Spinel Oxides for Photocatalytic Water Splitting: A Computational and Experimental study

by

Charlotte Hall

Submitted for the degree of Doctor of Philosophy

July 2025

Research Supervisors:
Dr Pilar Ferrer
Dr Ricardo Grau-Crespo
Dr David C. Grinter
Professor Georg Held

University of Reading

Department of Chemistry, School of Chemistry, Food and Pharmacy

Declaration

I confirm that this is my own work and the use of all material from other sources has been properly and fully acknowledged.

Charlotte Hall

Acknowledgements

During my PhD project I was very fortunate to meet and work with many great people. This means there's a lot of thanks to give, so strap in…

Firstly, I would like to thank my University of Reading supervisor, Ricardo Grau-Crespo. His ongoing support since the start of my undergraduate project has been invaluable, and without him I wouldn't have had this PhD opportunity. I'll miss our weekly library meetings! I would also like to extend my thanks to the past and present members of the GCMT group, particularly Ivan and Merve for providing so much support and fun throughout my PhD.

Secondly to my Diamond supervisors:

To Professor Georg Held, thank you for your endless knowledge of XPS and NEXAFS, going back all the way to my fourth-year undergraduate lectures. I'm incredibly grateful for all your advice and support in paper writing, data analysis, and more. And I can't forget to mention the amazing BBQs!

Dr David 'Dangerous DCG' Grinter, where would this project be without you? Thank you for keeping me calm and collected during my stressed-out moments, providing beamtime entertainment, answering my stupid questions and sharing your satsumas.

And finally, to Dr Pilar Ferrer. Her endless support and infectious positivity were such a driving force during this PhD and kept my motivation high. Pilar always helped me see the positive side of my work, even when I thought there would be no hope! Despite the long hours, tricky samples and terrible canteen food, Dave and Pilar always made beamtimes fun, they truly are the B07-B dream team.

I owe huge thanks to the whole B07 team for providing support and many laughs. I would like to specifically thank Dr Santosh Kumar for his catalysis expertise. And a big shout out to Dr Matthijs van Spronsen, the Igor Guru and my honorary 5th supervisor.

I would also like to thank the many collaborators who have contributed to the project. Firstly, to Dr Ivan da Silva for all his hard work, time and effort he put into the collection, processing and analysis of the X-ray diffraction data. To Professor Frank de Groot and his group for hosting me at Utrecht University and their help dealing with some very tricky data! Thank you to beamline scientists Dr Juan-Rubio-Zuazo, Dr Peter Bencok and Dr Francesco Carla and other collaborators Dr Roger Bennett, Dr Maria Retuerto, and Dr Roxy Lee.

I am grateful to Diamond Light Source and the University of Reading for funding the studentship. Thank you to the UK Materials and Molecular Modelling Hub for the computational resources, which is partially funded by EPSRC. I also thank the CompNanoEnergy COST Action group for funding my visit to Utrecht University.

I can't forget to thank all the PhD students who have made the last 4 years so much fun. Thanks to the office 100 boys, to the Durham Daves and to the Reading PhDs and postdocs: O. Matt, Jack, Archie^2, Lewis, Rob, Lucas, Callum Major, Callum Minor, Leon, Lochlan, Laila and more! Special shout out of course goes to Claudia and G. Matt. And a thank you and an apology goes to Sam for dealing with my thesis writing stress so well.

Someone who not only deserves my thanks but also some kind of award for putting up with me is Frances. She's been such an amazing friend since our first year of undergrad and since the PhD has been the best office- and housemate I could've asked for.

And finally (I promise this is the last one), my wonderful parents, thank you so much for supporting me in everything. I genuinely wouldn't be where I am today without your kindness, humour and, of course, financial aid. Congratulations Albert, you can finally retire now!

Abstract

Spinel oxides, AB_2O_4, exhibit significant promise in photocatalysis due to their favourable electronic properties, stability, compositional diversity, and tuneable cation distribution. Their photocatalytic activity can be modified through A and B cation substitution or by altering the cation distribution. The work in this thesis combines advanced quantum-chemical and synchrotron-based experimental methods to characterise various spinel materials and investigate their photocatalytic performance. Considering Co^{2+}, Cu^{2+} or Zn^{2+} as A cations in spinel ferrite (AFe_2O_4) nanoparticles revealed significant differences in their structures and photocatalytic abilities. $ZnFe_2O_4$ showed the highest activity for the oxygen evolution reaction, and this was further enhanced by substituting Ga^{3+} into the B sites: $ZnFeGaO_4$ produced almost double the amount of oxygen compared to $ZnFe_2O_4$. The activity of these samples was attributed to their suitable band gaps (3.35 eV and 2.84 eV, respectively) and alignments, as calculated by density functional theory. Exploring the structures of the spinel ferrites by X-ray diffraction and X-ray spectroscopy showed clear differences between bulk and surface cation distribution. Both $CoFe_2O_4$ and $CuFe_2O_4$ exhibited lower inversion degrees at the surface compared to the bulk, while $ZnFe_2O_4$ showed the opposite trend and with a more significant difference: DFT simulations showed that cation inversion in $ZnFe_2O_4$ is energetically favourable at the surface. To further understand the surface effects, a $ZnFe_2O_4$ (111) single-crystal surface with a well-defined bulk structure was studied. The surface preparation method was shown to have a significant effect on the surface structure. Annealing the sample under ultra-high vacuum resulted in zinc sublimation, leaving an iron-rich magnetite-like surface, whereas annealing under O_2 maintained the bulk-like $ZnFe_2O_4$ structure. The results highlight the distinct and important behaviour of the surfaces compared to the bulk in spinel ferrite catalysts.

List of Publications

Publications related to the work presented in this thesis:

1. Spinel ferrites MFe_2O_4 (M = Co, Cu, Zn) for photocatalysis: theoretical and experimental insights
   C. A. Hall, P. Ferrer, D. C. Grinter, S. Kumar, I. da Silva, J. Rubio-Zuazo, P. Bencok, F. de Groot, G. Held, R. Grau-Crespo, *J. Mater. Chem. A.* **2024**, 12, 29645-29656.

2. Zinc depletion at the $ZnFe_2O_4$ (111) single crystal surface: X-ray spectroscopy experiments and computer simulations
   C. A. Hall, D. C. Grinter, J. Sandemann, B. B. Iversen, R. A. Bennett, G. Held, R. Grau-Crespo, P. Ferrer, *Applied Surface Science*, **2025**, 713, 164253.

3. Preliminary draft of a third paper: The photocatalytic properties of $ZnFeGaO_4$ and $ZnGa_2O_4$: a theoretical and experimental study
   C. A. Hall, P. Ferrer, D. C. Grinter, S. Kumar, I. da Silva, M. Retuerto, F. de Groot, G. Held, R. Grau-Crespo.

Publication from PhD period but not included in this thesis:

4. Fabrication of Isolated Iron Nanowires
   D. C. Grinter, B. A. Shaw, C. L. Pang, C. Yim, C. A. Muryn, C. A. Hall, F. Maccherozzi, S. S. Dhesi, M. Suzuki, T. Yasue, T. Koshikawa, G. Thornton, *J. Phys. Chem. Lett.* **2023**, 38, 8507-8512.

Abbreviations

DLS	Diamond Light Source
VerSoX	Versatile soft X-ray beamline
XPS	X-ray photoelectron spectroscopy
NAP-XPS	Near-ambient pressure X-ray photoelectron spectroscopy
XAS	X-ray absorption spectroscopy
NEXAFS	Near-edge X-ray absorption fine structure
XMCD	X-ray magnetic circular dichroism
TEY	Total electron yield
TFY	Total fluorescence yield
UHV	Ultra-high vacuum
LEED	Low-energy electron diffraction
STM	Scanning tunnelling microscopy
PXRD	Powder X-ray diffraction
AXRS	Anomalous X-ray scattering
RT	Room temperature
DFT	Density functional theory
LDA	Local density approximation
GGA(+U)	Generalised gradient approximation (Hubbard corrections)
PBE	Perdew-Burke-Enzerhof
PAW	Projector augmented wave
HSE	Heyd, Scuseria and Ernzerhof
VASP	Vienna *ab initio* simulation package
Oh	Octahedral
Td	Tetrahedral

Contents

1. Introduction

1.1 Spinels

The spinel structure was discovered in 1915 independently by Nishikawa[1] and Bragg,[2] and over 200 different spinel compounds have been identified or synthesised since.[3] The spinel group shares a structure and name with the mineral, $MgAl_2O_4$, which was often referred to as 'spinel ruby', with the red colour being caused by trace-amounts of impurities. The general formula of a spinel is written as AB_2X_4, in which A and B are typically divalent and trivalent cations, respectively, and the X anion is usually a group VI species, *i.e.* O^{2-}, S^{2-}, Se^{2-} and Te^{2-}. However, there are other less common X anions that form stable spinel structures, such as CN^-, F^-, and N^{3-}. The general structure of a spinel in the conventional unit cell can be seen in **Figure 1.1**. This unit cell is in the face-centred cubic (fcc) arrangement, with most spinels belonging to the space group *Fd3m*.[4]

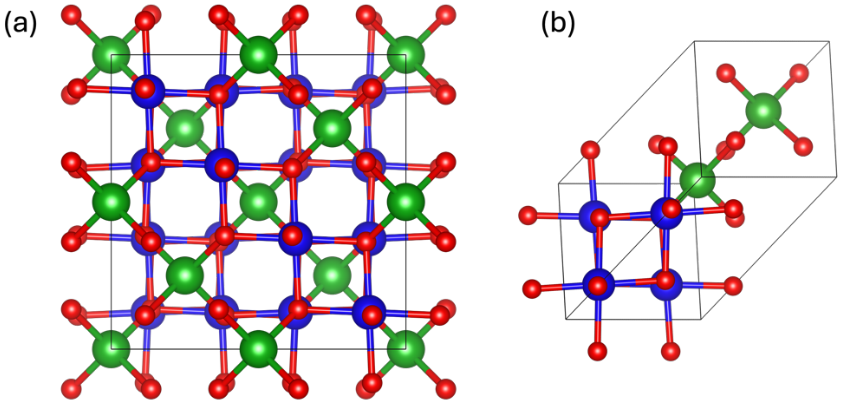

Figure 1.1. Crystal structure of a spinel, AB_2X_4, represented by (a) the conventional unit cell and (b) the primitive unit cell. Colour scheme: tetrahedral (Td) sites = green; octahedral (Oh) sites = blue; X = red. Images produced by VESTA.[5]

Within a 'normal' spinel structure, the A and B cations occupy tetrahedral (Td) and octahedral (Oh) sites, respectively. However, these cations can be distributed differently across the Td and Oh sites, and their relative occupancy is referred to as the degree of inversion (x). In a fully inverse spinel, the Oh sites are occupied by all the A cations and half of the B cations, and the remaining B cations occupy the Td sites. Partial inversion, where $0 < x < 1$, can also occur. The formula can therefore be written as $(A_{1-x}B_x)[A_xB_{2-x}]O_4$, where () and [] represent the Td and Oh sites, respectively. The degree of inversion ($0 \leq x \leq 1$) is defined in this formula as the fraction of Td sites occupied by B cations.

The inversion degree is dependent on several factors, such as ion size, electrostatic stabilisation, bonding, and crystal-field stabilisation energy (CFSE) site preferences.[6] The interstitial Oh sites in the crystal lattice are "larger" (in the sense that they are centred at longer distance to the anions) than the Td sites, therefore cations with a larger ionic radius will generally prefer to sit in the larger Oh sites. For example, in the inverse spinels $NiFe_2O_4$ [7, 8] and $CoFe_2O_4$ [9, 10] the ionic radii of Ni^{2+}(0.69 Å) and Co^{2+} (0.75 Å) in Oh coordination are greater than that of Fe^{3+} (0.64 Å),[11] therefore the A^{2+} cations will preferentially sit in Oh sites. If we consider the normal spinel $ZnFe_2O_4$,[12] where the ionic radius of Zn^{2+} (0.74 Å)[11] is larger than Fe^{3+}, the electrostatic stabilisation has a stronger influence. The electrostatic stabilisation means that generally the trivalent B cations will preferentially be surrounded by a larger number of anions (Oh) to balance for its higher positive charge (3+ compared to 2+). In $ZnFe_2O_4$ there is also a strong influence with respect to the bonding in the material. Zn^{2+} generally has a preference for Td sites over Oh,[13-15] due to the tendency to form strong sp^3 hybridisation with the anion.[16, 17] In contrast, when looking at inverse spinels, such as $NiFe_2O_4$ and $CoFe_2O_4$ the CFSE is likely to have the strongest influence on the cation distribution, as the d^8 and d^7 configurations of Ni^{2+} and Co^{2+}, respectively, are significantly more stable in Oh coordination.[18-20] In general, both the size effects and electrostatic stabilisation are less influential compared to bonding effects and CFSE.[21]

In some cases, the degree of inversion (x) observed for a given spinel can be influenced by the synthesis method or post-synthesis treatment. However, the ability to accurately and reliably control or predict a specific inversion degree remains a challenge.[21] Spinels can be prepared by a wide range of methods, such as pulsed laser, sol-gel, combustion and plasma preparation methods,[22] but these methods generally are not used on a large scale due to issues, such as long reaction times, costly or toxic reagents, and complicated synthesis steps. A more commonly used preparation method is co-precipitation, due to its relative simplicity and potential ability to control particle size.[23]

The synthesis conditions can affect the inversion degree, for example Tiano *et al.*[24] observed a significant decrease in inversion degree of $NiFe_2O_4$ nanoparticles, from $x = 1$ to $x = 0.84$, by introducing a surfactant into the reaction mixture when synthesised by a generalised hydrothermal method. Similarly, by changing the synthesis precursors under solvothermal conditions, Vamvakidis *et al.*[25] were able to increase the inversion degree of $MnFe_2O_4$ from $x = 0.22$ to $x = 0.42$.

The temperature during preparation or a post-synthesis annealing process can also have a strong influence on x. Early work by Néel[26] and Smart[27] outlined a simplified approach to understanding the thermodynamics of this effect, in which cation distribution is primarily influenced by the configurational entropy. A more advanced understanding of this was later presented and summarised by Callen *et al.*[28] and Navrotsky and Kleppa,[29] who considered both entropic and enthalpic contributions. These studies show that, at higher temperatures, spinels will approach a thermodynamically favoured random cation distribution, corresponding to an inversion degree of $x = 2/3$.[16, 29] For example, Granone *et al.*[30, 31] observe an increase from a near-normal inversion degree to $x = 0.2$ in $ZnFe_2O_4$ with increasing temperatures from 800 – 1200 K. A similar trend was reported by Bræstrup *et al.*[32] in $ZnFe_2O_4$. The normal spinel structure of $ZnAl_2O_4$ also demonstrates an increased inversion degree at higher temperatures.[33] On the contrary, the fully inverse spinel $CuFe_2O_4$, showed a decrease in inversion from $x = 1$ to $x = 0.77$ at higher temperatures.[34]

Although heating the samples allows for a specific cation distribution to be induced (based on the thermodynamics), the cooling process is crucial to maintaining x. During cooling, the kinetics of rearrangement can slow down enough that the cations are held into a nonequilibrium state.[35] It is suggested that rapid cooling (*e.g.* quenching in water) could retain an inversion degree nearer to the random distribution than to the equilibrium inversion. An example of the influence of cooling a $CoFe_2O_4$ spinel (typically fully inverse) was presented by Sawatzky *et al.*.[36] After being heated for 48 hours at 1200°C, the samples were quenched rapidly and cooled slowly to room temperature, resulting in inversion degrees of $x = 0.79$ and $x = 0.96$, respectively.

Due to their high compositional and structural diversity and favourable electronic structure, spinel materials exhibit significant promise in photocatalysis. The main area of focus of this thesis is their use as photocatalysts for the water splitting reaction.

1.2 Photocatalytic water splitting

The development of clean and sustainable energy sources has been one of the most important areas of research in the 21st century. As of 2024, over 100 countries have pledged to achieve Net Zero,[37] in which any carbon emissions are offset by removal of greenhouse gases from the atmosphere. Solar, geothermal, wind, and hydropower make up some of the alternative energy sources that, compared to fossil fuels, are relatively clean. However, there are limitations to these clean sources, such as cost of construction and operation, storability issues and environmental constraints.

Hydrogen (H_2) production has received significant attention as a suitable alternative energy resource. H_2 has the potential to offer a scalable, long-term, and cost-effective route to decarbonisation and could have a huge impact in areas, such as transport, industry, and heating.[38] There are various methods of hydrogen production, each with pros and cons with respect to their environmental impact, cost and prospects. The majority of H_2 is currently produced by a methane-steam reforming process. Although this method is relatively low cost in comparison with other production methods, it produces significant amounts of greenhouse gases and relies on non-renewable energy sources.

Photocatalytic water splitting is a promising route to producing clean, renewable H_2. This method utilises the natural resources of water and solar light, and has advantages, such as extremely high H_2 purity[39] and low toxicity with respect to the reactants and by-products.[40] The development of generating H_2 through the water splitting process is crucial to reaching the global Net Zero goal.

The first report of photocatalytic water splitting in a photo-electrochemical cell with a TiO_2 photocatalysts was published in 1972 by Fujishima and Honda.[41]. The process is generally described by the following three steps: (i) the generation of an electron/hole pair by photo absorption, (ii) the separation and migration of the photoexcited carriers to the surface, avoiding electron and hole pair recombination as much as possible before the final step can occur. Finally, step (iii) involves the reduction and oxidation of water by the photogenerated holes and electrons, producing O_2 and H_2, respectively. A diagram outlining these three steps can be seen in **Figure 1.2A**.

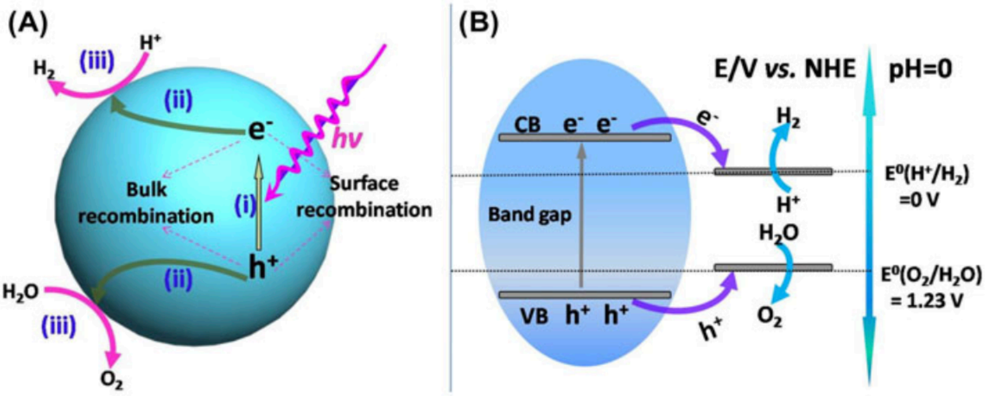

Figure 1.2. (A) The water splitting process and (B) the scheme of the process with a photocatalyst.[42]

The water splitting process is separated into the following two half reactions: the oxygen evolution reaction (OER) and the hydrogen evolution reaction (HER).

OER: $H_2O \rightarrow 2H^+ + 2e^- + \frac{1}{2}O_2$

HER: $2H^+ + 2e^- \rightarrow H_2$

The kinetics of the OER are substantially slower than those of the HER, as evidenced by a large overpotential, making this the rate limiting step.[42, 43] An efficient photocatalyst must have a band gap larger than 1.23 eV to thermodynamically overcome the water splitting energy barrier.[44] However, in order to reduce the charge carrier recombination rate, the ideal band gap increases to ~1.8 eV.[45-47] The photocatalyst must also display a suitable band alignment, with the conduction band (CB) and valence band (VB) straddling the half reaction potentials, *i.e.* the VB maximum lies below the OER potential and the CB minimum lies above the HER potential (**Figure 1.2B**).

Finding a suitable photocatalysts comes with many challenges, and as of today there is no single material that has been found suitable and active enough for the entire water splitting process under visible radiation.[43] Various potential photocatalysts have been identified, with a handful of examples being shown in **Figure 1.3**. $NaTaO_3$, $SrTiO_3$ and TiO_2 are classed as wide band gap materials (> 3 eV).[48-50] Despite their favourable band alignment, their large band gap makes them inefficient in the visible light region, and therefore limits their uses as photocatalysts.[51, 52] However, a suitable band gap does not necessarily guarantee a favourable band alignment, as demonstrated by WO_3, with CB minimum lying below the HER potential.[53]

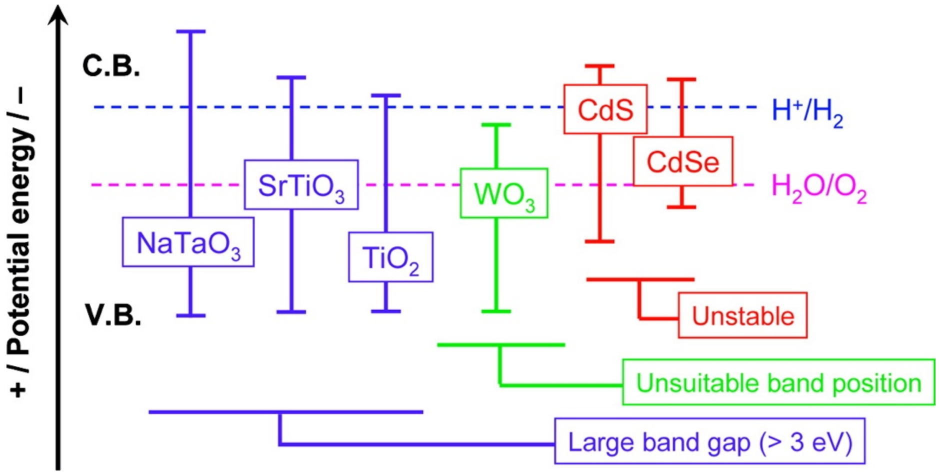

Figure 1.3. A schematic of the band alignments of various photocatalysts with respect to the water splitting half reaction potentials.[54]

Photostability is also important for the catalysts. For example, despite the known photocatalytic activity of the chalcogenides, CdS and CdSe, under visible light and their suitable band alignment, they suffer greatly with photo-corrosion making them unsuitable photocatalysts.[55, 56]

To independently study either the HER or the OER, sacrificial agents (or scavengers) can be used to suppress the counter half reaction.[42] For the HER, hole scavengers, such as methanol or triethylamine, can act as electron donors which consume the photogenerated holes, therefore allowing the electrons to reduce H^+ to H_2. In contrast, the OER requires electron scavengers, such as silver nitrate or silver chloride, leaving the holes to oxidise the water molecules.

In photocatalysis, both the bulk and the surface of the photocatalyst play crucial but distinct roles. The bulk structure primarily determines the materials electronic properties, including the band gap and alignment, which dictate the light absorbed and its suitability for specific reactions.[43] However, the surface is equally important, as it is the site where the actual photocatalytic reactions take place. The surface area and morphology significantly influence the photocatalytic performance by affecting the adsorption of reactants and availability of active sites.[57] While the electron-hole pairs are generated in the bulk, both the bulk and surface structure impact the recombination rate, which is critical to the catalysts efficiency. The use of a co-catalysts or constructed heterojunctions can enhance the overall efficiency of a photocatalyst by increasing light absorption, promoting charge separation and transport, providing additional active sites and reducing photocorrosion.[43, 58]

1.3 Spinel oxides for photocatalytic water splitting

A wide range of spinel structures have been studied as photocatalysts, not only for the water splitting reaction, but also for other photocatalytic applications, such as CO_2 reduction[59] or phenol degradation.[6] Spinel ferrites are attractive materials for photocatalytic applications for several reasons. First, their electronic structure and optical properties can be tuned via their composition and/or cation distribution, which allows optimising light absorption or targeting specific band alignments.[60-62] Second, they tend to be chemically stable under a wide range of temperatures and pH levels.[3] Third, they are magnetic, which allows for easy recovery and reuse of the photocatalyst from the reaction mixture, reducing waste and improving process efficiency.[63] Spinel ferrites are also relatively cheap catalysts and can be made up of naturally abundant metals.[64, 65] However, there are also drawbacks, such as irregular morphology, poor conductivity, insufficient active sites, and charge-carrier recombination.[59, 64] In many studies of spinel materials where photocatalytic activity is observed, they are rarely used as a lone catalyst. Instead, sacrificial agents, co-catalysts, or composite structures, such as heterojunctions combining spinels with other wide band-gap materials, are often employed.[39, 64, 66-68]

There are three key methods to modify the spinel configuration and structure that can influence their photocatalytic ability: (i) the substitution of A cations, (ii) the substitution of B cations, and (iii) tuning the inversion degree. The work presented in this thesis concentrates on spinel oxides, AB_2O_4, with the main focus on spinel ferrites (where the B cation is Fe^{3+}) for photocatalytic water splitting. In order to understand their photocatalytic properties, it is crucial to characterise their bulk and surface structures. The work mainly discusses cation substitution, the spinel materials discussed in Chapters 4, 5, and 6, where A = Co, Cu, or Zn and B = Fe or Ga, are introduced in the following subsections.

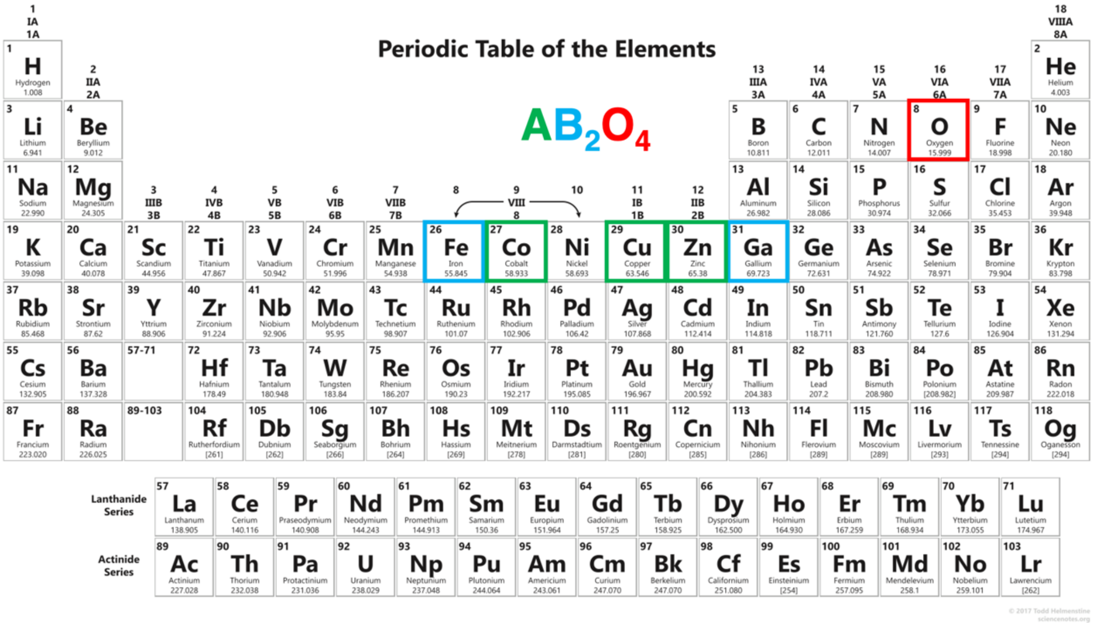

Figure 1.4. The periodic table highlighting the A (green) and B (blue) cations studied in the AB_2O_4 spinels. Figure adapted from ref.[69]

1.3.1 *Cobalt ferrite*

Cobalt ferrite, $CoFe_2O_4$, is a widely studied spinel with a range of interesting applications. Its uses span from biomedical fields, such as bone tissue engineering[70] or hyperthermic cancer treatment,[71] to photocatalytic applications, such as degradation or water splitting.[72] Bulk cobalt ferrite is generally understood to be a fully inverse spinel structure ($x \approx 1$),[10, 73] where the cobalt and iron are A and B cations, respectively. The preference for high inversion in $CoFe_2O_4$ has been confirmed by several theoretical studies.[62, 74] The Co^{2+} cation (d^7) has an Oh stabilisation energy of 30.9 kJ mol^{-1},[75] which compared to Fe^{3+} (d^{10})

with no CFSE, results in the stabilisation of the inverse distribution. However, in smaller nanoparticles, lower inversion degrees of x = 0.66 – 0.68 have been observed.[76, 77]

The degree of inversion is crucial to the study of spinels. However when dealing with a sample, such as cobalt ferrite, three degrees of freedom need to be considered: (i) the inversion degree, (ii) potential charge transfer, and (iii) spin states. Generally, in $CoFe_2O_4$, the cations maintain their respective charges of Co^{2+} and Fe^{3+},[10, 78] but both cobalt and iron can be divalent or trivalent cations. The mix of Co^{2+}/Co^{3+} and Fe^{2+}/Fe^{3+} cations are observed in Co_3O_4 [79] and Fe_3O_4 (magnetite),[80] respectively. Wakabayashi *et al.*[81] conducted a study of a $CoFe_2O_4$ (111) thin film in which Fe^{3+} and Co^{2+} occupy both Oh and Td sites with a preference towards full inversion, but they also observed low amounts (< 20%) of Co^{3+} and Fe^{2+} in Oh sites. The thin film also demonstrated more significant charge transfer at the surface,[81] a similar phenomenon that has also been reported by Subedi *et al.*.[82]

The third degree of freedom, spin states, needs to be considered in spinel structures containing transition-metal cations. Although divalent and trivalent cobalt and iron can be in either high-spin or low-spin states, in cobalt ferrite both Co^{2+} and Fe^{3+} are generally reported to be high-spin.[81, 83] The high-spin configuration of these cations is also more stable in computational simulations.[9, 74]

Cobalt ferrite is commonly discussed in the literature for its use in photocatalytic water splitting.[68, 84] However, it is rarely reported as a stand-alone catalyst. Typically, it is used alongside an electron/hole scavenger, and the specific sacrificial agent used can help to improve the samples activity. For example, Benlembarek *et al.*[85] reported a significantly improved activity in hydrogen evolution (by a factor of 57%) of $CoFe_2O_4$ nanoparticles using a combination of oxalate ($C_2O_4^{2-}$) and NaOH as hole scavengers compared to NaOH alone. A similar study of a nanoporous cobalt ferrite sample by He *et al.* [86] demonstrated greater hydrogen production using triethanolamine (TEOA) over methanol. This was attributed to a shift in the HER potential caused by an increase in pH from the TEOA, therefore improving the electron transport efficiency. In many cases, $CoFe_2O_4$ is used as part of a heterojunction alongside materials, such as Fe_2O_3,[87] C_3N_4,[88] and the spinel ZnI_2S_4.[89] Ge *et al.*[90] found that a

$CoFe_2O_4/ZnI_2S_4$ heterojunction produced ~5 times the amount of hydrogen compared to $CoFe_2O_4$ alone.

The use of spinel ferrites for the HER is generally more widely studied in the literature compared to the OER. Several studies highlight the potential photocatalytic ability of cobalt ferrite nanoparticles for the OER,[91, 92] including the catalytic improvement using co-catalysts or doping.[93-95] However, the area of research for oxygen evolution is still relatively undeveloped.

1.3.2 *Copper ferrite*

Copper ferrite, $CuFe_2O_4$, shares similar properties to cobalt ferrite, also having uses in biomedicine [96, 97] and photocatalysis, *e.g.* degradation,[98, 99] C-C coupling[100] and water splitting.[101] With Cu^{2+} having an excess Oh stabilisation energy of 63.5 kJ mol^{-1},[75] $CuFe_2O_4$ also favours high inversion degrees.[34, 102, 103] The preference for full inversion has also been demonstrated by computational techniques.[104, 105] However, copper ferrite also demonstrates a difference in inversion between bulk and nanoparticle samples. Siddique *et al.* [106] report a high inversion degree of $x = 0.88$ in bulk $CuFe_2O_4$ compared to $x = 0.80$ in nanoparticle form. Inversion degrees as low as $x = 0.57$ have been found in small nanoparticles of less than 10 nm.[107]

Similarly to cobalt ferrite, $CuFe_2O_4$ is mainly discussed for its use in the HER, and its use for the OER is less developed.[108-110] Although copper ferrite is still rarely used as a bare catalyst for the HER, Soto *et al.* [111] report a hydrogen evolution of 336 μmol g^{-1} h^{-1} with cobalt ferrite nanoparticles without the use of a scavenger. However, the amount of H_2 produced is increased significantly when a Na_2SO_3/Na_2S scavenger mixture is used (3605 μmol g^{-1} h^{-1}). Methanol [112] and oxalate [113] are also commonly used as sacrificial agents with copper ferrite. Examples of successful heterojunctions constructed with $CuFe_2O_4$ include C_3N_4,[114] Fe_2O_3,[115] and BiOX (X = Cl, Br, I).[112]

1.3.3 *Zinc ferrite*

Zinc ferrite ($ZnFe_2O_4$) although similar in many ways to cobalt and copper ferrite, has several advantages that increase its potential for wider use. For example, in biomedical applications, zinc-based spinels are generally preferred in comparison with other divalent transition metals, due to the relatively low toxicity of Zn^{2+} in the human body.[116] $ZnFe_2O_4$ also has the potential to be synthesised using biological materials, *i.e.* plants, algae and microorganisms.[117] This brings the advantage of being able to produce nanoparticle samples with a significantly reduced negative environmental impact compared with other methods of synthesis.

Unlike the previous spinels discussed, zinc ferrite exhibits very low inversion degrees in bulk structures, reaching near-normal distributions ($x \approx 0$).[12] This is partly due to the absence of CFSE effects, as both the Zn^{2+} (d^{10}) and high spin Fe^{3+} (d^5) cations have no CFSE. Additionally, as previously mentioned in section 1.1, the Zn^{2+} cations have a strong preference for Td over Oh coordination due to electrostatic stabilisation[13-15] and bonding effects,[16, 17] influencing the low values of x observed. Like cobalt and copper ferrite, the cation distribution of $ZnFe_2O_4$ nanoparticles deviates from the bulk. Zinc ferrite nanoparticle samples display higher inversion degrees of up to $x = 0.4$, depending on particle size and thermal history.[118, 119]

Compared to cobalt and copper ferrites, zinc ferrite is a more efficient photocatalyst for the HER.[66] In a study by Rodríguez *et al.*,[120] more than twice the amount of H_2 was produced by $ZnFe_2O_4$ compared to $CoFe_2O_4$ over 8 hours with a methanol sacrificial agent. Lv *et al.* [121] found that introducing methanol, a commonly used scavenger,[122] significantly improved the catalytic ability. Several studies have also found an increase in efficiency using heterojunctions with other materials, such as BiOBr,[90] $SrTiO_3$,[123] and C_3N_4.[124] Kalia *et al.* [125] found that introducing a Pt co-catalyst increased the hydrogen evolution by almost 10 times that of the bare $ZnFe_2O_4$ nanoparticles with a TEOA scavenger. Like cobalt and copper ferrite, the use of zinc ferrite structures for the OER has received limited attention.[126-128]

1.1.4 Gallium-substituted zinc ferrite

Substituting the B cation is a strategy to enhance the catalytic efficiency of established catalysts, such as zinc ferrite. Replacing the Fe^{3+} in $ZnFe_2O_4$ with Ga^{3+} has proved effective in achieving this improvement.[125, 129] $ZnFe_yGa_{2-y}O_4$ spinels (0

$\leq y \leq 1$) tend towards a normal cation distribution with very low inversion, [125, 129, 130] as the introduction of Ga^{3+} to replace Fe^{3+} cations has no effect with respect to the CFSE. However, Li *et al.*[131] report inversion degrees up to $x = 0.3$ in $ZnGa_2O_4$ with varied preparation methods and annealing temperature.

Xu *et al.* [129] report an increased hydrogen evolution with Ga^{3+} doping, *i.e.* $ZnFe_2O_4 < ZnFeGaO_4 < ZnGa_2O_4$, with a Na_2SO_3 sacrificial agent. They attribute this to a modified electronic structure which in turn improves UV light absorbance. The same trend in activity was also observed by Kalia *et al.*;[125] however, their spinels were used alongside a Pt co-catalyst and a methanol hole scavenger. The use of co-catalysts and sacrificial agents is common in spinel-catalysed water splitting to improve their efficiency.[59, 64] Part of the improved catalytic ability was attributed to the increased band gap of $ZnGa_2O_4$, therefore reducing the electron-hole recombination rate compared to $ZnFe_2O_4$. However, their synthesis of $ZnGa_2O_4$ resulted in some residual ZnO, which could also be improving the activity by forming a heterostructure. The use of $ZnO/ZnGa_2O_4$ heterojunctions is a common strategy for improving the photocatalytic ability of $ZnGa_2O_4$ catalysts.[132, 133] An improvement in the hydrogen-evolution performance of $ZnGa_2O_4$ as a lone catalyst by creating mesoporous nanoflowers was demonstrated by Yang *et al.*.[134] The hydrogen evolution demonstrated by the various spinels structures introduced in this Chapter in the visible light range and under various conditions are listed in **Table 1.1**.

Table 1.1. The hydrogen evolution from spinel ferrite samples under visible light irradiation.

Catalyst	Type	Sacrificial agent	H_2 evolution	Ref
$CuFe_2O_4$	Nanoparticles	No Scavenger Na_2SO_3/Na_2S	336 μmol h^{-1} g^{-1} 3605 μmol h^{-1} g^{-1}	111
$CuFe_2O_4$ $CuFe_2O_4$/BiOCl	Nanoparticles Heterojunction	Methanol	< 5000 μmol h^{-1} 22000 μmol h^{-1}	112
$CuFe_2O_4/C_3N_4$	Heterojunction	TEOA	76 μmol h^{-1}	114
$CoFe_2O_4$	Nanoparticles	NaOH $NaOH/C_2O_4^{2-}$	47 μmol min^{-1} g^{-1} 74 μmol min^{-1} g^{-1}	85
$CoFe_2O_4$	Nanoporous Material	Methanol TEOA	28 μmol h^{-1} g^{-1} 88 μmol h^{-1} g^{-1}	86

Ag-$CoFe_2O_4/C_3N_4$	Heterojunction	TEOA	335 μmol h^{-1}	88
$CoFe_2O_4$	Nanoparticles	TEOA	334 μmol h^{-1} g^{-1}	90
$CoFe_2O_4/ZnIn_2S_4$	Heterojunction		1577 μmol h^{-1} g^{-1}	
$CoFe_2O_4$	Nanoparticles	Methanol	128 μmol g^{-1} (over 8 hours)	120
$ZnFe_2O_4$			354 μmol g^{-1} (over 8 hours)	
$ZnFe_2O_4$	Nanocrystalline material	Methanol	134 μmol g^{-1} (over 4 hours)	122
$ZnFe_2O_4$	Porous nanorods	No scavenger	85 μmol g^{-1} (over 5 hours)	121
		Methanol	238 μmol g^{-1} (over 5 hours)	
$ZnFe_2O_4/SrTiO_3$	Heterojunction	$Na_2S_2O_3$	9200 cm^3 h^{-1} g^{-1}	123
$ZnFe_2O_4$	Nanoparticles	Methanol	170 μmol h^{-1} g^{-1}	124
$ZnFe_2O_4/C_3N_4$	Heterojunction		1752 μmol h^{-1} g^{-1}	
$ZnFe_2O_4$	Nanoparticles	Na_2SO_3	861 μmol h^{-1} g^{-1}	129
$ZnFeGaO_4$			971 μmol h^{-1} g^{-1}	
$ZnGa_2O_4$			> 971 μmol h^{-1} g^{-1}	
$ZnFe_2O_4$	Nanoparticles	TEOA	378 μmol h^{-1} g^{-1}	125
Pt-$ZnFe_2O_4$	Co-catalyst		3089 μmol h^{-1} g^{-1}	
Pt-$ZnFeGaO_4$			~ 3750 μmol h^{-1} g^{-1}	
Pt-$ZnGa_2O_4$			3989 μmol h^{-1} g^{-1}	
$ZnGa_2O_4$	Mesoporous Particles	Na_2SO_3	700 μmol h^{-1} g^{-1}	134
	Nanoflowers		1500 μmol h^{-1} g^{-1}	

1.4 Thesis objectives and outline

The overall objective of the work presented in this thesis is to understand the properties of spinel ferrites, in particular the effect of cation distribution and substitutions, and the interplay between bulk and surface, in connection with their photocatalytic applications. For that purpose, a synergistic combination of experimental and theoretical methods has been used.

This introduction section has explored the background of spinels and their uses in photocatalysis. This Chapter is followed by an overview of the experimental and computational techniques used throughout the research in Chapters 2 and 3, respectively. The experimental methodology will mainly cover the synchrotron techniques of X-ray photoelectron spectroscopy and X-ray absorption spectroscopy with a brief introduction to some other techniques utilised to carry out the structural characterisation and catalysis measurements. The theoretical techniques covered in Chapter 3 include density functional theory and semi-empirical calculations used in the study of the spinel configurations, electronic structures and to aid in the experimental analysis.

Chapter 4 is presenting published work studying cobalt ferrite, copper ferrite and zinc ferrite nanoparticles.[135] In this work the spinels bulk and surface structures were studied experimentally with the support of theoretical calculations. The photocatalytic activity of the samples was also investigated, and their respective behaviours were rationalised using electronic structure calculations.

Chapter 5 presents work conducted on a zinc ferrite (111) single-crystal with the aim to investigate the sample surface and how it is affected by different treatment methods. Various experimental techniques were used alongside density functional theory calculations.

Chapter 6 contains work studying $ZnFeGaO_4$ and $ZnGa_2O_4$ nanoparticles, looking at the substitution of Ga^{3+} into the B sites of zinc ferrite. Similarly to the work presented in Chapter 4, the photocatalytic ability measured and the DFT electronic structure is analysed. The DFT analysis of the inversion degree of the spinels was studied.

Finally, Chapter 7 summarises the work presented in the previous Chapters and provide a general discussion of the PhD project. I also discuss ideas of future experimental and theoretical work to further develop this research.

2. Experimental Methods

2.1 Introduction

2.1.1 Synchrotron radiation

Synchrotron radiation was first discovered at General Electric in 1947,[136] however the supporting theory can be traced back earlier to 1873, when Maxwell published his theory of electromagnetism.[137] A major theoretical advancement came in 1949, when Julian Schwinger derived a quantum formulation of synchrotron radiation, now known as the Schwinger equation.[138] Since then, the number of experiments using synchrotron radiation has grown significantly. There are currently approximately 70 synchrotrons globally at various stages of development, conducting experiments spanning a wide range of applications and research topics.[139-141]

The first stage of generating a synchrotron light source is to initially accelerate the electrons using a linac, or linear accelerator. These electrons will then enter a booster ring where, with the use of a series of magnets, the energy of the electrons is increased before they are transferred to a larger storage ring. The storage ring uses electromagnets to move the electrons around a series of adjacent straight sections which form a closed loop. These electrons, which are travelling almost at the speed of light around the ring, generate synchrotron radiation, which spans across the electromagnetic spectrum from infrared to X-ray light. A diagram of a typical synchrotron set up can be seen in **Figure 2.1**.[142] In order to minimise loss of electrons and maintain a high energy beam, the system is maintained under ultra-high vacuum (UHV). The electron beam can then be directed to individual beamlines using either a bending magnet or an insertion device. Synchrotron light sources have many benefits, including variable photon energy and polarisation, high flux and high brightness. However, due to high demand and limited synchrotron facilities, access for researchers can be difficult to obtain.

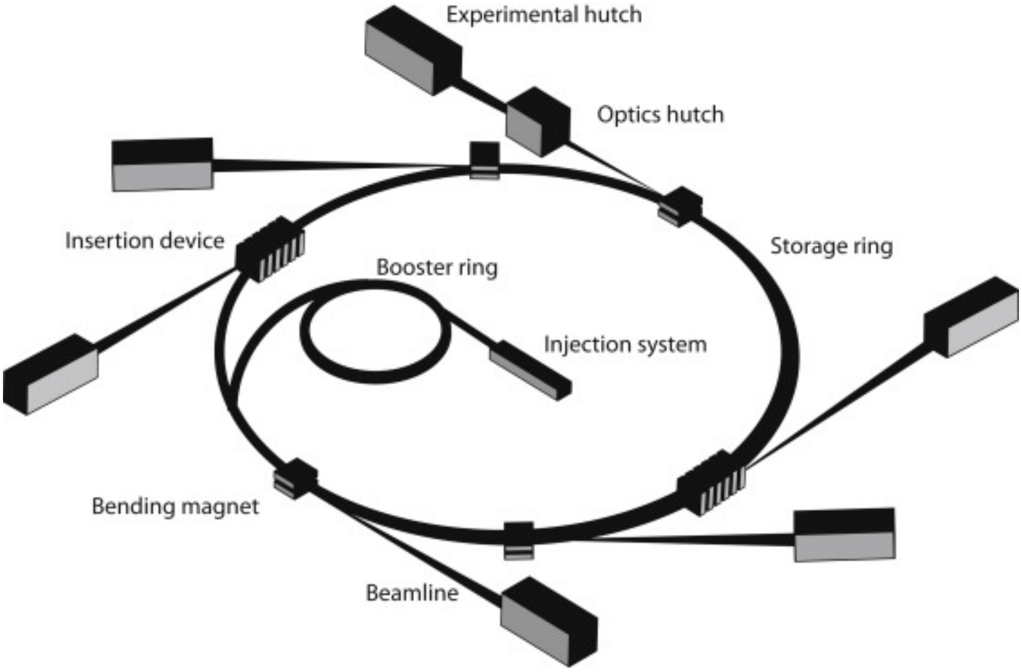

Figure 2.1. Schematic representation of a typical synchrotron.[142]

2.1.2 Versatile soft X-ray beamline

The Versatile soft X-ray (VerSoX) beamline B07 at Diamond Light Source (DLS) is a soft X-ray beamline. The synchrotron radiation is directed from the storage ring to the beamline by a bending (dipole) magnet, which emits a wide fan of synchrotron light. This allows for B07 to be split into two branches, B and C, each of which can operate simultaneously due to their independent optics set up. The layout for the B and C branches can be seen in **Figure 2.2**.[143] The C branch endstation is set up for near-ambient pressure X-ray photoelectron spectroscopy (NAP-XPS), at an energy range of 120 eV to 2800 eV.[144]

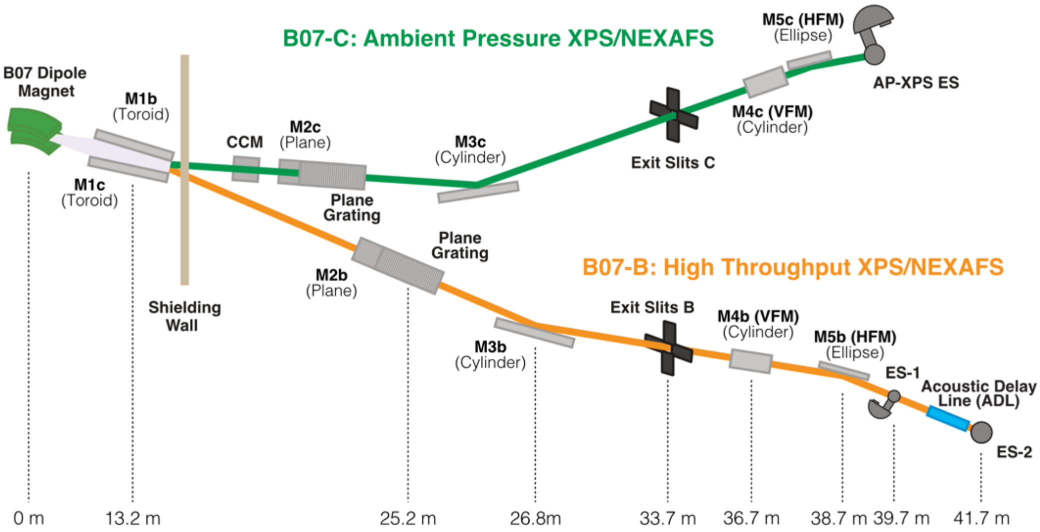

Figure 2.2. Schematic of the VerSoX B07 beamline layout.[143]

Most of the spectroscopic work presented in this thesis has been measured on branch B of the VerSoX beamline, which covers a slightly lower photon energy range of 45 eV to 2200 eV.[143, 145] This branch has two focal points with two endstations dedicated to both XPS and X-ray absorption spectroscopy (XAS) experiments under UHV or ambient pressures. The ability to conduct both XPS and XAS is highly beneficial as they are complementary techniques probing the occupied and unoccupied states, respectively. The beam is directed at the endstations using a combination of monochromators, exit slits and mirrors. The mirrors are designed to focus and direct the beam, and the exit slits define the beamsize, flux, and resolution before reaching the endstation. The plane grating monochromator (PGM) disperses the incoming beam vertically using a diffraction grating. The photon energy can be set by adjusting the grating and mirror angles within the PGM to diffract a specific wavelength.

Endstation 1 (ES-1) has the capability to conduct XPS and near-edge X-ray absorption fine structure (NEXAFS) measurements under UHV conditions. Angle-resolved measurements can be undertaken on this endstation to probe different sample depths. ES-1 also has the capability to measure NEXAFS by total electron yield, total fluorescence yield, Auger electron yield, and (inverse) partial fluorescence yield (using a vortex detector). ES-1 also contains a preparation chamber, in which samples can undergo treatment and preliminary characterisation, such as sputtering, thermal treatment, gas-dosing, and low-energy electron diffraction (LEED). Endstation 2 (ES-2) has the ability for

NEXAFS measurements by total electron yield or total fluorescence yield, with an ambient pressure range of 10^{-7} mbar to 1 bar.

2.2 X-ray photoelectron spectroscopy

2.2.1 Introduction

X-ray Photoelectron Spectroscopy (XPS) is an analytical technique built on the theory of the photoelectric effect. This was first discovered by Hertz in 1887 [146] and later explained by Einstein in 1905, [147] eventually winning him a Nobel prize in 1921. The following decades saw the development of XPS into an established analytical technique, mainly through work conducted by Siegbahn, *et al*,[148] who won a Nobel prize in 1981. Since then, XPS has become widely available, with its uses spanning across a vast range of materials and research fields.

During the XPS process, X-rays with a known energy (hv) are directed at sample, exciting and emitting a core level electron, as shown in **Figure 2.3**. This emitted electron has a kinetic energy (E_{kin}) which is measured by a detector, and therefore the binding energy (E_{B}) can be calculated by the following equation:

$$hv = E_{\text{B}} + E_{\text{kin}} + \varphi \tag{1}$$

where φ is the work function, which refers to the minimum energy required to remove an electron from the Fermi level to the vacuum level. The E_{kin} and E_{B} are measured relative to the vacuum level energy and Fermi level energy, respectively.

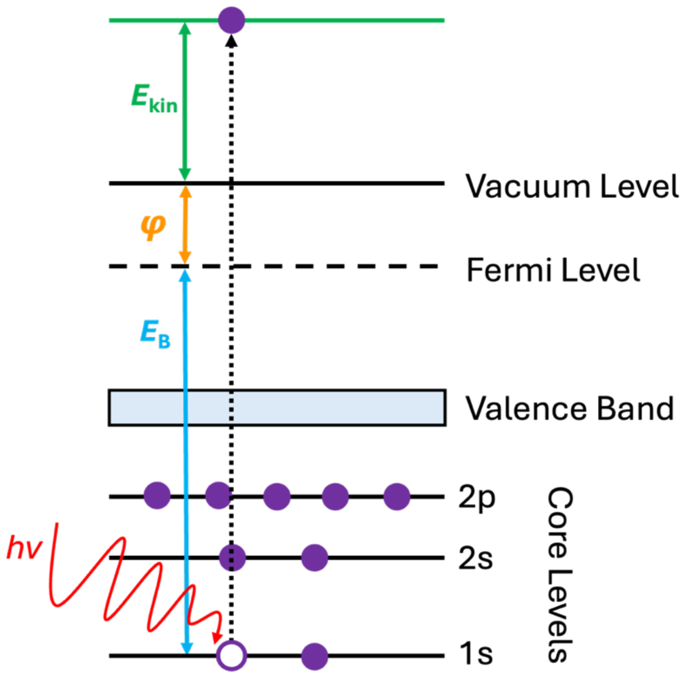

Figure 2.3. Diagram of the X-ray photoelectron spectroscopy (XPS) process.

The binding energy is intrinsic to a specific element; however, it can vary slightly depending on its exact chemical environment. For example, ions with a higher oxidation state experience a higher effective nuclear charge, making it harder to remove the core electrons, resulting in a higher binding energy. E_B is often defined as the difference between the final state energy (E_{FS}) and the initial state (or ground state) energy (E_{IS}) of a species with n electrons, as described by the following equation:

$$E_B = E_{FS}(n-1) - E_{IS}(n). \tag{2}$$

Early analysis of the theory behind XPS had a basic approach, based on Koopmans's Theorem,[149] in which it is assumed the electron orbitals remain unchanged during the photoemission process, therefore suggesting that the binding energy is dominantly influenced by the initial state effects. However, it is now well understood that the final state effects have a more significant influence.[150] Final state effects include binding energy shifts caused by the re-arrangement of the remaining (n-1) electrons, lifetime broadening, spin-orbit coupling, satellites and multiplet splitting and all need to be considered when analysing XPS spectra.

After the loss of a core electron from photoionisation, the core-hole is then filled by an electron from a valence orbital. The core hole therefore has a finite lifetime, which creates an energy of uncertainty of the emitted photoelectron. According to the Heisenberg uncertainty principle, the core hole lifetime influences peak width (lifetime broadening), *i.e.* core holes with shorter lifetimes lead to broader spectral peaks.[151] Generally, the lifetime decreases with increasing binding energy for the same orbital type, for example the O 1s peak (~530 eV) will experience higher lifetime broadening than the C 1s peak (~284 eV).

The process of filling a core hole with a valence electron releases energy that is then transferred to another electron, which is subsequently ejected from the sample (**Figure 2.4**). This is referred to as the Auger effect, and results in Auger peaks in an XPS spectrum. Similarly to the photoelectron peaks, the Auger peak position, shape and intensity can also provide information on the chemical environment of the probed element. However, unlike the photoelectron peaks, the kinetic energy of an Auger electron is independent of the photon energy.

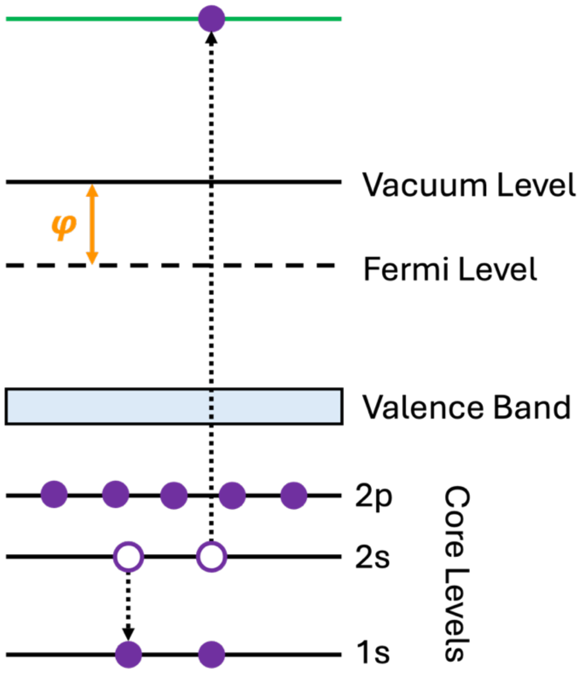

Figure 2.4. Diagram of the Auger electron emission process.

Spin-orbit coupling (J), another final state effect, occurs in orbitals with an orbital angular momentum of L > 0 (*i.e.* p, d and f orbitals). The spin (s) of the excited electron combines with the orbital angular momentum resulting in peak splitting, often appearing as a doublet peak, where $J = L + s$ ($s = \pm \frac{1}{2}$). The nomenclature of the doublets is written as nL_J (n = principal quantum number).

Examples of Zn and Fe 2p doublets can be seen in **Figure 2.5**, in which the metal 2p orbitals split into $2p_{3/2}$ (higher E_B) and $2p_{1/2}$ (lower E_B) peaks. Their relative intensities are dependent on the degeneracy of the split states, *e.g.* the 3/2 and 1/2 p orbitals and 5/2 and 3/2 d orbitals have intensity ratios of 2:1 and 3:2, respectively. The difference in E_B between the split peaks increases with increasing binding energy (i.e. increasing atomic number and decreasing n), for example a ~13 eV difference in observed in Fe 2p peaks, compared to Zn 2p which has a larger E_B gap of ~23 eV (**Figure 2.5**). The magnitude of splitting in small atoms can be as low as $\Delta E_B < 1$ eV which, depending on the experimental resolution, can be too small to resolve.

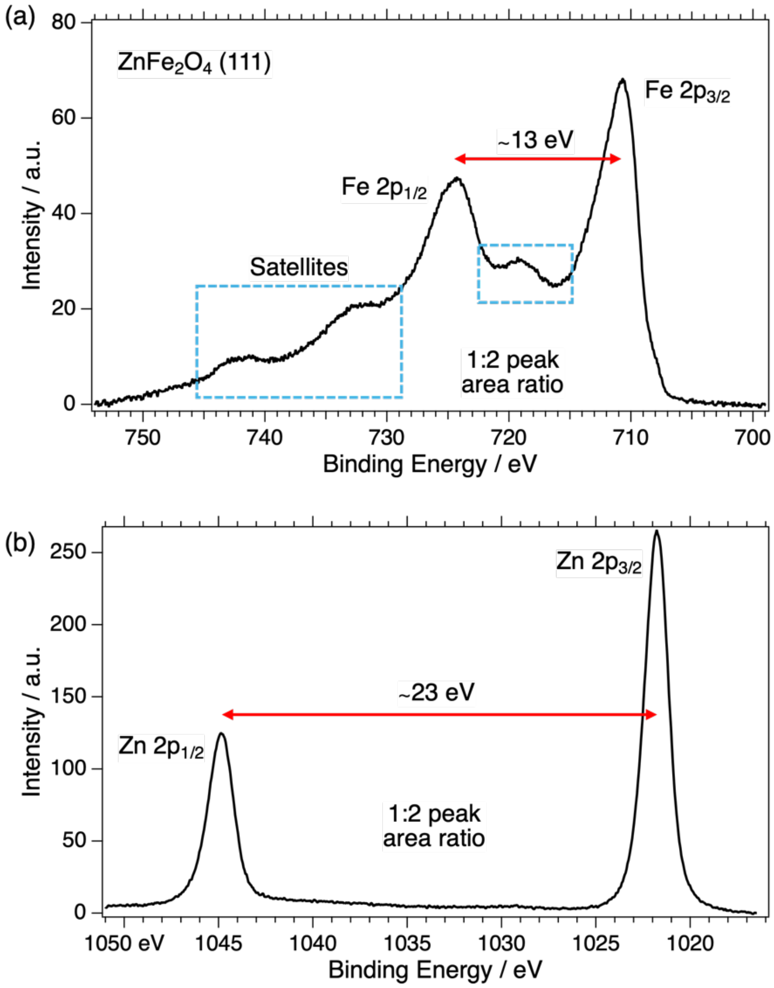

Figure 2.5. The (a) Fe 2p and (b) Zn 2p XPS of a $ZnFe_2O_4$ (111) surface measured at photon energies of 840 and 1190 eV, respectively. The binding energy difference of the doublets is highlighted by the red arrows and the satellites of Fe 2p are shown by the blue dashed boxed.

Multiplet splitting is another splitting effect that occurs in systems that contain unpaired d electrons, such as transition-metal spinels. It is caused by the interaction between the unpaired core electrons created by the photoionisation process and the unpaired electrons in the outer shell. This can result in a number of final states which then manifest in the relative XPS spectra. The multiplet splitting effect can make data fitting difficult, particularly in systems with mixed oxidation states, geometry and coordination numbers of the same atom, such as magnetite (Fe_3O_4).[152, 153] This complexity can often lead to misinterpretation and incorrect peak fitting, which is commonly observed in the literature. Multiplet splitting also needs to be considered in X-ray absorption spectroscopy of open-shell systems.[154]

When the photoelectrons leave the sample they can interact with other electrons in the system, reducing their E_{kin} and therefore resulting in a continuous inelastic background. The background appears as a 'tail' which extends to higher binding energies after the photoemission peak. The further the X-ray penetrate the sample increases the probability of inelastic scattering, which therefore increases the background. The inelastic effects need to be considered when quantitively studying photoemission peaks. Typically, two types of background removal are used: linear or Shirley.[155-157] The linear background removal uses a straight line to interpolate between intensities before and after the XPS peaks. This method is suitable for 1s peaks, however, is limited in its use for more complex spectra. The Shirley background is calculated considering the background intensity to be proportional to the integrated peak intensity at higher kinetic energies, producing a smooth curve rather than a linear line. More sophisticated approaches of background removal exist, (*e.g.* the Tougaard [158] or Shirley-Végh-Salvi-Castle [159, 160] approaches) however, for the work presented in this thesis the original Shirley method was used, an example of this can be seen in **Figure 2.6**.

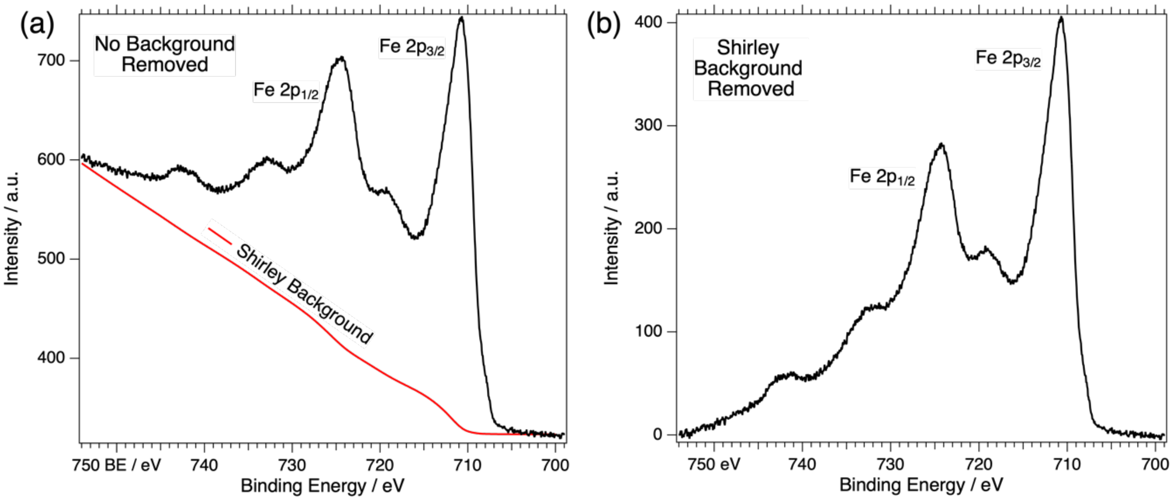

Figure 2.6. Examples of Fe 2p XPS peaks of a $ZnFe_2O_4$ (111) surface measured at a photon energy of 840 eV with (a) no background removal and the relative Shirley background and (b) with the Shirley background removed.

Discrete excitations can also occur during the XPS process and, unlike the inelastic background, appear as satellite peaks. They are found at higher binding energies with respect to the photoelectron peaks and can provide information on the electronic properties (*e.g.* oxidation state) of an atom or material. “Shake-up” satellites occur when a valence electron moves to a higher unoccupied orbital during the photoemission process. This reduces the E_{kin} of the emitted photoelectron resulting in a satellite peak with a higher E_{B} with respect to the main photoelectron feature. An example can be seen in the Fe 2p peaks, as demonstrated in **Figure 2.5**. Shake-off satellite peaks are similar to shake-up peaks but are caused by the ejection of a valence electron. These features tend to have a higher E_{B} compared to shake-up peaks and are often broader meaning they can be difficult to distinguish from the background. Plasmon satellite features can occur due to the collective excitation of all electrons in a material (plasmons), which can cause energy loss to the emitted photoelectrons. This effect usually results in multiple satellite peaks higher in E_{B} than the main photoelectron peaks. If the X-ray source is not completely monochromatic, weaker X-ray lines can excite photoelectrons creating peaks of different binding energies, which are referred to as X-ray satellites. Unlike the previous satellites discussed, these can be at a higher or lower E_{B} with respect to the photoelectron peaks. They are more common in lab-based XPS but can also be present in synchrotron-based measurements, usually due the presence of higher order harmonics of the selected photon energy.

The XPS peak intensities are proportional to the concentrations of the specific element, however quantifying the number of atoms can be difficult as there are other influencing factors. X-ray sources with greater intensities, such as synchrotrons compared to lab-based sources, result in more intense peaks. The photon flux affects the peak intensity, with higher flux resulting in more intense peaks. The efficiency of the detector can also cause variations in peak intensity. Another factor that needs to be considered is the photoionisation cross sections, which is the probability of a photoelectron being excited at a certain photon energy. The magnitude of the cross section is element and orbital specific. Yeh and Lindau [161] published the cross section corrections of elements with the atomic number of 1 to 101 in the photon energy range 1 to 1500 eV. Scofield [162] independently published this data with the photon energy range extending to 1500 keV. The XPS intensities need to be corrected with respect to the cross section to be able to conduct quantitative analysis. Digitised versions of the Yeh and Lindau and Schofield photoionisation cross sections have been made available by Kalha *et al.*[163, 164]

XPS is typically a surface-sensitive technique, with the information depth being dependent on the inelastic mean free path (IMFP, λ). The IMFP is defined as the distance that an electron beam with a given E_{kin} can travel in a particular material before its intensity drops to $1/e$ of its initial value, due to it losing energy from inelastic collisions. Materials with a higher density tend to have a lower IMFP. The probing depth of XPS is generally approximated as three times the IMFP (3λ), where the majority ($> 99\%$) of photoelectrons come from.[165] Due to the dependence on the E_{kin}, the probing depth can be altered by changing photon energy. Although the absolute IMFP varies with sample, there is a general trend with respect to the photon energy, known as the universal curve (**Figure 2.7**). The IMFP initially decreases reaching a minimum value and then begins to increase as the kinetic energy increases. The photoelectrons that are measured are an accumulation of those emitted from the deepest point in the bulk probed (E_{kin} dependent) to the sample surface, therefore the surface effects still need to be accounted for in bulk XPS analysis.

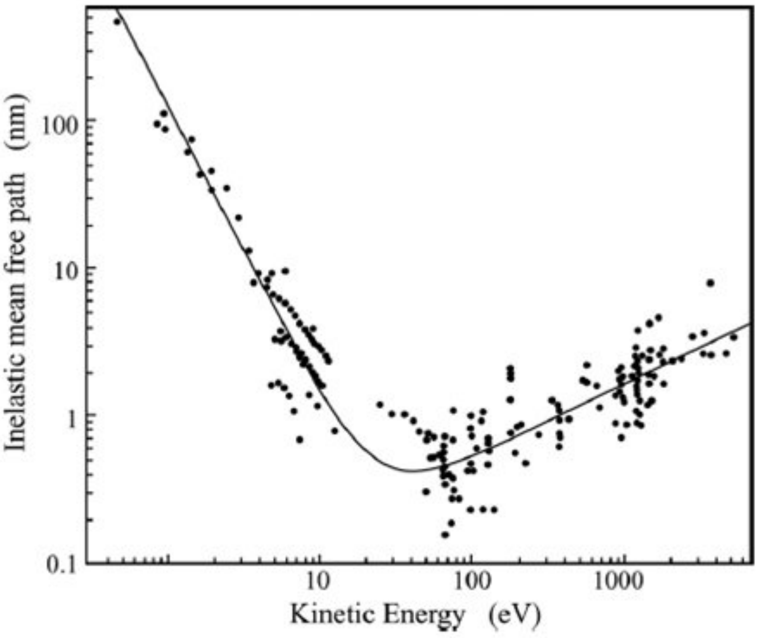

Figure 2.7. The inelastic mean free path (IMFP) universal curve as a function of kinetic energy. The data points shown are accumulated from various studies of different materials.[166, 167]

By analysing the binding energies, peak areas (intensities), and spectral shape of the core level XPS, it is possible to obtain information on the oxidation states, geometries and bonding of atoms within a material.

2.2.2 Instrumentation

XPS measurements are typically conducted under ultra-high vacuum (UHV) which ranges in very low pressures from 10^{-8} to 10^{-10} mbar. These conditions can be achieved using a series of scroll, turbo and ion pumps, the method used on the B07 beamlines. A key advantage to a UHV system is the minimisation of scattering caused by interaction with gas particles, therefore preventing the loss of photoelectron kinetic energy. It also reduces the risk of contamination (*e.g.* water or adventitious carbon), which is particularly important when conducting surface-sensitive techniques. However, in more recent years, near-ambient pressure XPS (NAP-XPS) has been prominent in spectroscopic research. This technique was built on foundational research conducted by Siegbahn *et al.* [168] and allows XPS measurements to be conducted under gas pressures of up to as high as 1 bar ,[169] which has been achieved on beamline P22 at PETRA.[170] NAP-XPS can therefore be used to replicate 'real life' conditions, which can be extremely beneficial in areas of research, such as electrochemistry [171-173] and catalysis.[174-176] Other possible experiments include *in-situ* studies of surface deposition, such as thin film growth, atomic layer deposition or chemical vapour deposition. Another advantage of near-ambient pressures is its potential to combat charging effects in insulating materials. Charging occurs when a positive charge accumulates on the insulator surface during photoemission, causing the photoelectron peaks to shift and broaden. This is a common occurrence under UHV conditions and the resulting XPS spectra can be difficult to interpret. To prevent this effect, the positive charge must be compensated for to neutralise the surface. This can be done with the use of an electron flood gun which directs low energy electrons towards the sample surface under UHV. NAP-XPS can also be used by introducing low pressures of gas (such as helium) to compensate for the positive charge, a method utilised on the B07 beamline (DLS).

Traditionally, laboratory sources are used to provide the monochromatic X-rays for XPS and are generated by irradiating a metallic anode with a beam of high-energy electrons. Various metals can be used for the anode, but the most common X-ray sources are Al K_α (1486.6 eV) and Mg K_α (1253.6 eV). A diagram of a typical lab-based XPS set up, including a hemispherical electron energy analyser, can be seen in **Figure 2.8**. The analyser shown consists of two hemispheres, the outer having a negative potential and the inner having a positive potential. The emitted electrons that enter the analyser will be attracted and repelled by the inner and outer hemispheres, respectively, forcing the electrons on a circular trajectory to the detector.

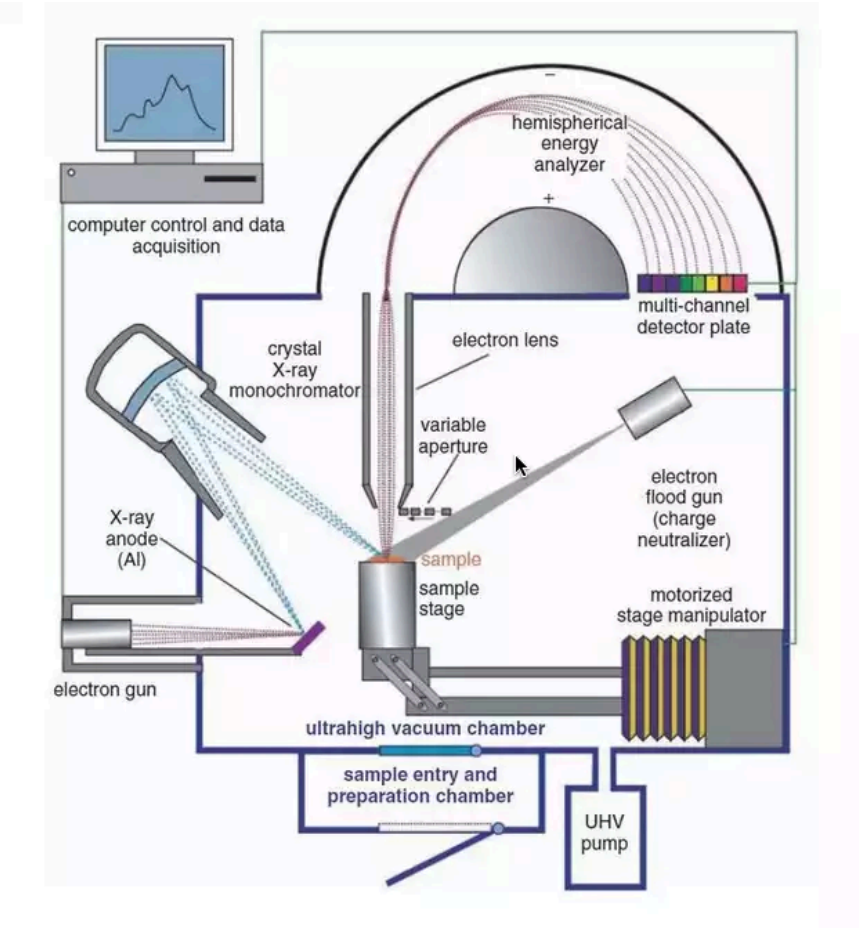

Figure 2.8. Diagram of a typical laboratory-based XPS set up.[165]

The fixed photon energies provided by lab-based sources can be limiting and present challenges. Therefore, use of synchrotron radiation for XPS can be beneficial and has many advantages, as mentioned in section *2.1.1*. For example, high flux (number of photons emitted per second) improves signal strength, sensitivity for weaker signals, and data acquisition time. Synchrotron radiation also has the ability to generate a variable photon energy range, from 'soft' X-rays (< 2 keV) to 'hard' X-rays (> 5 keV). A notable advantage of this is the ability to avoid overlap between the primary XPS and Auger peaks. Due to the fixed E_{kin} of the Auger peaks, one can select a specific photon energy to shift their effective binding energy to produce an XPS spectrum with no peak interference. This allows for easier analysis of both the photoemission and Auger peaks. Synchrotron XPS also generally achieves significantly improved resolution compared to lab-based XPS. Typically, the lab-based resolution is in the range of 300 – 900 meV,[177] whereas synchrotron XPS can reach resolutions below 50 meV.[178]

The information depth of XPS is directly related to the kinetic energy of the emitted photoelectrons. As previously discussed, the IMFP is dependent on the E_{kin} and the density of the material being measured. Photoelectrons with a higher E_{kin} can travel further through the material, therefore being able to escape from deeper in the bulk. Based on the photon energy equation in section *2.2.1* it is known that higher photon energies result in increased kinetic energies, *i.e.* increasing *hv* increases the XPS information depth. Different depths of XPS can also be probed using angle-dependent measurements.[179, 180]

The XPS data presented in this thesis were measured on the B branch of the B07 beamline (DLS).

2.3 X-ray absorption spectroscopy

2.3.1 Introduction

X-ray absorption spectroscopy (XAS) is a complementary technique to XPS that probes unoccupied states by studying the excitation of a core electron to a higher energy state. The XAS technique was initially developed in the 1970's, with groundbreaking work being published by Sayers *et al.*[181] and Eisenberger and Kincaid.[182] X-ray absorptions techniques are now commonly used across a wide range of research fields, such as catalysis, biomedicine and cultural heritage.[183]

Similarly to XPS, a photon beam is used to excite electrons within a sample, however the spectra are collected by measuring the absorption of the X-rays across a range of *hv*. XAS measurements therefore require a tuneable X-ray source, typically provided by synchrotron radiation. The intensity of the incoming X-rays (I_0) must be known. This is typically measured by passing the beam through a metallic mesh (*e.g.* Au or Ni), exciting photoelectrons which creates a signal proportional to I_0. The simplest and most efficient way to measure XAS is in transmission mode, where the X-ray intensity is remeasured as it passes through the sample (I_{trans}), usually by another mesh. A basic schematic of the X-ray absorption process in transmission mode can be seen in **Figure 2.9**. Transmission detection has the advantage of being able to measure the direct cross sections and doesn't experience any yield variation effects. However, there are significant limitations with respect to the sample. The sample must be thin enough for the X-rays to pass through (< few μm for soft X-rays) and variations in thickness or homogeneity can affect spectral shape. Generally, a photon energy of > 1 keV is required for transmission experiments.[184] In the soft X-ray regime, XAS is usually termed Near-edge X-ray Absorption Fine Structure (NEXAFS).

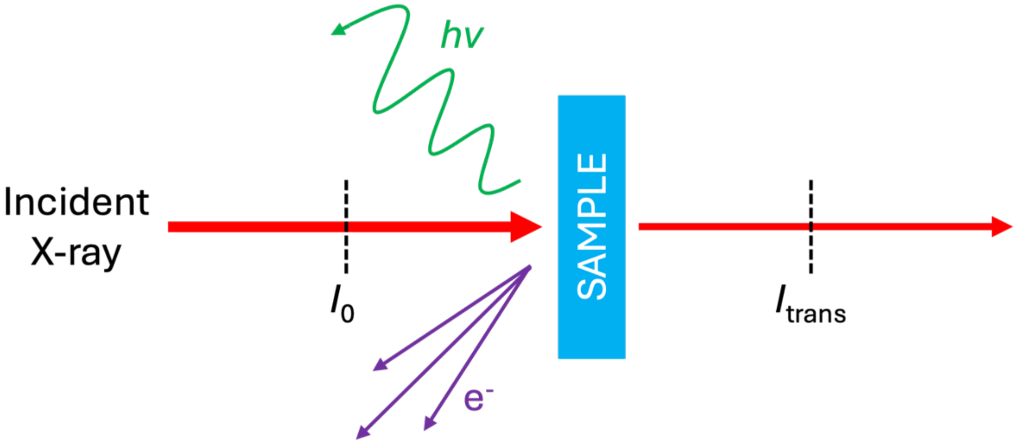

Figure 2.9. Diagram outlining the X-ray absorption spectroscopy (XAS) process by transmission mode and the secondary signals: emitted electrons and photons.

To avoid the challenges of transmission mode XAS, the absorption can be measured using the secondary signals from either emitted electrons or emitted photons (**Figure 2.9**). Total electron yield (TEY) measures all the electrons (photoemission and secondary) of all kinetic energies emitted from the sample, with the number of electrons emitted being proportional to the number of photons absorbed. The emitted electrons are either directly measured or measured by the current of electrons that flow back into the sample (which is equal to that of those emitted). TEY is a surface sensitive technique with information depths < 10 nm depending on the material being studied. Similarly to XPS, different depths can be probed by conducting angle-dependent measurements.[185-187]

The filling of the core hole left after photoemission (as described for XPS) can also result in photons that are emitted from the sample. Total fluorescence yield (TFY) measures the number of emitted fluorescence photons as a function of incident *hv*. The fluorescence emission is specific to the element and the electron transition. The fluorescence X-rays interact less with the material resulting in a greater escape depth (~100 nm) compared to emitted electrons.[184, 188, 189] This therefore means that TFY is more bulk sensitive than the electron yield techniques presented. **Figure 2.10a** shows the relative fluorescence and Auger yields for K and L_3 edges with respect to the atomic number. The fluorescence yields obtained for the L_3 edges of the elements with an atomic number $Z \leq 42$ is significantly less than the relative Auger yields. The yields are also shown as a function of photon energy in **Figure 2.10b**. At an energy of ≤ 2500 eV, the yield is also significantly less in fluorescence compared to Auger for the L_3 edge. This can therefore result in lower signal intensities and higher noise levels in L_3 edges collected by TFY compared to TEY.

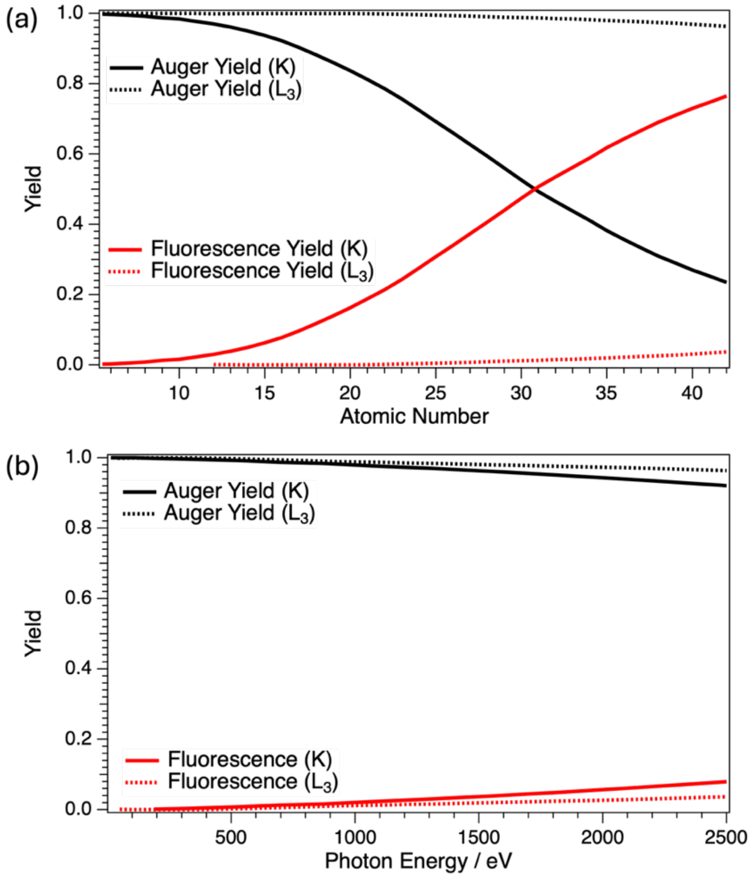

Figure 2.10. The relative Auger (black) and fluorescence yields (red) for the K and L_3 edges as a function of (a) atomic number and (b) photon energy.[190]

A major challenge that TFY presents is self-absorption, whereby the fluorescence X-rays are reabsorbed by neighbouring atoms within the material before being emitted from the sample. This can result in distortion of the spectral shape (*e.g.* flattening of peaks) and affect peak intensities making analysis difficult, this is especially prevalent in the soft X-ray regime. For heavier elements with strong absorption edges (*e.g.* transition metal L edges)[191, 192] the risk of these effects increases. An example of the effect of self-absorption can be seen in **Figure 2.11**. The Fe L edge of a $CoFe_2O_4$ nanoparticle measured in TFY mode shows distortion with respect to the peak intensities (particularly effecting the L_2 edge) compared to the edge measured in TEY mode.

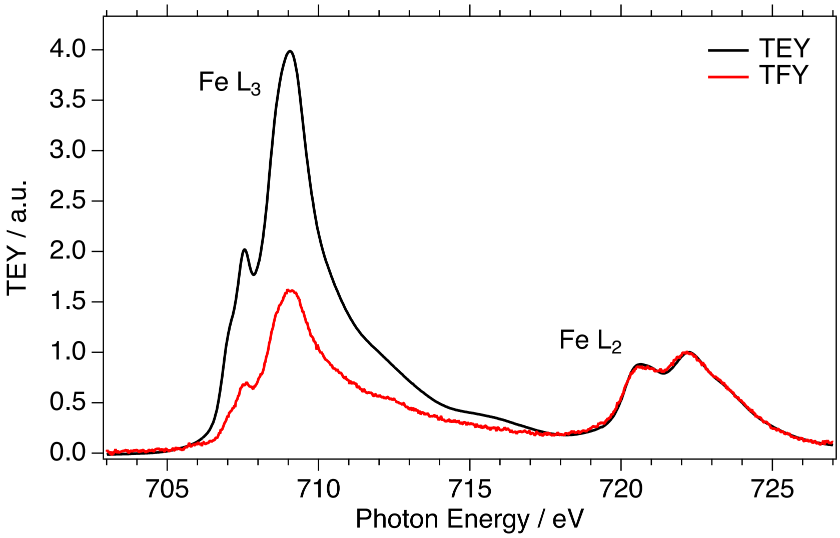

Figure 2.11 The Fe $L_{2,3}$ edge of a $CoFe_2O_4$ nanoparticle sample measured by TEY (black) and TFY (red) demonstrating the effect of self-absorption.

Similarly to the electron yield techniques, it is possible to selectively measure the intensity of a specific emitted X-ray fluorescence in a mode called partial fluorescence yield (PFY). An energy-resolving detector (a Vortex EM detector is used on the B07-B beamline) can measure a selected emission line from the resonant element (*i.e.* the same atom that is being excited by the incident photons). PFY can reduce the background and improve the spectral resolution, however, still suffers from self-absorption effects. Inverse partial fluorescence yield (iPFY) is a similar process however it measures the fluorescence emitted of a non-resonant element. Using iPFY eliminates the self-absorption effects seen in TFY and PFY, keeping the bulk sensitive character.[191]

In XAS a specific photon energy range is selected to excite core electrons from a specific core level, the resulting absorption edges are named corresponding to the level. The relative transitions and their names can be seen in **Figure 2.12**, where principal quantum numbers 1, 2, and 3 correspond to K-, L- and M- edges, respectively. For example, the excitation of core 2p electrons occurs at the $L_{2,3}$ edge, as seen in **Figure 2.11**.

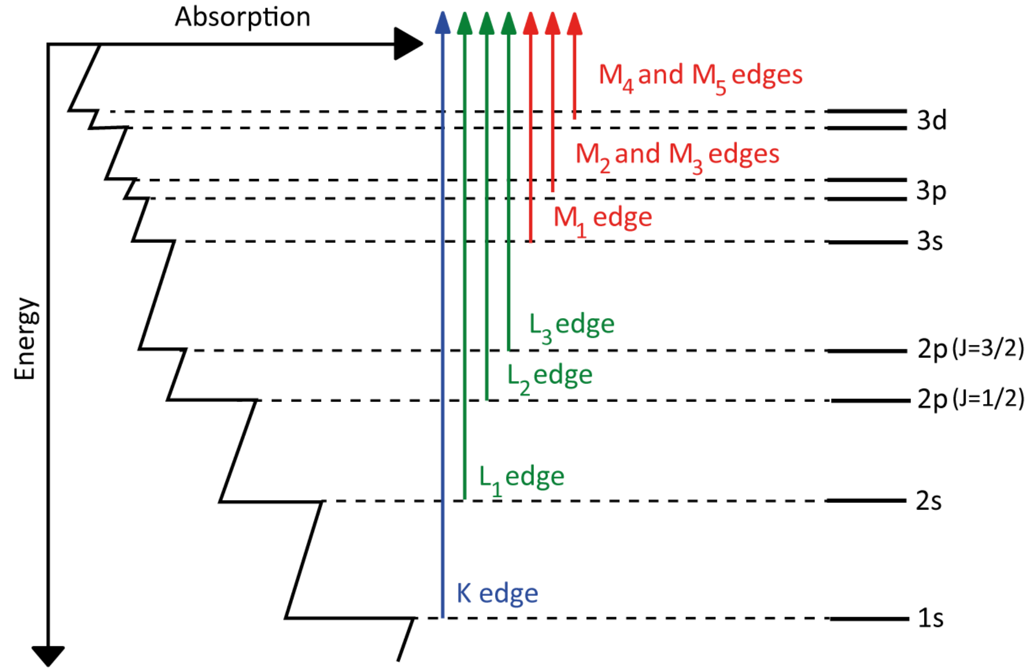

Figure 2.12. Schematic showing the XAS transitions with respect to the core level energies. Figure by Atenderholt [CC BY-SA 3.0 (http://creativecommons.org/licenses/by-sa/3.0), via Wikimedia Commons.

The NEXAFS data presented in this thesis was collected on the B branch of the B07 beamline (DLS).

2.3.3 X-ray magnetic circular dichroism

X-ray magnetic circular dichroism (XMCD) is a type of XAS experiment which measures the absorption of left- and right-circularly polarised X-rays. The XMCD is calculated as the difference between the absorption spectra measured using the right- and left-circularly polarised light, *i.e.* right minus left. In order to obtain spectra using this technique the sample must exhibit magnetism, *e.g.* Fe-based materials. The magnetic samples will absorb the differently polarised X-rays unequally, allowing for a difference in the spectra to be obtained easily. XMCD can not only be useful in determining the magnetic behaviours of an element in the sample, but it can also provide a better distinction between oxidation states and coordination numbers compared to NEXAFS. An example of a Fe L_3 edge of a $CoFe_2O_4$ nanoparticle sample can be seen in **Figure 2.13**, where the features highlighted are mainly attributed to a specific oxidation state and coordination of the iron cation. The spectral features are much easier to identify, compared to the Fe L_3 edge NEXAFS presented in **Figure 2.11**.

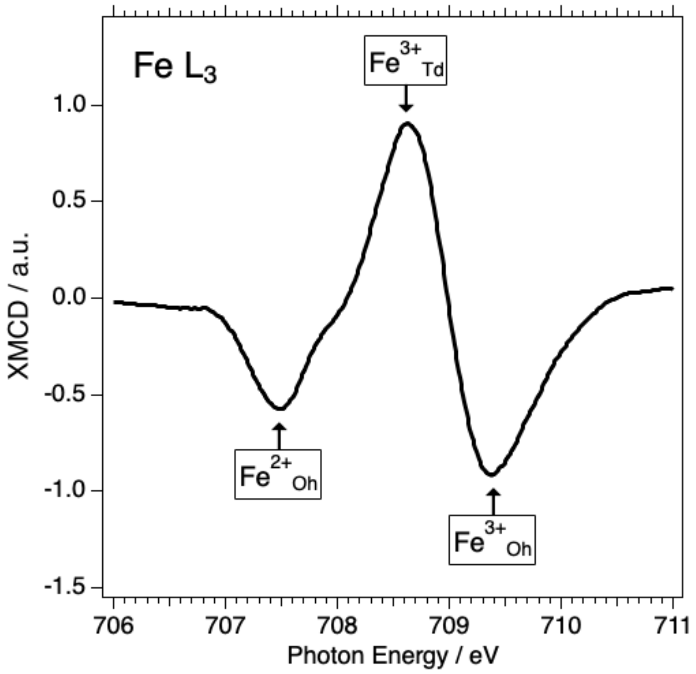

Figure 2.13. The Fe L_3 edge XMCD spectrum of a $CoFe_2O_4$ nanoparticle sample, with the relative Fe cations labelled.

The XMCD data presented in this thesis was collected at the I10 beamline (DLS).

2.4 Other experimental techniques

2.4.1 X-ray diffraction

Powder X-ray diffraction (PXRD) measurements were conducted to determine the bulk structure of the spinel nanoparticle samples as well as determining their crystallite sizes. The analysis of the PXRD patterns can provide information on the cation occupancy, however, does not describe their oxidation states. PXRD is typically undertaken using a Cu-anode lab source. This was used for the spinel measurements, as outlined in Chapters 4 and 6. However, challenges arose when studying the spinel samples containing metals with similar atomic numbers (*i.e.*

$CoFe_2O_4$, $ZnFeGaO_4$, $ZnGa_2O_4$) as for neighbouring atoms, such as Co and Fe, and Zn and Ga, their atomic scattering factors are very similar. The scattering factor *f* is described as the ratio of the amplitude of X-rays scattered by an atom with respect to that scattered by one electron under the same conditions.[193] Although it is mainly dependent on the atom type, the scattering factor also has a dependence on the scattering angle θ and the wavelength λ.[194] From **Figure 2.14**, it can be seen that atoms/ions with similar number of electrons will have comparable X-ray scattering factors and will be essentially indistinguishable from a standard PXRD experiment. Incorrect use of PXRD for determining cation distribution in spinel oxides is a reoccurring issue seen in the literature, and as a result the inversion degrees reported often need to be disregarded.

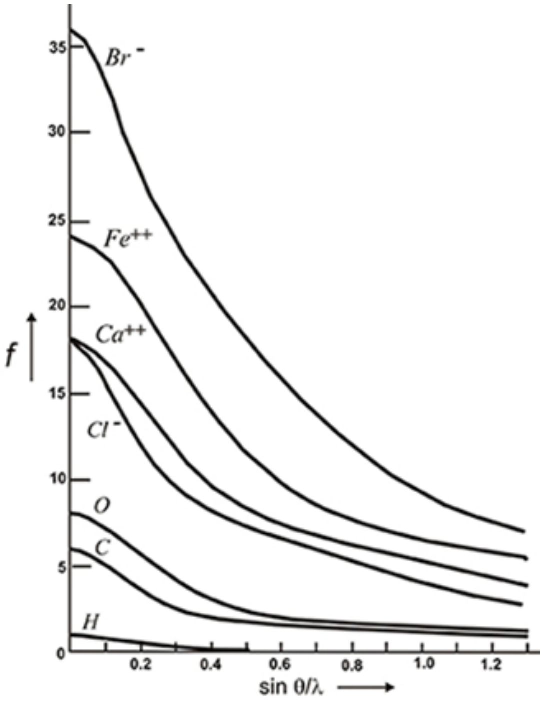

Figure 2.14. Scattering factor, *f*, as a function of scattering angle and wavelength for different ions.[195]

To distinguish between the Co/Fe atoms and be able to define a reliable inversion degree we conducted anomalous X-ray scattering (AXRS) on the cobalt ferrite spinels. In AXRS, an incident synchrotron X-ray source beam can be used to select a wavelength close to the absorption edge of a particular element. At these energies the total scattering factor of that element changes, allowing for differentiation between elements, such as Co and Fe.

The PXRD measurements outlined in this thesis were conducted at the ISIS Material Characterisation Laboratory on a Rigaku SmartLab diffractometer. The AXRS data presented were measured on the SpLine BM25 beamline at the European Synchrotron Radiation Facility (ESRF) and some preliminary results were measured on beamline I07 at DLS.

2.4.2 Low-energy electron diffraction

Low-energy electron diffraction (LEED) was used to characterise the surface of a zinc ferrite single-crystal (Chapter 5). In LEED, a beam of monochromatic low energy electrons (30 – 500 eV) is directed at the sample surface, the wave functions of the backscattered electrons interfere with each other resulting in a diffraction pattern, which can be detected by a fluorescence screen. The general set up of a LEED system can be seen in **Figure 2.15a**. The pattern produced is essentially an image of the reciprocal lattice, and therefore can provide information on crystallinity, lattice constants and surface symmetry. An example pattern of a $ZnFe_2O_4$ (111) single-crystal is shown in **Figure 2.15b**. LEED can also detect surface reconstructions with respect to the bulk material, as they cause changes in the surface periodicity leading to additional or shifted diffraction spots. LEED is a very surface sensitive technique with a low penetration depth of a few only angstroms.

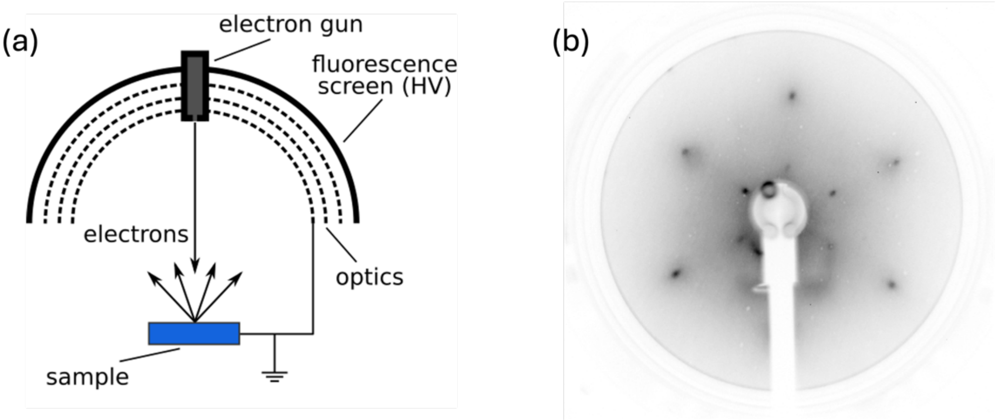

Figure 2.15. (a) Basic diagram of a LEED set up [196] and (b) an example LEED pattern of a $ZnFe_2O_4$ (111) single-crystal surface (measured at 75 eV).

The LEED measurements presented in this thesis were conducted on the offline UHV sample preparation chamber on the C branch of B07 (DLS).[144]

2.4.3 Catalytic testing

A crucial part of the project was determining if the spinel samples showed catalytic activity for the water splitting process or either of the half reactions. The catalytic testing on the powder spinel samples was conducted at the catalysis hub, based at the research complex at Harwell. The specific details of the experimental processes used are outlined in Chapters 4 and 6.

2.4.4 Scanning tunnelling microscopy

Scanning Tunnelling Microscopy (STM) is an imaging technique that can produce high resolution images of a sample surface at the atomic scale. Unlike electron microscopic techniques (*i.e.* scanning electron microscopy or transmission electron microscopy), STM uses an atomically-sharp probe to build the surface images. A low voltage (1-3 mV)[197] is applied to a metal tip which is held closely to the surface (< 1 nm), allowing the electrons to 'tunnel' between the tip and surface. The tunnelling current (nA) is measured across the sample building a map of surface structure. The general set up of STM can be seen in **Figure 2.16**.

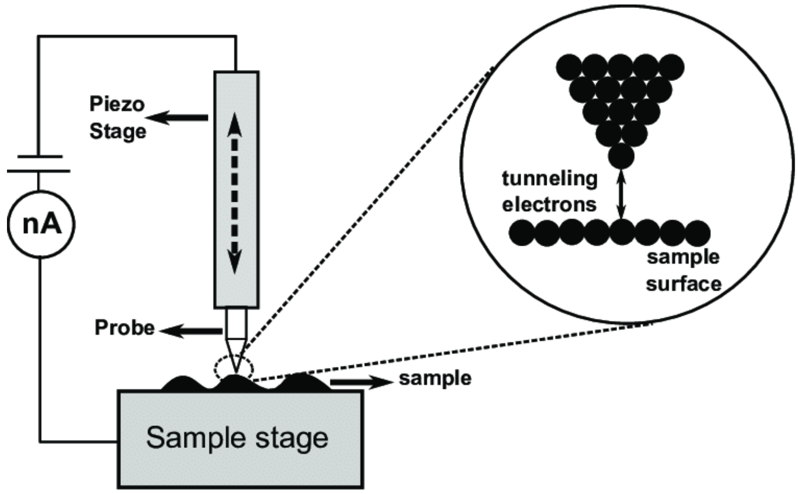

Figure 2.16. Diagram of the scanning tunnelling microscopy (STM) set up.[198]

The STM measurements were conducted at the University of Reading using an Oxford Instruments variable-temperature STM.

3. Computational Methods

3.1 Introduction

Computational simulations are widely used within scientific research and can be applied across many disciplines. Not only can they replicate real-world scenarios (*e.g.* complex structures and reaction mechanisms), but they can also predict experimental outcomes and guide future research. Modelling can also provide useful insights and support analysis of experimental data, in fields, such as spectroscopy,[154, 199-201] crystallography,[202, 203] and microscopy.[204-206]

The history of molecular modelling dates back as far as 1808, where Dalton began to create two dimensional visualisations of atoms on paper.[207] It was not until 1952 that the first 3D structure representations (Newman projections) were established.[208] The 1950s saw the development of the first computers with sufficient power to conduct theoretical calculations. This development was accelerated in World War II where ENIAC, the first general-purpose programmable digital computer, was built at the University of Pennsylvania. In the following decades computational research became much more advanced, with development of high processing power computers (supercomputers) and specialised, high-performance software. It was not until 1998 when the first Nobel prize was awarded in theoretical chemistry to Pople and Kohn for the "development of computational methods in chemistry" and the "development of the Density Functional Theory", respectively.

There are currently a wide range of computational chemistry techniques available, spanning from quantum-level methods, such as Density Functional Theory (DFT) and molecular dynamics, to data driven and artificial-intelligence-based approaches like machine learning. These computational techniques play an important role in current scientific research, with a notable recent example being the use of simulations and modelling during the COVID-19 pandemic.[209, 210]

3.2 The Schrödinger equation

Quantum mechanics have been applied in computational chemistry to investigate the structures and properties of molecules and compounds for many decades. However, the fundamental equation of these methods was first published in 1926 by Erwin Schrödinger, describing the quantum mechanical behaviour of a system in terms of its wavefunction, ψ. To determine ψ, which provides nuclear and electronic information about a given system, the time-independent, non-relativistic Schrödinger equation needs to be solved:

$$\hat{H}\psi = E\psi \tag{3}$$

where $\hat{H}$ is the Hamiltonian operator and E is the energy states of the system. The Hamiltonian represents the total energy of a particular system, including kinetic and potential energies. The Schrödinger equation can only be solved exactly for very simple systems, such as the hydrogen atom. For more complex systems approximations need to be considered.

The Born-Oppenheimer approximation[211] can be applied and allows for the separation of the nuclei and electron motion based on their significant difference in mass. By considering the nuclei as having fixed positions, it is possible to calculate the lowest energy state of the electrons in a particular system. This approximation is described by the following equation:

$$\hat{H} = -\sum_{i=1}^{N}\frac{1}{2}\nabla_i^2 - \sum_{i=1}^{N}\sum_{A=1}^{M}\frac{Z_A}{\mathbf{r}_{iA}} + \sum_{i=1}^{N}\sum_{j>i}^{N}\frac{1}{\mathbf{r}_{ij}} \tag{4}$$

where N and M are the total number of electrons and nuclei in the system, respectively. Z_A is the atomic number of nucleus A, $\mathbf{r}_{iA}$ is the distance between electron i and nucleus A, and $\mathbf{r}_{ij}$ is the distance between electrons i and j. The first term describes the kinetic energy of the electrons, the second is the Coulombic attraction between the electrons and nuclei, and third term describes the Coulombic repulsion between the electrons.

Even with the application of the Born-Oppenheimer approximation, solving the Schrödinger equation is still a difficult task. The electron wavefunction is a function of the spatial coordinates of every electron in the system, *i.e.* $3N$ variables (neglecting electron spin). We also need to consider the number of electrons in a system, which is considerably larger than the number of nuclei (M). When studying a seemingly simple molecule, such as CO_2, the full wavefunction is a 66-function, with each of the 22 electrons having 3 dimensions. When looking at a larger system, such as the conventional unit cell of $ZnFe_2O_4$ (912 electrons) investigated in this thesis, the full wave function requires a significant total number of dimension (2,736 functions). Another layer of complexity is added when considering the Hamiltonian, as the wavefunction of an electron cannot be found without also considering the wavefunctions of the other individual electrons in the system simultaneously.

A more fundamental issue of solving the Schrödinger equations is that the wavefunction of a particular group of electrons cannot be directly determined. However, in principle this can be quantified by measuring the probability of the N electrons being in a particular position. To characterise the electronic structure, the closely related electron density at a particular position in space, $\rho(\mathbf{r})$, can be used instead. This can be expressed in terms of the individual electron wavefunctions:

$$\rho(\boldsymbol{r}) = 2\sum_{i} \psi_i^*(\mathbf{r})\psi_i(\mathbf{r})\,. \tag{5}$$

The term inside the summation covers all the individual electron wavefunctions that are occupied by electrons and is the probability than an electron in individual wavefunction $\psi_i(\mathbf{r})$ is in position $\mathbf{r}$. This is of a factor of 2 because (in a closed-shell system) each individual wavefunction is occupied by two electrons with opposite spin. The approximations presented here provided a foundation for the advancement in computational modelling.

3.3 Density functional theory

3.3.1 Introduction

Density Functional Theory (DFT) has been prevalent in the quantum-mechanical-simulation field since its first introduction in the 1960's. The basis of DFT is built on two fundamental theorems presented by Hohenberg and Kohn.[212] Their first theorem states that the ground state energy from the Schrödinger equation is dependent on a unique functional of electron density, $\rho\,(\mathbf{r})$:

$$E = E[\rho(\mathbf{r})]. \tag{6}$$

In simpler terms, this theorem suggests that the electron density describes all properties of a system, including the wavefunction, allowing the Schrödinger equation to be solved using a function of only 3 spatial variables, $\rho(\mathbf{r})$. However, this theorem does not define the actual functional.

The second Hohenberg and Kohn theorem defines an important property of the functional and states that the electron density that minimises the energy of the overall functional is the true electron density corresponding to the full solution of the Schrödinger equation.

$$E[\rho(\mathbf{r})] \geq E[\rho_0(\mathbf{r})]. \tag{7}$$

This suggests that the electron density can be varied until the energy given by the functional is minimised, therefore allowing the ground state density and corresponding energy to be determined. However, the exact form of the functional was still undefined.

Kohn and Sham further built on the Hohenberg and Kohn theorems and presented the Kohn-Sham equation.[213] To compute the electron density and energy they replace the real system with a fictitious system of non-interacting electrons that has the same ground-state electron density.[214] The introduction of Kohn-Sham orbitals compensates for the poor representation of the kinetic energy and wavefunctions of the interacting electrons.[215] The Kohn-Sham energy functional is expressed in the following equation:

$$E[\rho(\mathbf{r})] = T_{\mathrm{ni}}[\rho(\mathbf{r})] + V_{\mathrm{ne}}[\rho(\mathbf{r})] + V_{\mathrm{ee}}[\rho(\mathbf{r})] + E_{\mathrm{xc}}[\rho(\mathbf{r})]. \tag{8}$$

The four terms on the right-hand side of the equation describe the kinetic energy of the non-interacting electrons, the electron-nuclei attraction, the electron-electron repulsion, and the exchange correlation energy, respectively. Unlike the other terms, the exchange correlation energy includes the quantum mechanical effects and defining it is an extremely difficult task, and therefore further approximations need to be considered.

3.3.2 Exchange correlations functionals

The development of exchange correlation functionals has been crucial in the advancement of quantum simulations and remains an active area of research with the aim of improving the accuracy and efficiency of DFT. The current functionals that exist vary in quality and accuracy, generally with the better functionals being more computationally expensive.

The Local Density Approximation (LDA) is considered the simplest approximation to employ in DFT and is computationally cheap compared to other DFT approaches. LDA considers systems as locally homogenous and assumes that the exchange-correlation energy per particle at any given point of space is a function of the electron density at that point. The exchange correlation, $E_{\mathrm{xc}}^{\mathrm{LDA}}$, is defined by the equation:

$$E_{\mathrm{xc}}^{\mathrm{LDA}}[\rho(\mathbf{r})] = \int d^3\mathbf{r}\rho(\mathbf{r})\varepsilon_{\mathrm{xc}}^{\mathrm{LDA}}\big(\rho(\mathbf{r})\big). \tag{9}$$

Although LDA is relatively efficient for modelling the exchange-correlation effects in systems with slowly varying densities (*e.g.* bulk metals or uniform electron gas), it provides poor accuracy for inhomogeneous systems, which leads to systematic errors, such as over binding and underestimated band gaps.

In order to improve on LDA, the inhomogeneity of the electron density needs to be considered. The generalised gradient approximation (GGA) includes both the electron density and its spatial gradient (the first derivative with respect to its position) to calculate the exchange-correlation energy per particle:

$$E_{\mathrm{xc}}^{\mathrm{GGA}}[\rho(\mathbf{r})] = \int d^3\mathbf{r}\rho(\mathbf{r})\varepsilon_{\mathrm{xc}}^{\mathrm{LDA}}\big(\rho(\mathbf{r})\big)\, F\big(\rho(\mathbf{r}), \nabla\rho(\mathbf{r})\big) \tag{10}$$

The gradient correction factor, $F\big(\rho(\mathbf{r}), \nabla\rho(\mathbf{r})\big)$, depends on the local density and spatial gradient of the electron density. GGA can better capture how the densities vary in space compared to LDA. The early development of GGA functionals was mainly empirical and involved fitting to experimental or high-level theoretical data, which in some cases could limit their general applicability. To address this issue, non-empirical functionals were subsequently developed. The most commonly used functionals for calculating solids are the Perdew-Wang (PW91)[216] functional and the Perdew-Burke-Ernzerhof (PBE)[217] functional. PBE defines the exchange correlation functional by using consistent theoretical principles, improving the transferability across different systems. PBE also provides more accuracy for properties, such as bond lengths, surface energies and chemical bonding, compared to LDA and early GGA functionals. Over the years modifications to improve the functional have been implemented, such as the revPBE[218] and PBEsol.[219] However, the standard PBE functional was suitable for the work conducted in this thesis.

GGA is a useful functional in delocalised systems where the electrons do not strongly interact with themselves. However, self-interaction becomes a challenge in systems containing strongly localised d or f orbitals, for example in transition metals.[220] A way to overcome this is to include Hubbard corrections to the generalised gradient approximation (GGA+U).[221, 222] The *U* parameter selectively provides an energy correction to the localised d electrons within a particular system, suppressing the hybridisation of the d orbitals with those of the ligands. This penalty counteracts the artificial delocalisation of the d orbitals that results from the self-interaction problem. The GGA+U method provides an improved energy for systems with self-interaction compared to GGA; however, there are still limitations with this method, as it only corrects specific orbitals (e.g. the d orbitals in a transition metal) and requires adequate *U* values to be found (often empirically or with the help from higher-accuracy calculations).

Hybrid functionals not only provide a higher quality exchange-correlation but can also provide an improved correction for self-interaction compared to GGA+U. Hybrid functionals work by combining GGA functionals with the Hartree-Fock (HF) exact exchange. HF theory uses a Slater determinant to express the multielectron wavefunction in terms of single-electron wavefunctions. Although HF calculates the exchange energy accurately, its overall accuracy is limited when studying complex systems because it neglects the wider electron correlation effects. In a hybrid functional both the exchange energy (from HF) and the electron correlation (from DFT) can be accounted for, resulting in improved accuracy in calculating molecular and electronic properties. Commonly used hybrid functionals include the empirical B3LYP functional[223, 224] (where the proportions of LDA/GGA/HF contributions are chosen to match experimental properties of small molecules), as well as the non-empirical functionals PBE0 (after Perdew-Burke-Ernzerhof)[225] and HSE06 (after

Heyd-Scuseria-Ernzerhof).[226] The PBE0 hybrid functional includes exactly ¼ of HF exchange. The HSE06, on the other hand, also uses ¼ of HF exchange, but only for short-range electron interactions; at longer range the PBE exchange is exclusively used, leading to better convergence properties. The HSE06 method significantly improves the accuracy and efficiency of calculations in solids (where long-range HF is less necessary), particularly improving band gap predictions. HSE06 was employed in the electronic structure calculations presented in this thesis.

Beyond these functionals there have been some more sophisticated exchange-correlation functionals developed, however these can some at significantly higher costs, particularly when working in larger cells. For the DFT calculations that were conducted in this thesis, the use of GGA+U and hybrid functionals provided a suitable level of accuracy.

3.3.3 Pseudopotentials and the projector augmented wave method

The physical properties and chemical bonding of a material are primarily determined by the valence electrons in the atoms and the more tightly-bound core electrons play a minimal role. Therefore, the number of planewaves required for a DFT calculation can be significantly reduced by only considering the valence electrons. Pseudopotentials replace the combined effect of the core electrons and nucleus with an effective potential to accurately reproduce their influence on the valence electron.[227] Including pseudopotentials significantly reduce the cost of DFT calculations.

The projector augmented wave (PAW) method[228, 229] is analogous to pseudopotentials, and was used in calculations throughout the project. The PAW method combines and all-electron approach with a frozen-core method; i.e. the core electrons are included in the calculation, but their wavefunctions are kept at the isolated atom reference states. The PAW is widely used in DFT calculations of solids, as it provides high accuracy at relatively low costs. The PAW method has also proved to perform particularly well for the complex behaviour exhibited by d- and f-block elements.[230]

3.3.4 Dispersion corrections

Dispersion forces, or van der Waals' forces, are a non-local correlation effect. Due to the local/short-range nature of the GGA functional, non-local correlations are neglected and therefore long-range dispersion forces are not accounted for. Therefore, an additional empirical energy term related to the dispersion interaction (E_{disp}) is often added to the DFT energy (E_{DFT}):

$$E_{\mathrm{total}} = E_{\mathrm{DFT}} + E_{\mathrm{disp}} \tag{11}$$

The E_{disp} term contains contributions from all atom pairs in the system, with the magnitude of the contributions decaying as R^{-6}, where R is the distance between atoms. There is a range of high-quality dispersion correction methods available. The calculations in this thesis used Grimme's D3 method,[231] where the coefficients in front of the R^{-6} term are geometry-dependent, in the sense that they are calculated on the basis of the coordination number around the interacting atoms.

3.3.5 Reciprocal space and k points

The periodicity of the crystal structure is fundamental to how electrons behave in solids and leads to the concept of reciprocal space. While real space describes the positions of atoms and lattice vectors, reciprocal space describes the wave-like properties of electrons, particularly their wavevectors, denoted by **k**.

In the context of DFT calculations, the reciprocal space becomes essential because the electronic wavefunctions are periodic functions in **k**-space. These wavefunctions are labelled by wavevectors that belong to the Brillouin zone, which is the primitive unit cell of the reciprocal lattice. To calculate physical properties, such as total energy or charge density, one must integrate over the entire Brillouin zone. However, since it is computationally infeasible to evaluate an infinite number of **k**-points, we sample the Brillouin zone using a finite grid of **k**-points. Each **k**-point corresponds to a specific wavevector where the band structure is evaluated. The total electronic properties of the crystal are then approximated as a weighted sum over these discrete **k**-points. The choice of **k**-point mesh significantly affects the accuracy and computational cost of the DFT calculation. One commonly used method for generating **k**-point grids is the

Monkhorst-Pack scheme,[232] which simply provides a uniform sampling of the Brillouin zone. For example, in a cubic Brillouin zone, the Monkhorst-Pack scheme might correspond to a 4×4×4 grid of **k**-points. The necessary number of divisions in the grid is larger the smaller the real space cell is. It also depends on the nature of the material: metals require a denser sampling, while insulators and semiconductors tend to converge with fewer **k**-points. In general, it is recommended to check for the convergence of calculated properties with increasing grid density and use a grid that is large enough for the precision required. The DFT code used in this study efficiently parallelises calculations over the different **k**-points,[233] taking optimal advantage of highly-parallel supercomputers.

3.3.6 Slab models

Typically, calculations on structures, such as spinels are conducted using periodic boundary conditions to model the crystalline solids, representing the bulk material. For example, in this thesis the majority of the DFT calculations were conducted using the spinel primitive unit cell, as seen in **Figure 1.1b**. Increasing the cell size does not only increase complexity within the system but also significantly increase computational cost.

It is possible to model a surface by taking a 'slice' of a material that is finite in two dimensions, which is referred to as a slab model. They can be used to study effects, such as surface reconstruction, interface modelling and surface reactions. The slab model consists of two cleaved surfaces from the bulk material separated by a vacuum space, an example can be seen in **Figure 3.1**.

When building a surface model, the size of the vacuum space and slab thickness need to be considered. The vacuum space must be large enough to avoid interaction between the two surfaces either side of the slab, however, as the vacuum size increases as does the computational cost. Typically, a vacuum space of 10 Å is suitable, but the slab thickness required is somewhat dependent on the effect being studied. Like the vacuum size, the greater the slab thickness the better, however with an increasing number of layers in the slab comes a greater computational cost.

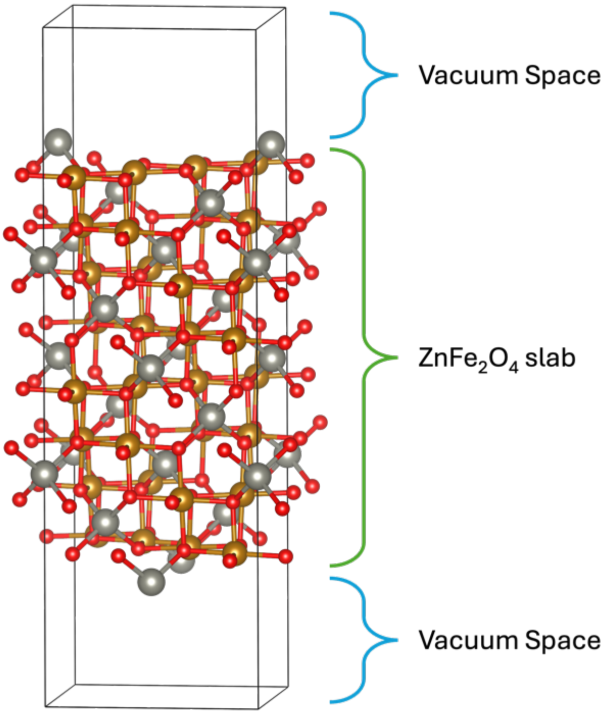

Figure 3.1. A slab model of a $ZnFe_2O_4$ $(100)_A$ surface with a 10 Å vacuum. Colour scheme: Zn = silver; Fe = gold; oxygen = red.

Maintaining symmetry in the surface model is often important for DFT simulations as it helps to remove dipole moments to ensure electrostatic stability. This can be challenging for materials with inherently polar terminations. The Tasker classification[234] categorises surfaces based on the charge distribution in the atomic planes, which therefore determines if a net dipole moment is present. Tasker type I surfaces contain an equal number of anions and cations in each plane resulting in a neutral charge and therefore no dipole moment. Type II surfaces have charged layers; however, due to the symmetrical stacking they also have no dipole moment. In the Tasker type III surface, the layers are also charged, but due to the stacking pattern there is a dipole moment perpendicular to the surface. **Figure 3.2** shows diagrams of each surface type. Surface construction can be used to eliminate the net dipole moment in a Tasker type III surface; however, this can be challenging to do whilst maintaining the materials stoichiometry.

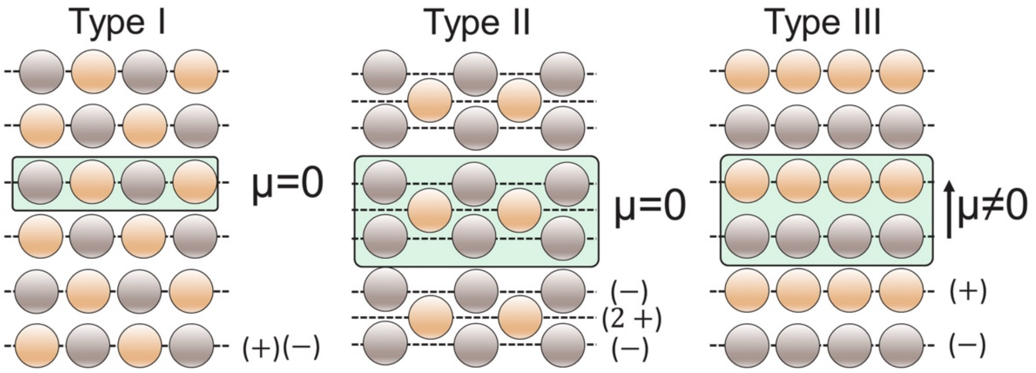

Figure 3.2. Type I, II, and III surfaces according to the Tasker classification, where μ is the net dipole moment.[235]

The spinels studied in this project are Tasker type III surfaces, which therefore required surface reconstruction. The specific details of how this was done are outlined in Chapters 4 and 6.

3.1.7 Vienna ab initio simulation package

The Vienna *ab initio* simulation package (VASP) is a widely used tool for performing techniques, such as molecular dynamics and DFT. All the DFT simulations presented in this thesis were conducted using VASP and the specific parameters used are outlined in the individual results Chapters 4, 5, and 6.

3.4 Semi-empirical simulations

3.4.1 Introduction

When it comes to calculating the core-level spectra of open-shell systems, such as transition metal spinels, the multiplet-splitting effect (Chapter 2, section *2.2.1*) needs to be considered in simulating spectroscopy data. However, DFT struggles to accurately describe this effect due to its limitations with respect to describing the electron interaction, particularly for localised d and f electrons. To model the XPS and XAS we therefore need to consider the use of semi-empirical methods,[154, 236] which are partially based on fundamental theory (*e.g.* quantum mechanics);

however, unlike first-principles DFT, they also require experimental fitting parameters.

3.4.2 The Hamiltonian

The basis of the semi-empirical method for simulating the spectral shape is to construct a Hamiltonian that considers the key interactions in the multiplet splitting effect. To simplify the calculations, the electron kinetic energy and nuclei interactions can be excluded because they are similar for all electrons within a given shell and do not affect the splitting structure. The simplified Hamiltonian can be described as:

$$\widehat{H} = \sum_{i\neq j} \frac{e^2}{\mathbf{r}_{ij}} + \sum_{N} \zeta(\mathbf{r}_i) L_i s_i + \sum_{k=0}^{2L} \sum_{m=-k}^{k} A_{k,m} C_k^m(\theta, \phi) \tag{12}$$

where the three terms describe the electron-electron interactions, spin-orbit coupling, and the crystal-field parameters, respectively. In this form of the Hamiltonian the electron-electron repulsion term is crucial in defining the multiplet structure. It can be solved by considering the radial (how the electrons interact) and angular (how the interaction varies with orbital orientation) components:

$$\sum_{i\neq j} \frac{e^2}{\mathbf{r}_{ij}} = \sum_{k}^{2l} \beta^k f_k F^k + \sum_{k} \beta^k g_k G^k \tag{13}$$

In this equation the Slater integrals, F^k and G^k account for the Coulomb repulsion between electrons in the same shell (*e.g.* 3d) and the exchange interaction between electrons with the same spin, respectively. These parts make up the radial components. f_k and g_k are the angular coefficients, which are dependent on the coupling of the angular momenta in different electron configurations. Scaling parameters, β^k, are used to account for screening and correlation effects which are not fully described by the Slater integrals. The angular components can be solved analytically from angular momentum theory, however the radial components are usually obtained from *ab initio* simulations and scaled with respect to experimental data (β^k).

The spin-orbit coupling term consists of the spin-orbit coupling constant ($\zeta(\mathbf{r}_i)$), the angular orbital momentum of electron i (L_i), and its spin angular momentum (s_i). The crystal-field term describes the interaction of the electrons with the surrounding ligand field. In equation 12, $A_{k.m}$ are the crystal-field parameters which define the symmetry and strength of the crystal-field and C_k^m defines the angular function.

One consequence of neglecting some terms in the simplified Hamiltonian, is that the absolute energy is not considered in the simulation. To compensate for this, the binding (XPS) or photon (XAS) energy shifts need to be determined experimentally or through a different computational method. For example, the relative energy shifts of the simulated Fe $L_{3,2}$ edges presented in this thesis were shifted with respect to the complimentary experimental work.

3.4.3 CTM4XAS

There are a number of options of freely available software for simulating core-level spectra of open shell systems, such as CTM4XAS [237] and Crispy.[238] They use the semi-empirical mutliplet approach implemented in Quanty, a quantum many-body script language developed for this purpose.[239] Although both CTM4XAS and Crispy were used for initial simulations, the calculated X-ray absorption edges presented in this thesis were primarily modelled using CTM4XAS. The specific parameters implemented can be seen in Chapter 4.

The simulations with CTM4XAS were conducted with support from Prof. Frank de Groot, during a research visit to Utrecht University.

4. Spinel ferrites MFe_2O_4 (M = Co, Cu, Zn) for photocatalysis: theoretical and experimental insights

Chapter Overview

Spinel ferrites exhibit significant promise for photocatalytic water splitting and their efficiency can be enhanced by A cation substitution. However, the complex properties of spinels, for example, the different behaviour of bulk and nanostructured materials, are not well understood. Here, we combine advanced computational and experimental methods with reactivity measurements to explore the inversion degrees, electronic structures, and photocatalytic activities of MFe_2O_4 spinels (M = Co, Cu, Zn). X-ray diffraction and anomalous X-ray scattering measurements determined bulk inversion degrees of 0.81, 0.91, and 0.26 for $CoFe_2O_4$, $CuFe_2O_4$, and $ZnFe_2O_4$, respectively. Photocatalytic tests showed that only $ZnFe_2O_4$ is active for the oxygen evolution reaction, which correlates with its favourable band alignment, as determined by DFT simulations. Surface-sensitive X-ray absorption spectroscopy measurements provided insights into the cation distributions at the surfaces, showing significant deviations from bulk properties, particularly in $ZnFe_2O_4$ in which 52% of the near-surface tetrahedral sites are occupied by Fe cations, compared to 26% in the bulk. DFT simulations of $ZnFe_2O_4$ illustrated how the surface terminations can alter the thermodynamic preference for cation distribution in comparison with the bulk. Our findings illustrate the complex interplay between surface and bulk properties in spinel ferrites. The work presented in this Chapter was published in *J. Mater. Chem. A.* (2024).

Statement of contributions

The work in this Chapter was a collaboration with Dr Ivan da Silva (IdS) and Dr Santosh Kumar (SK). The PXRD measurements and PXRD and AXRS data processing and Rietveld refinements were conducted by IdS. The catalytic activity measurements were conducted by SK.

4.1 Introduction

The work presented in this Chapter looks at the first key methods of spinel modification to enhance their catalytic ability: A cation substitution. Chapter 1 highlights the catalytic ability of the spinel ferrites MFe_2O_4, where M = Co, Cu or Zn,[68, 84, 111, 125, 240] with $ZnFe_2O_4$ showing significant efficiency in the HER.[66, 120] We use a combination of catalysis measurements and computational analysis to study the photocatalytic abilities cobalt, copper and zinc ferrite nanoparticle samples.

Previous work has suggested substantial differences in properties and cation distribution of spinel ferrites between bulk crystals and nanoparticles.[77, 106, 119] Understanding the properties that are inherent to the bulk materials and differentiating them from the effects of the surface is important in applications including photocatalysis, because both the bulk and the surface participate with different roles in the photocatalytic process. Therefore, we also conduct X-ray diffraction, X-ray absorption spectroscopy and DFT calculations to investigate and characterise the bulk and surface configuration of the three spinel samples. Computational modelling also offers insights on the departures from bulk behaviour seen in small nanoparticles due to different behaviour of bulk and surfaces in terms of the inversion degree.

4.2 Methods

4.2.1 *Ab-initio simulations of bulk and surface models*

The calculations were performed using density functional theory (DFT) as implemented in the VASP code.[241, 242] Geometry optimisations were performed using the generalised gradient approximation (GGA) with the Perdew-Burke-Ernzerhof (PBE) exchange-correlation functional.[243] Hubbard (GGA+U) corrections with U_{eff} values of 3.3 eV and 4.0 eV were applied to the Co and Cu/Fe d orbitals, respectively; these values were obtained by Wang *et al.*[244] via fitting to the experimental oxidation enthalpies of the corresponding binary metal oxides, and have been found to transfer well to the study of more complex oxides (*e.g.* $FeSbO_4$,[245] $LaCoO_3$ and $LaFeO_3$,[246] $YBa_2Fe_{3-x}Co_xO_8$,[247] and $BiFe_{1-x}Co_xO_3$[248]). The interaction between the valence and core electrons was described with the projector augmented wave (PAW) method.[249] An energy cut-off of 520 eV, 30% above the recommended value for the PAW potentials, was used for all geometry optimisations involving cell volume charges, to decrease the Pulay errors.

For the bulk calculations, primitive unit cells of MFe_2O_4 (M = Co, Cu, Zn) containing two formula units were modelled with inversion degrees of $x = 0$, 0.5 and 1, example models of $ZnFe_2O_4$ can be seen in **Figure 4.1**.

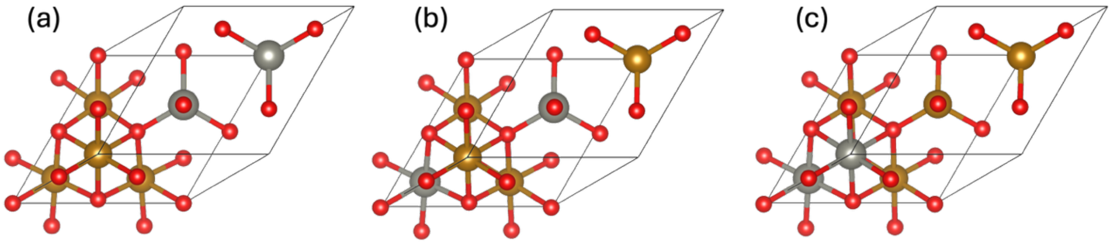

Figure 4.1. The models of the primitive unit cells of $ZnFe_2O_4$ with inversion degrees of (a) $x = 0$, (b) $x = 0.5$, and (c) $x = 1$ used for the DFT simulations. Colour scheme: Zn = silver; Fe = gold; oxygen = red.

For each inversion degree there is only one symmetrically different configuration in the primitive cell, therefore allowing us to calculate the inversion energy (configurational contribution only) as

$$\Delta E_{\text{conf}}(x) = E(x) - E(0). \tag{14}$$

The electronic structure calculations to determine the band gap and alignment of the most stable configurations were completed using the hybrid functional by Heyd, Scuseria and Ernzerhof (HSE06),[226] which includes 25% of Hartree-Fock exchange as well as range-separated screening with an attenuation parameter of 0.2 Å^{-1}. The HSE06 calculations used the geometries optimised at GGA+U level, *i.e.* we did not re-optimise the structures at HSE06 level (but we checked, using $ZnFe_2O_4$ as a test, that this is an acceptable approximation, leading to both cell parameters and band gaps very close, within 0.5%, to those obtained with the full HSE06 approach). The band alignment was calculated using the top of the valence band and the bottom of the conduction band in the HSE06 band structure.

In all calculations, the magnetic moment for Fe^{3+} (and for Co^{2+} in the case of $CoFe_2O_4$) was initialised in high-spin state.[9, 250] For $CoFe_2O_4$ there is an additional degree of freedom: both cobalt and iron cations can exist in 2+ or 3+ oxidation states; therefore, charge transfer could occur resulting in Co^{3+} and Fe^{2+} being present. Test calculations were completed in which charge transfer and different spin states of the cations were considered. In all cases, the structures were either higher in energy or converged back to the more stable Co^{2+}/Fe^{3+} high-spin configuration. Magnetic moment orientations were initialised at the magnetic ground state which was found by considering all the possible orientations of the moments. For $ZnFe_2O_4$ with a normal distribution, an antiferromagnetic configuration of the Fe^{3+} in Oh sites had the lowest energy. However, a ferromagnetic orientation of Fe^{3+} in Oh sites was most stable for normally distributed $CoFe_2O_4$ and $CuFe_2O_4$. For the ground state of all three spinels structures, when partially or fully inverse, the Fe^{3+} in Td sites had magnetic moments opposite to the moments of the Fe^{3+} in the Oh sites.

To simulate the (100) and (111) $ZnFe_2O_4$ terminated surfaces, four periodic slab models of $ZnFe_2O_4$ with different terminations separated by a vacuum gap of 10 Å were optimised using the same parameters outlined for the bulk GGA+U calculations. These are Tasker type-III surfaces, in which there is a dipole moment perpendicular to the surface which can only be eliminated by surface reconstruction.[234] Therefore, we need to modify the slabs to build stoichiometric, non-polar surface models, which are generally expected to be stable under neutral (not very reducing or very oxidising) conditions. Having stoichiometric and non-polar slabs is also important in our work because they are used to estimate the offset of the macroscopic electrostatic potential between the bulk and the vacuum level. However, it is generally possible to study deviations in stoichiometry, as done elsewhere for spinel oxides,[251-255] to understand the variation in surface stoichiometry with external conditions, such as the oxygen partial pressure; we have not conducted such analysis here. A schematic representation of the reconstructions of the surfaces for our study are shown in the **Figure 4.2**, and the notation for the stoichiometric non-polar surfaces follows the one used in Ref. [252]. The $(100)_A$ surface is Zn-terminated, whereas the $(100)_B$ surface ends at the Fe-O layer, with half of the layer atoms removed.

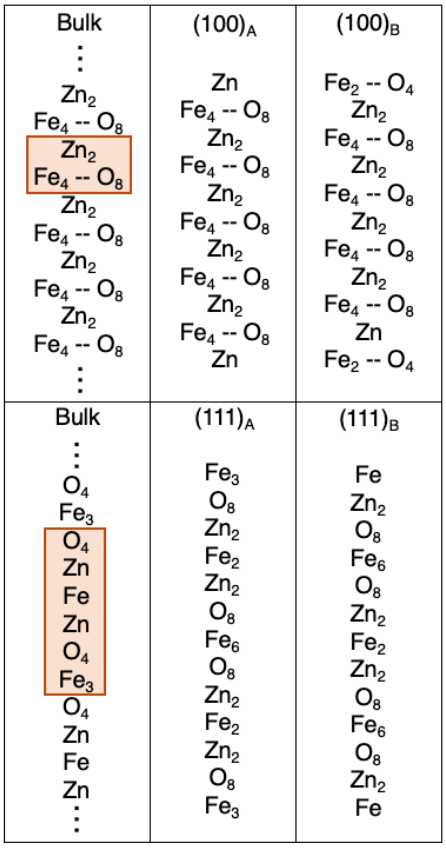

Bulk	$(100)_A$	$(100)_B$
⋮ Zn_2 Fe_4 -- O_8 Zn_2 Fe_4 -- O_8 Zn_2 Fe_4 -- O_8 Zn_2 Fe_4 -- O_8 Zn_2 Fe_4 -- O_8 ⋮	Zn Fe_4 -- O_8 Zn_2 Fe_4 -- O_8 Zn_2 Fe_4 -- O_8 Zn_2 Fe_4 -- O_8 Zn_2 Fe_4 -- O_8 Zn	Fe_2 -- O_4 Zn_2 Fe_4 -- O_8 Zn_2 Fe_4 -- O_8 Zn_2 Fe_4 -- O_8 Zn_2 Fe_4 -- O_8 Zn Fe_2 -- O_4
Bulk	$(111)_A$	$(111)_B$
⋮ O_4 Fe_3 O_4 Zn Fe Zn O_4 Fe_3 O_4 Zn Fe Zn ⋮	Fe_3 O_8 Zn_2 Fe_2 Zn_2 O_8 Fe_6 O_8 Zn_2 Fe_2 Zn_2 O_8 Fe_3	Fe Zn_2 O_8 Fe_6 O_8 Zn_2 Fe_2 Zn_2 O_8 Fe_6 O_8 Zn_2 Fe

Figure 4.2. Schematic representation of the $ZnFe_2O_4$ (100) and (111) A and B terminated surface reconstructions. The column of the left shows the sequence of layers in the bulk for the given direction; the shaded rectangles in the bulk scheme highlight a stoichiometric unit.

Building the (111) surfaces presented a greater challenge, as the unit cell needed to be expanded in both lateral directions, which leads to the two different types of bulk Fe layers having six and one Fe atoms per cell, respectively. The $(111)_A$ surface ends at the Fe_6 layer, but half of the surface atoms are removed (Fe_3

termination). The $(111)_B$ surface ends at the Fe_2 layer, and again half of the Fe atoms are removed to maintain the stoichiometry (Fe termination). **Figure 4.3** shows the constructed surface structures. An inversion on the surface was modelled by switching one Fe atom in an Oh site with one Zn atom in a Td site on either side of the slabs to maintain the stoichiometry and symmetry. For the most stable surface termination further inversions were created propagating into the surface.

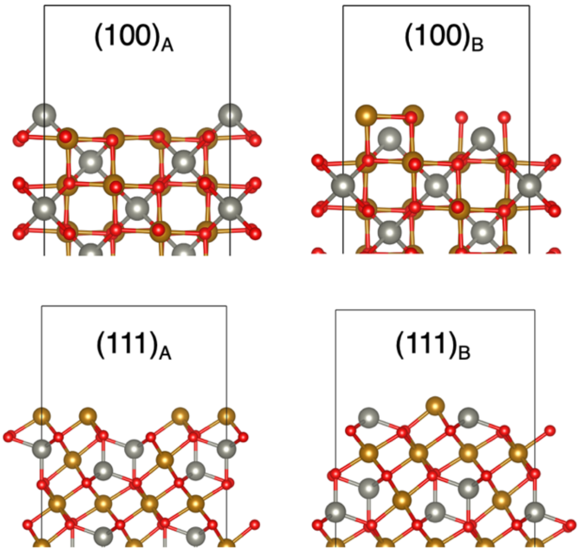

Figure 4.3. Surface structures of $ZnFe_2O_4$ (100) and (111) A and B surface reconstructions leading to stoichiometric and non-polar terminations. Only one side of the slab is shown but the other side of the slab is equivalent by symmetry. Colour scheme: Zn = silver; Fe = gold; oxygen = red.

Surface energies (γ) for the different surface terminations were obtained from the equation:

$$\gamma = \frac{E_{\text{slab}} - E_{\text{bulk}}}{2A}, \tag{15}$$

where E_{slab} is the total energy of the relaxed slab, E_{bulk} is the energy of the bulk with the same number of formula units as the respective slab and A is the surface area of one side of the slab. In the calculation both sides of the symmetric slab are allowed to relax and therefore both must be considered in the surface energy calculation.

4.2.2 Semi-empirical simulations of core-level spectra

The semi-empirical quantum many-body program QUANTY,[239, 256, 257] within the graphical user interface CTM4XAS,[237] was used to simulate the Fe $L_{2,3}$ edges. This semi-empirical approach considers Coulomb interaction, spin-orbit coupling and crystal-field splitting around a given species, without consideration of the crystalline structure. Independent calculations were completed for the three Fe species observed in the spinels: Fe^{3+} in Oh and Td symmetry and Fe^{2+} in Oh symmetry. Based on experience in modelling similar systems, the Coulomb interaction was scaled to 94% and 88% of the Hartree-Fock values of the Slater integrals, whereas the spin-orbit coupling parameter were kept at 1.0 (no screening) for both core and valence levels.[237] A broadening of 0.1 eV was used for Gaussian functions and broadenings of 0.2 – 0.4 eV were used for Lorentzian functions in both the Near-edge X-ray Absorption Fine Structure (NEXAFS) and X-Ray Magnetic Circular Dichroism (XMCD) simulations. The crystal-field parameters for each Fe species have been outlined in **Table 4.1**. The integrated Fe^{2+} and Fe^{3+} NEXAFS and XMCD spectra were normalised to the corresponding numbers of d electrons (6 and 5, respectively). The energies of the simulated spectral shapes were aligned by fitting to the experimental XMCD signals.

Table 4.1. Crystal-field parameters of independent Fe species for the CTM4XAS input.

Fe Species	10 Dq / eV	Exchange Field / meV	
		XAS	XMCD
Fe^{3+} (Td)	-0.5	0	-90
Fe^{3+} (Oh)	1.6	0	90
Fe^{2+} (Oh)	1.2	0	90

4.2.3 X-Ray diffraction

Powder X-ray diffraction (PXRD) patterns of $CuFe_2O_4$ and $ZnFe_2O_4$ samples were collected on a Rigaku SmartLab diffractometer at the ISIS Material Characterisation Laboratory, using Cu $K\alpha_1$ radiation, in reflection mode and at room temperature, over a 2θ range of 10 – 80°.

In the case of $CoFe_2O_4$, the PXRD technique is limited because Co and Fe have similar atomic numbers (27 and 26, respectively), leading to similar scattering factors, and making it difficult to distinguish between these cations when they share a given spinel site. Therefore, for this sample, an Anomalous X-ray Scattering (AXRS) experiment was carried out on the multipurpose six-circle geometry diffractometer of SpLine BM25 Beamline at the European Synchrotron Radiation Facility at room temperature. The sample was loaded in a 0.5 mm diameter borosilicate capillary, and the recorded diffraction patterns were collected for $CoFe_2O_4$: one using a beam energy of 20000 eV (6 – 60° 2θ range), and another one using an energy of 7097 eV (15 – 67° 2θ range), that is 15 eV below the Fe K-edge absorption edge at 7112 eV.

The Rietveld method was used for fitting the powder diffraction patterns and crystal structure refinements, by means of the Topas Academic v6 software.[258] The structural starting model used for the refinements was the normal spinel structure and, for the case of AXRS data, the diffraction patterns at both incident energies were fitted simultaneously using the same structural parameters for $CoFe_2O_4$. In all cases, the A and B cation occupancy at both Td and Oh crystallographic positions were refined, applying the constraint that both sites should be fully occupied, and that the final calculated formula should be AB_2O_4.

Instrument peak profile parameters, which were calculated from a silicon NIST-640C standard reference sample measured under the same conditions as the three different samples, were used to calculate broadening effects, due to crystalline size, and perform particle-size analysis.

4.2.4 Catalytic testing

The catalytic testing was undertaken at the Catalysis Hub based at the Research Complex at Harwell. The photocatalytic oxygen evolution was measured at room temperature in a gas-tight 50 mL quartz photoreactor. The light intensity was adjusted to 1 sun (100 mW cm^{-2}) using an AM 1.5G mass filtered 300 W Xe source. 25 mg of sample was used for each spinel (MFe_2O_4, M = Co, Cu, Zn) measurement in a 0.5 M $AgNO_3$ medium to act as the hole scavenger. Before the measurements, the system was purged for 1 hour with 1.5 bar Ar gas. The gas composition was monitored by gas chromatography with a barrier ionisation discharge (BID) detector (GC, Shimadzu GC- 2010 Plus). The oxygen evolution was measured over 5 hours. Reference measurements for each medium were taken to normalise the oxygen evolution data for the spinel samples; further details of the control measurements can be seen in **Figure 4.4**.

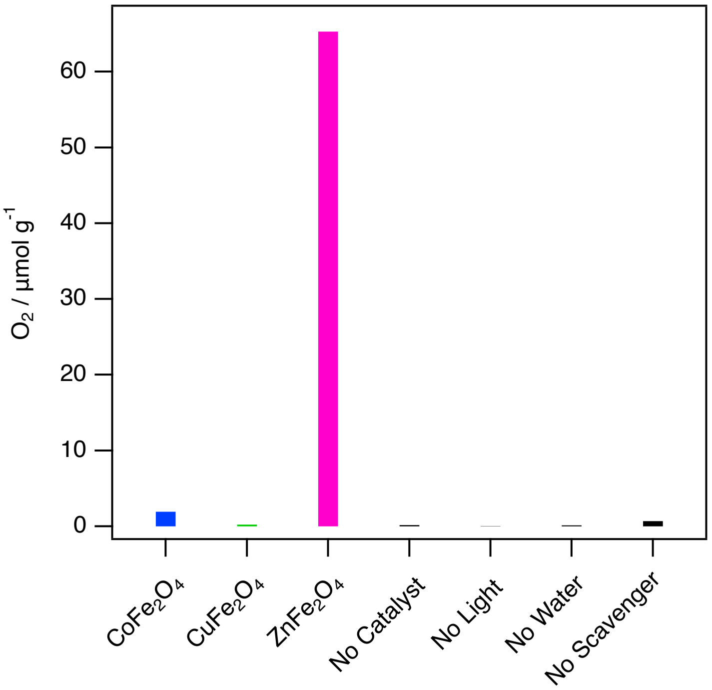

Figure 4.4. The amount of oxygen produced by the spinels MFe_2O_4 (M = Co, Cu or Zn) and the oxygen produced by the control measurements: with no catalyst, or with the presence of the $ZnFe_2O_4$ catalyst but no UV light, no water or no $AgNO_3$ sacrificial agent (scavenger).

4.2.5 Near-edge X-Ray absorption fine structure

NEXAFS measurements were carried out on branch B of the B07 (VerSoX) beamline at Diamond Light Source (DLS) using the total electron yield (TEY) mode collected under 1 mbar helium and corrected for the beamline transmission.[143, 144]

The NEXAFS spectra were normalised to the beamline transmission by dividing I_0 (the photocurrent measured off the final refocussing mirror). The background and edge jumps were subtracted with a Fermi-Dirac step function. Two step functions with a width of 1 eV were used with a 2:1 jump ratio for the L_3 and L_2 edges, respectively. The edge jump position was shifted by 3 eV with respect to the peak maximum.[259] Finally, the integral of each spectrum was normalised with respect to the average number of holes, 4.8 (20% Fe^{2+} and 80% Fe^{3+} as determined by the XMCD fitting).

4.2.6 X-ray magnetic circular dichroism

XMCD measurements were carried out on the I10 beamline at DLS on the electromagnet end station in TEY mode. The measurements were done at normal incidence with a positive helicity at room temperature. Varied external magnetic fields of ±1.5 - ±1.9 T were applied to the spinels.[78]

The positive and negative circularly polarised XAS spectra measured were first normalised with respect to the beamline transmission and then normalised to the pre-edge region. The difference in these normalised spectra was taken to obtain the XMCD signals.

4.3 Results

4.3.1 Bulk structure: DFT simulations and X-Ray diffraction

We first discuss the thermodynamics of cation distribution in the three ternary oxides $CoFe_2O_4$, $CuFe_2O_4$, and $ZnFe_2O_4$. To approximate the free energy of inversion as a function of inversion degree and temperature, we interpolate the inversion energies obtained from the three DFT calculations at x = 0, 0.5 and 1 using a quadratic dependence, which was originally proposed by O'Neill and Navrotsky [16] and has subsequently been used in several investigations of the thermodynamics of inversion in spinels.[260-262] The interpolated inversion energy functions, ΔE_{conf}, are shown in **Figure 4.5a**. They only depend on the configuration and are therefore independent of the temperature.

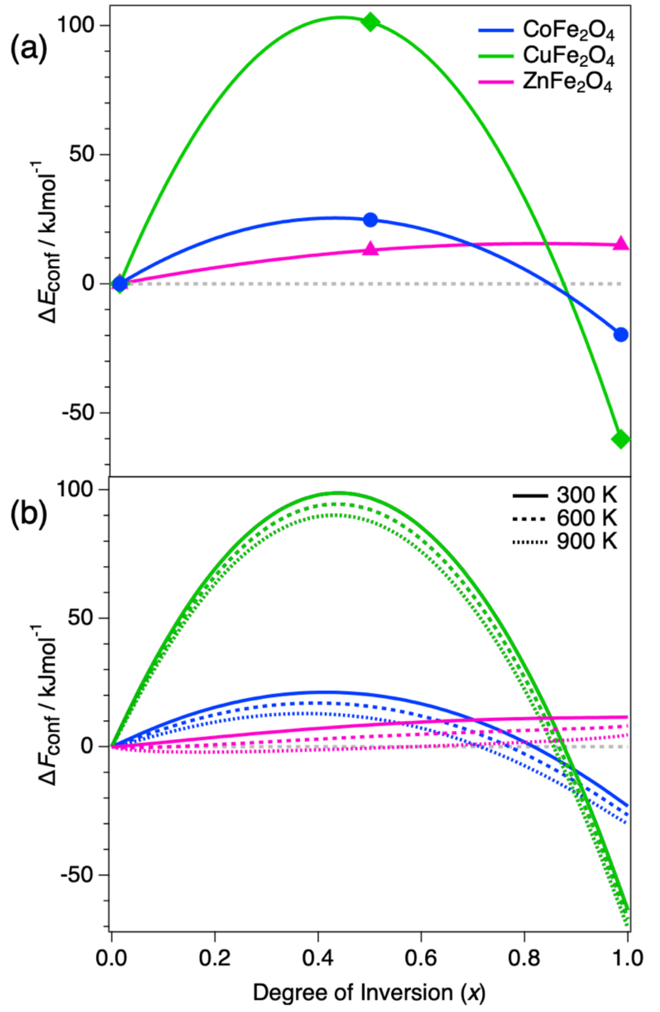

Figure 4.5. a) Inversion energies per formula unit (ΔE_{conf}, configurational contributions only) obtained by DFT, and b) configurational free energies (ΔF_{conf}) at 300 K (solid line), 600 K (dotted line) and 900 K (dashed line) of $CoFe_2O_4$ (blue circles), $CuFe_2O_4$ (green diamonds) and $ZnFe_2O_4$ (pink triangles).

From the calculated inversion energies, the configurational free energy of inversion, ΔF_{conf}, can be estimated as:

$$\Delta F_{\mathrm{conf}} = \Delta E_{\mathrm{conf}} - T\Delta S_{\mathrm{conf}} \tag{16}$$

where ΔS_{conf} is the ideal configurational entropy of inversion:[29, 263]

$$\Delta S_{\mathrm{conf}} = -R\left[x\ln x + (1-x)\ln(1-x) + x\ln\frac{x}{2} + (2-x)\ln\left(1-\frac{x}{2}\right)\right]. \tag{17}$$

There might be other (excess) contributions to the inversion entropy, arising from energy differences between configurations at a given inversion degree, or from vibrational contributions. However, previous work showed that these contributions are relatively small and can be ignored in a first approximation.[261]

The dominant effect is the inversion energy, whereas the entropic term plays a relatively small role. Both $CoFe_2O_4$ and $CuFe_2O_4$ reach the minimum inversion energy at $x = 1$, implying a preference to be fully inverse. In contrast, the inversion energy of $ZnFe_2O_4$ is positive across the full range of x, with the most stable configuration being normal ($x = 0$). These results can be rationalised based on simple physical arguments. In $A^{2+}B^{3+}{}_2O^{2-}{}_4$ spinels, the lattice (Madelung) energy and electrostatic stabilisation favour the normal cation distribution. Thus, in the absence of crystal-field stabilisation energy (CFSE) effects and the tendency for Zn^{2+} to form sp^3 hybridisation in the Td sites, the normal distribution is preferred. In both $CoFe_2O_4$ and $CuFe_2O_4$ the divalent cation is a transition metal with higher CFSE in the octahedral than in the tetrahedral site (excess octahedral stabilisation energy is 30.9 kJ mol^{-1} for Co^{2+} and 63.5 kJ mol^{-1} for Cu^{2+} [75]); therefore, these spinels favour the inverse distribution.

The inclusion of configurational entropy effects permits the consideration of finite temperatures within this simple model, but it does not change the picture considerably. The free energy of inversion variation with x at different temperatures is shown in **Figure 4.5b**. In the cases of $CoFe_2O_4$ and $CuFe_2O_4$, the free energy of inversion minima occurs at $x = 1$ even at high temperatures up to 900 K. On the other hand, the inversion free energy minima of $ZnFe_2O_4$ are close to the normal end, ranging from $x = 0$ at room temperature up to $x = 0.2$ at 900 K.

Next the theoretical bulk values of the inversion degree are compared with the observed values for small nanoparticles. The nanoparticle size, inversion degree (x), cell parameter (a) and the oxygen coordinate parameter (u) of the spinel samples, as determined by AXRS or PXRD with the Rietveld method, are listed in **Table 4.2**. The corresponding AXRS and PXRD patterns can be seen **Figure 4.6** and **Figure 4.7**, respectively. The R_{wp} (weighted profile R-factor) defines the weight ratio of the difference between the observe red and calculated diffraction patterns, generally an ideal R_{wp} value is considered to be < 10%.[264-266] The particle sizes of the cobalt, copper and zinc ferrites are 35, 24, and 22 nm, respectively. $CoFe_2O_4$ and $CuFe_2O_4$ display high inversion degrees (x) of 0.81 and 0.91, respectively, which are slightly below the DFT-predicted value of 1 (fully inverse) for both systems. In contrast, the degree of inversion of $ZnFe_2O_4$ (0.26), although much lower compared to the cobalt and copper ferrites, is more inverse than the DFT predicted normal structure. The inversion energy curve, however, shows a very small x-dependence, therefore small additional entropy contribution can alter the position of the minimum significantly. Overall, the general trends of x agree with that of DFT predictions and with previous literature reports.[10, 106, 118]

Table 4.2. Summary of experimentally determined (AXRS data for $CoFe_2O_4$ and PXRD data for $CuFe_2O_4$ and $ZnFe_2O_4$) and DFT-calculated structural parameters x (inversion degree), a (cell parameter), u, and R_{wp} (weighted profile R-factor). The u parameter determines the O atoms coordinates (u, u, u) in the standard setting of the Fd-$3m$ space group.

	Experimental (nanoparticles at room temperature)					DFT (bulk at 0 K)		
Sample	Size / nm	x	a / Å	u	R_{wp} / %	x	a / Å	u
$CoFe_2O_4$	35(1)	0.81(1)	8.398(3)	0.246(3)	4.11	1	8.423	0.245
$CuFe_2O_4$	24(1)	0.91(2)	8.371(7)	0.249(4)	1.17	1	8.409	0.242
$ZnFe_2O_4$	22(1)	0.26(1)	8.439(3)	0.243(3)	1.50	0	8.481	0.239

The absolute values of the cell and oxygen parameters of the nanoparticle samples are generally close to those calculated by DFT, with the largest percentage differences between the experimental and calculated a and u (2% and 3%, respectively) being observed in the case of $CuFe_2O_4$. The trend in a values observed in the experimental data (Cu < Co < Zn) is also seen in the simulation results. Factors effecting the accuracy of the simulation prediction include the approximations made in the density functional (the generalised gradient approximation), the absence of nanostructuring effects (calculations are done for the infinite bulk crystal), and the temperature difference (0 K in DFT, room temperature for experiment). From the experimental point of view, X-rays have low sensitivity to oxygen atoms; moreover, their scattering signal is masked by the surrounding heaver atoms making the refined u value less reliable. Also, a direct comparison between the parameters is difficult as the simulated spinels have extreme inversion degrees (*i.e.* x = 0 or 1), from which the nanoparticles deviate.

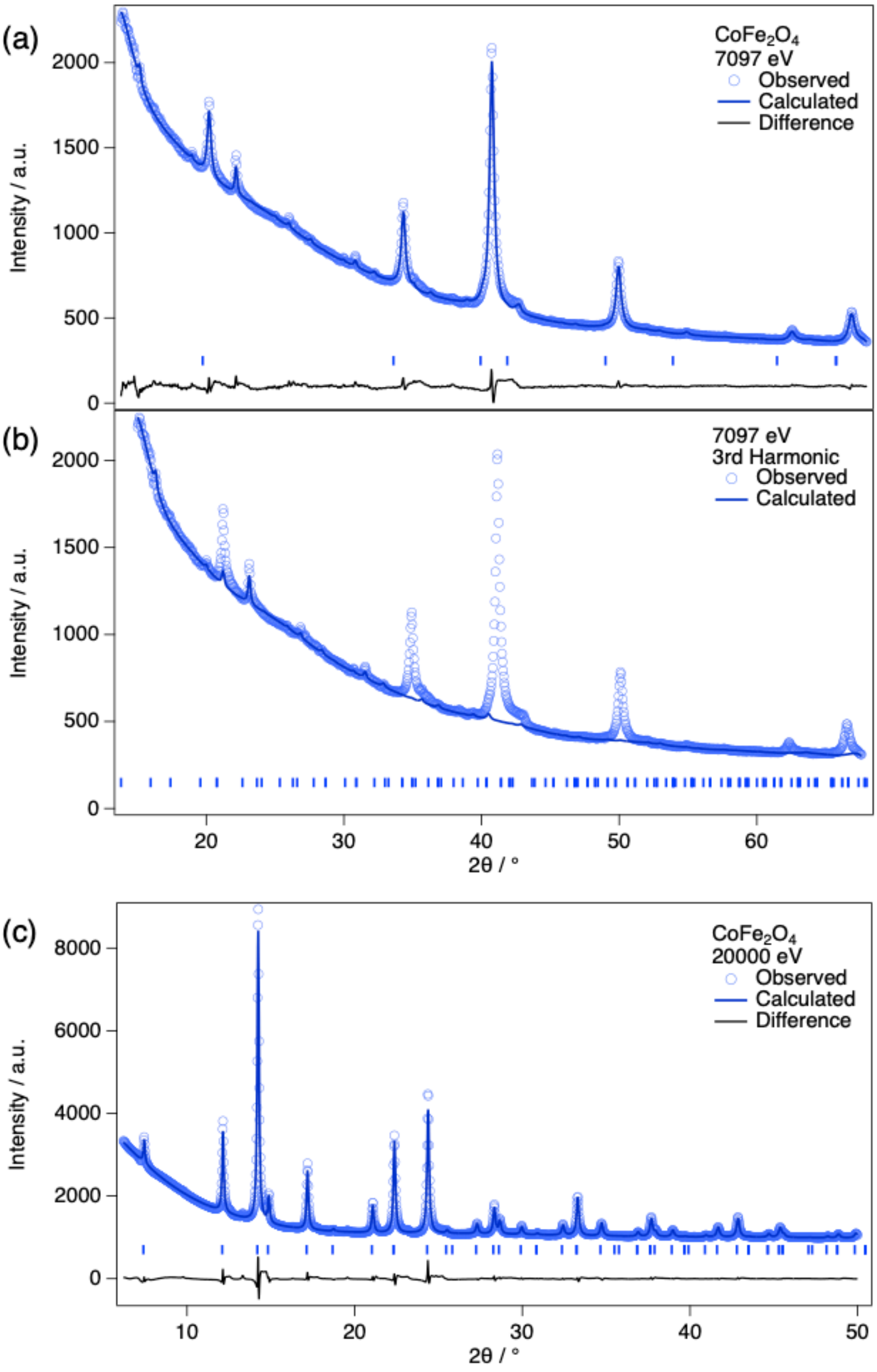

Figure 4.6. The AXRS patterns of CoFe$_2$O$_4$ at (a) 7097 eV, (b) 7097 eV only considering the 3rd harmonic contributions, and (c) 20,000 eV.

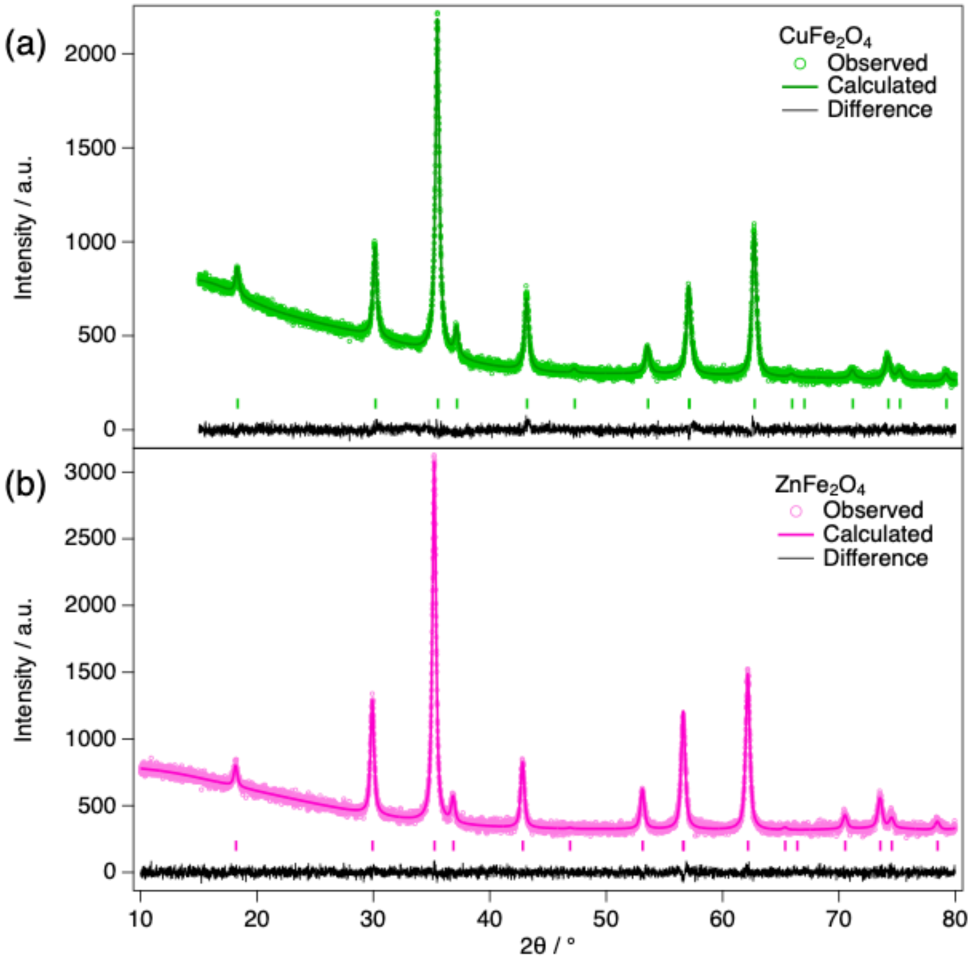

Figure 4.7. The PXRD pattern of (a) $CuFe_2O_4$ and (b) $ZnFe_2O_4$.

4.3.2 Electronic Structure, Band Alignment, and Photocatalysis

The photocatalytic OER using Ag^+ ions as an electron sacrificial agent on all the samples was carried out under simulated solar light (1 sun). As seen in **Figure 4.8**, $CoFe_2O_4$ and $CuFe_2O_4$ exhibit very little photocatalytic oxygen evolution across 5 hours of irradiation (< 3 μmol g^{-1} of O_2). In contrast, $ZnFe_2O_4$ produced approximately 65 μmol g^{-1} of O_2 after 5 hours.

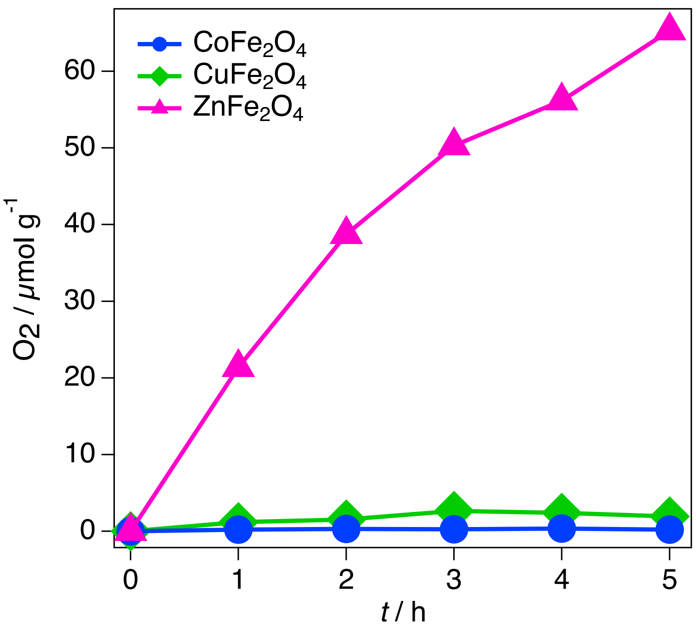

Figure 4.8. Photocatalytic oxygen evolution of MFe_2O_4 (M = Co, Cu or Zn) over a time of 5 hours under simulated sun light using $AgNO_3$ as an electron sacrificial agent.

We now attempt to rationalise the photocatalytic behaviour of the samples in terms of the electronic structures and band alignments. The density of states (DOS), including the partial DOS contributions from the ions, of the spinels can be seen in **Figure 4.9**. In each case, the Fe 3d levels are the main contribution to the conduction band (CB). On the other hand, the character of the valence band (VB) differs among the spinels: the high-lying filled Co 3d levels make the main contribution to the VB of $CoFe_2O_4$, leading to the narrowest gap in the series; whereas the absence of d level contributions to the VB of $ZnFe_2O_4$ leads to the widest gap among the three spinels. The calculated band gaps of $CoFe_2O_4$, $CuFe_2O_4$ and $ZnFe_2O_4$ are 1.96, 2.17 and 2.84 eV, respectively, which are similar to those observed in respective nanoparticle samples in the literature.[267, 268] These band-gap values are all sufficient in principle for photocatalysis of the overall water splitting reaction, for which a minimum thermodynamic potential of 1.23 eV is required.[42, 43]

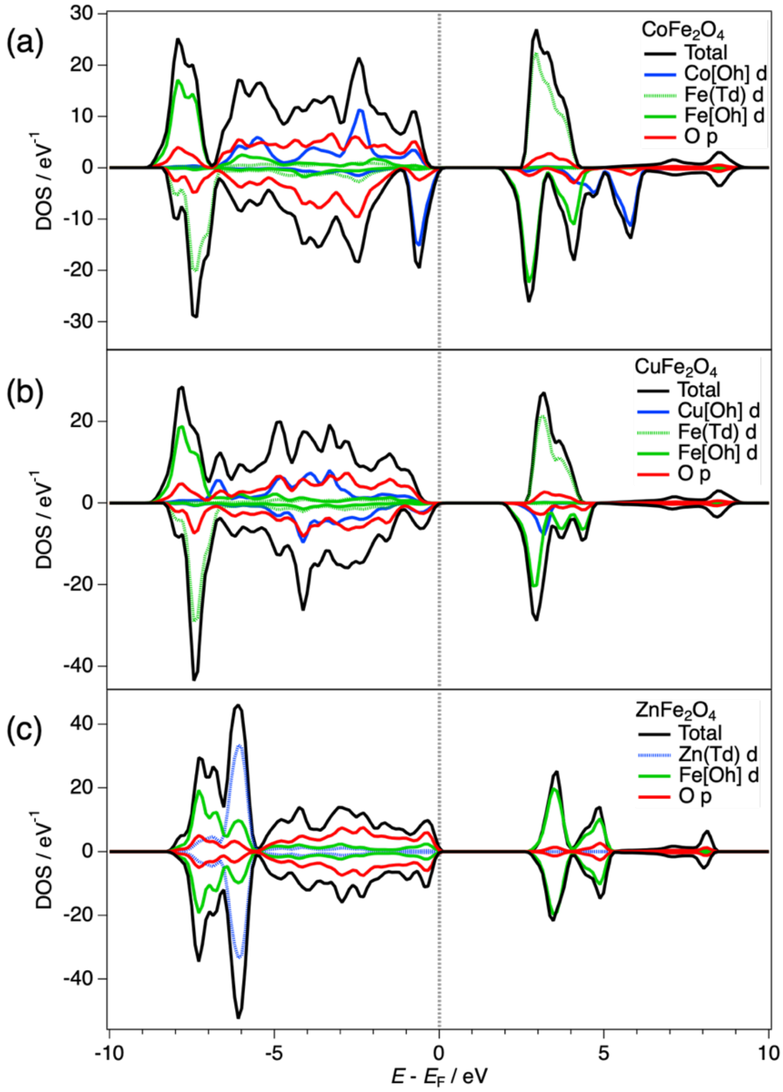

Figure 4.9. Density of states (DOS) at HSE06 level for a) $CoFe_2O_4$, b) $CuFe_2O_4$ and c) $ZnFe_2O_4$ and partial DOS contributions from Co, Cu, Zn and Fe d orbitals and O p orbitals.

In addition to having a suitable band gap, a semiconductor must also have CB and VB positions straddling the HER and OER levels in order to be a good water splitting photocatalyst (in a single-semiconductor configuration).[43] From the bulk simulations, the CB minimum and VB maximum are calculated with respect to the average electron potential in the solid. To compare these potentials with respect to the HER and OER potentials the electronic structure needs to be aligned relative to the vacuum level. To do so, a slab calculation can be used to determine the potential difference (ΔV) between the pseudo-bulk average and the vacuum potential. **Figure 4.10** shows a stoichiometric slab, with a symmetric $(100)_A$ terminated surface and vacuum level.

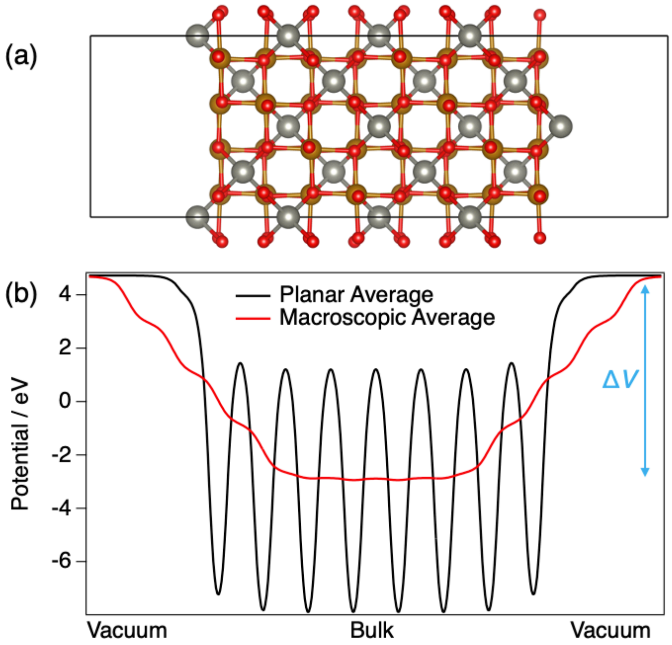

Figure 4.10. (a) $ZnFe_2O_4$ slab with a $(100)_A$ termination and (b) the planar-averages of the electrostatic potential.

The calculated band alignment of the spinels with respect to vacuum scale are shown in **Figure 4.11,** compared with potentials of the water splitting half-reactions. The potentials of the HER and OER in the vacuum scale at pH = 0 are -4.44 and -5.67 eV, respectively. These energy levels are shifted up with a pH > 0 at temperature T by $k_BT \times \text{pH} \times \ln 10$.[248, 269] Therefore, at room temperature and pH = 7 the HER and OER potentials are -4.03 and -5.25 eV, respectively, corresponding to those seen in **Figure 4.11**. Despite all three spinels having a suitable band gap to catalyse the overall water splitting process, their band alignments do not fit the thermodynamic requirements, due their high-lying CB minima with respect to the HER potential (-4.03 eV). The lack of oxygen evolution displayed by $CoFe_2O_4$ and $CuFe_2O_4$ (**Figure 4.8**) could be explained by the VB maxima positions, which lie above the OER potential (-5.25 eV). In contrast, the band alignment of $ZnFe_2O_4$ meets the thermodynamic requirements for the OER, with a VB potential -5.90 eV.

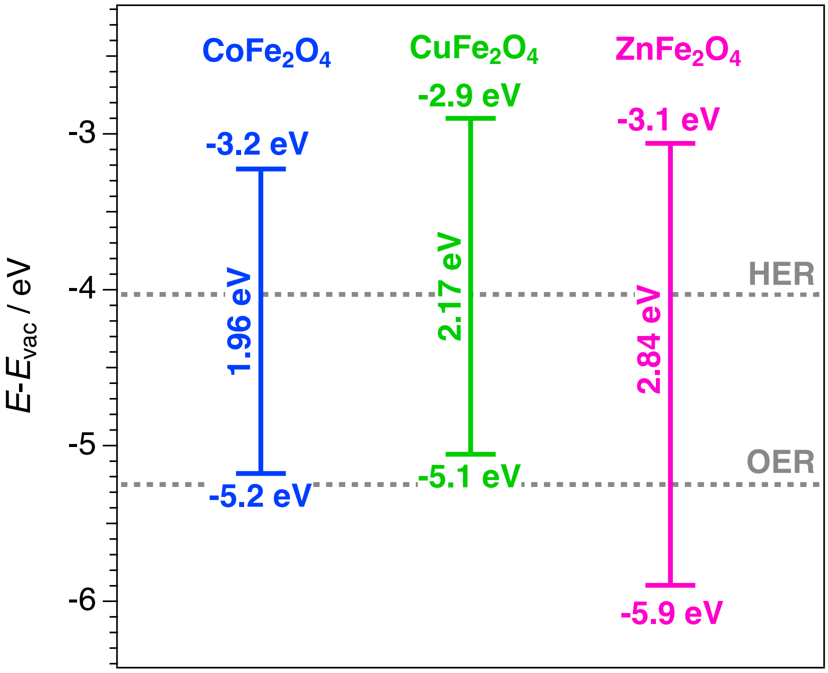

Figure 4.11. Calculated CB and VB positions and band gaps of MFe_2O_4 (M = Co, Cu or Zn). Half-reaction potentials for water splitting are represented by dotted lines.

4.3.3 Surface Effects: NEXAFS and XMCD experiments and slab calculations

While the prior discussion is focused on bulk properties, the behaviour at the oxide surfaces, where the actual catalytic reactions take place, might depart considerably from the bulk behaviour. Understanding the surface properties of these complex oxides is challenging, but some insights can be obtained by using surface-sensitive techniques, such as total electron yield (TEY) NEXAFS and XMCD. These techniques probe approximately 2 nm into the sample surface. The Fe $L_{2,3}$ edges measured in TEY mode by NEXAFS of $CoFe_2O_4$, $CuFe_2O_4$, and $ZnFe_2O_4$ are shown in **Figure 4.12a**. The spectral features are dependent on the relative quantities of each iron species, as calculated in **Figure 4.12b**. The intensity of the feature between the pre- and main edges at 708 eV (indicated by the red arrow in **Figure 4.12a**) can be related to the presence or absence of tetrahedrally coordinated Fe^{3+}. The width of the main edge at 709 eV is also affected by the cation distribution. In $ZnFe_2O_4$, the intensity of this feature is lower compared to $CoFe_2O_4$ and $CuFe_2O_4$, indicating that there is less Fe^{3+}_{Td} (*i.e.* less inversion) in the zinc ferrite surface compared to the surface of the other two spinels. Therefore, the same trend in cation distribution is observed in both the surface and bulk of these materials. However, quantitively determining the relative amounts of the different Fe species is difficult to do by just fitting NEXAFS spectra; more spectral features or information is required, which can be obtained from XMCD.

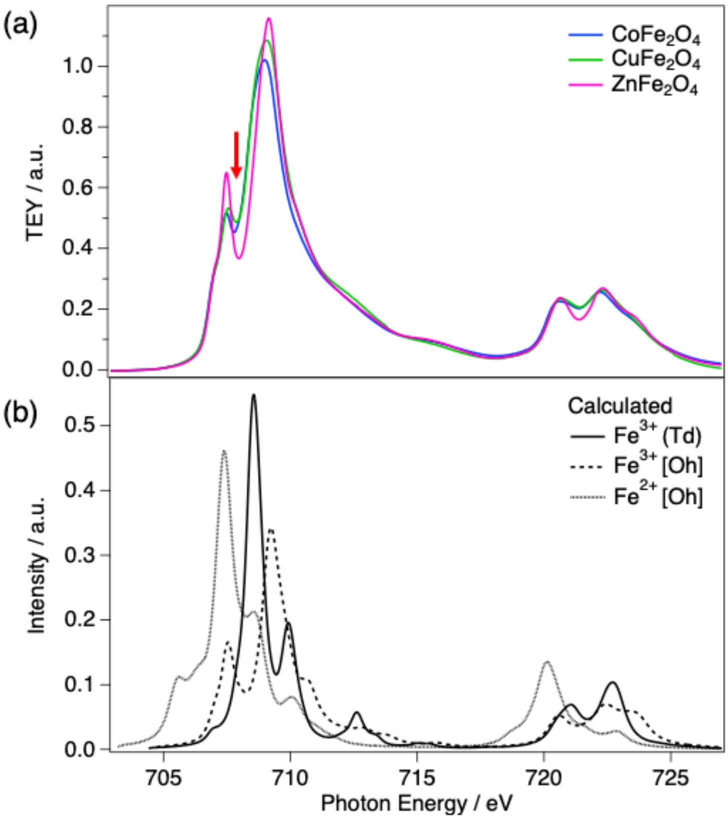

Figure 4.12. a) Fe $L_{2,3}$ edge NEXAFS spectra of MFe_2O_4 (M = Co, Cu or Zn) and b) calculated spectra of Fe^{3+} (Td), Fe^{3+} (Oh) and Fe^{2+} (Oh) by CTM4XAS. The red arrow in a) highlights the spectral feature that is significantly impacted by the relative amounts of the Fe species.

The Fe L_3 edges measured by XMCD seen in **Figure 4.13a-c** (also collected in TEY mode, and therefore surface-sensitive) display spectral features that are more distinguishable between the different Fe species compared to NEXAFS. The features at 707.5 eV, 708.7 eV and 709.4 eV can be attributed mainly to contributions from Fe^{2+} (Oh), Fe^{3+} (Td) and Fe^{3+} (Oh), respectively, with the Oh and Td ions displaying opposite dichroism. The difference of around 2 eV observed in our spinel XMCD spectra between the Fe^{2+} and Fe^{3+} peak maxima in Oh coordination is smaller than that reported for magnetite (Fe_3O_4), a fully inverse spinel (2.5 eV).[270] However, the relative shifts between the iron species peak maxima observed in **Figure 4.13a-c** are comparable with XMCD shifts of spinel ferrites reported in the literature.[271, 272] The relative quantities of the Fe species at the surface can be estimated by fitting a combination of the calculated species-specific spectra (**Figure 4.13d**) to the experimental spectra. Since the XMCD measurements were also collected in TEY mode, the Fe distribution at the near-surface can be quantified.

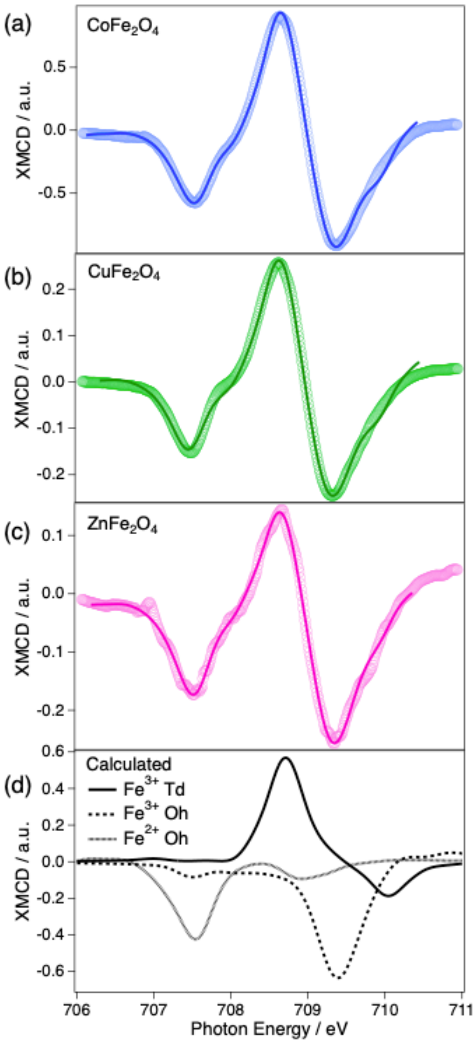

Figure 4.13. Fe L_3 edge XMCD spectra of a) $CoFe_2O_4$, b) $CuFe_2O_4$, and c) $ZnFe_2O_4$ in which the circles are the experimental data and the solid line are the calculated spectra. d) The calculated Fe L_3 edge of Fe^{3+} (Td), Fe^{3+} (Oh) and Fe^{2+} (Oh) by CTM4XAS.

The percentages of Fe^{2+}/Fe^{3+} in Oh/Td sites, as derived from the XMCD fit, are listed in the **Table 4.3**. The fit of the $CoFe_2O_4$ signal showed 76% percent of near-surface Td sites are occupied by Fe cations, in contrast to 81% of Fe occupied Td sites in the bulk. A similar difference was observed in $CuFe_2O_4$ with 74% of the near-surface Td sites being occupied by Fe cations, compared to 91% in the bulk. $ZnFe_2O_4$ showed a significant contrast from 26% of Td occupied by Fe in the bulk to 52% at the surface. The XMCD signals also indicate that around 20 – 30% of the octahedrally coordinated iron was Fe^{2+} in all three of the samples, indicating some level of surface reduction which could be explained by the formation of oxygen vacancies or other surface defects.

Table 4.3. Percentages of Fe cations in different oxidation states (Fe^{2+}/Fe^{3+}) and sites (Oh/Td) at the near-surfaces of spinels MFe_2O_4 (M = Co, Cu or Zn), as derived from the XMCD fitting.

Sample	Fe^{3+} Oh	Fe^{3+} Td	Fe^{2+} Oh
$CoFe_2O_4$	42.9%	38.1%	19.0%
$CuFe_2O_4$	44.5%	37.2%	18.3%
$ZnFe_2O_4$	46.8%	25.1%	28.1%

To illustrate how the presence of the surface can alter the preferred cation distribution observed in the bulk, we conducted DFT simulations in $ZnFe_2O_4$ slabs with different surface terminations and cation distributions (swapping Zn and Fe cations at the top layer). Only $ZnFe_2O_4$ was considered for the surface calculations, since for this composition nanoparticles have a significant difference in the inversion degree observed in the surface compared to the bulk. Also, unlike $CoFe_2O_4$ and $CuFe_2O_4$, zinc ferrite was the only sample that demonstrated any catalytic activity for the OER.

The relaxation of the different terminations can be seen in **Figure 4.14**. In the $(100)_A$ and $(111)_A$ terminated surfaces, the surface cations shift towards the bulk by up to 1.2 Å, which generates minor distortion or shifting towards surface within their sub-surface layers. The $(100)_B$ sub-surface layers shift towards bulk, however the top cations remain relatively fixed in the square structure. Minimal cation shifting occurs in the surface and sub-surface layers in $(111)_B$ structures during relaxation.

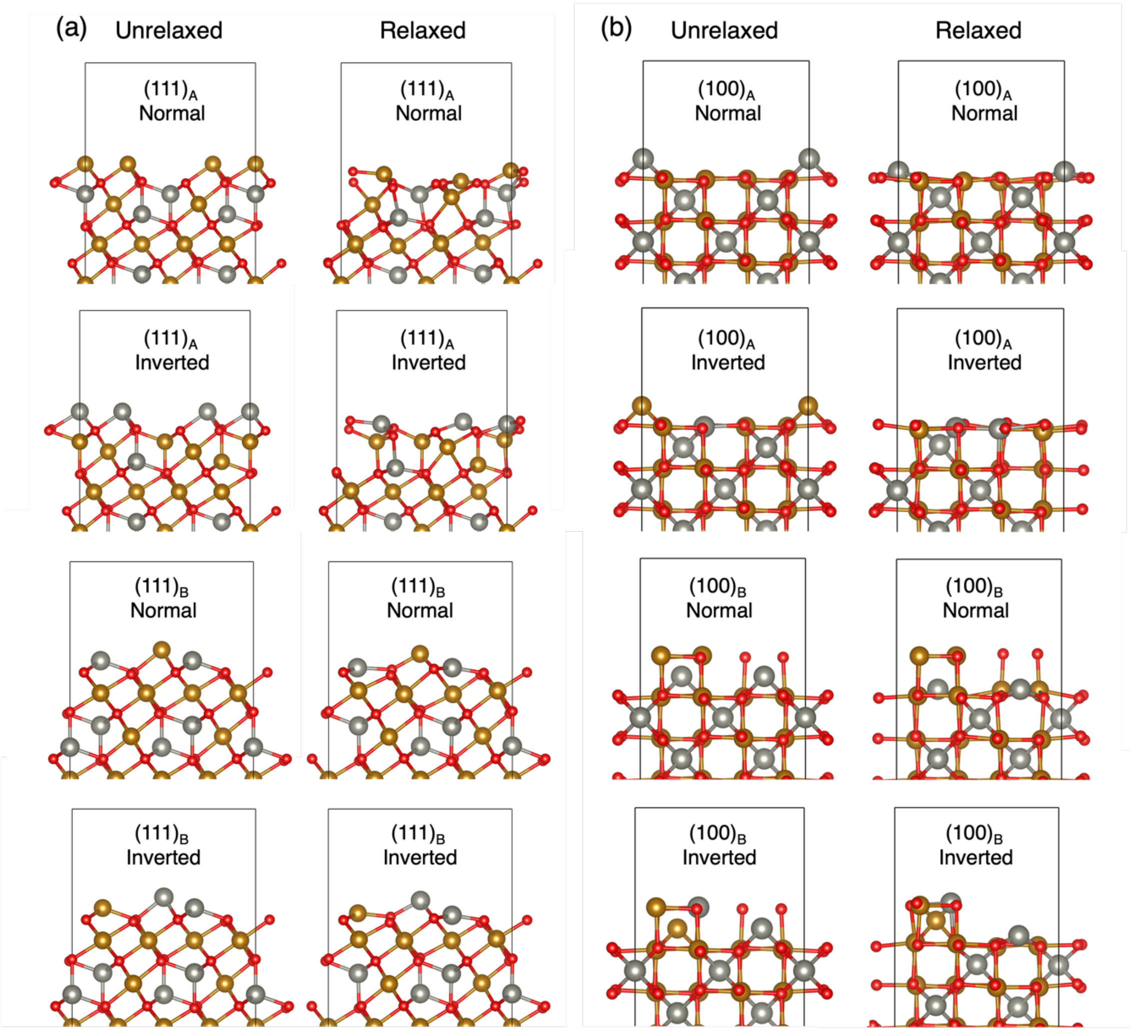

Figure 4.14. (a) $ZnFe_2O_4$ (111) A and B and (b) $ZnFe_2O_4$ (100) A and B terminated surfaces terminated surfaces before and after relaxation.

The calculated surface energies are summarised in **Table 4.4**. The most stable normal surface is the Zn-terminated $(100)_A$ surface, whereas the Fe/O-terminated $(100)_B$ surface is much less stable. This result aligns with a previous ab-initio study that found that the (100) surface of zinc ferrite is always more stable when Zn-terminated, regardless of the presence of O-rich or O-poor conditions.[254] We also find that the normal (111) surface is less stable than the $(100)_A$ termination. This contrasts with the conclusion from a theoretical study by Guo *et al*.[253] that found that the (111) surface is the most stable under the range of chemical potentials at which bulk $ZnFe_2O_4$ is stable. Since we do not perform an analysis here as a function of chemical potentials, it is difficult to compare with the results of Ref. [253]. However, for the purpose of this work, we are less interested in the relative stabilities of the surfaces, and more focused on the effect of changes in the cation distribution at the surface with respect to that of the bulk.

Table 4.4. Calculated surface energies (γ) of the relaxed terminations of the (100) and (111) A and B terminated surfaces of $ZnFe_2O_4$.

Surface	Termination	Cation Distribution at Surface	γ / Jm^{-2}
(100)	A	Normal	1.28
		Inverted	1.26
	B	Normal	2.91
		Inverted	1.91
(111)	A	Normal	2.32
		Inverted	1.62
	B	Normal	1.75
		Inverted	1.61

The comparison of the normal vs. inverted distribution of cations shows that in all cases the surface becomes more stable after the cation inversion is introduced at the surface. The $(100)_A$ surface has the smallest difference in surface energy between the normal and inverted surface (0.02 Jm^{-2}). In contrast, the $(100)_B$ termination was the least stable normal surface, but showed the most stabilisation with the inversion. The $(111)_B$ termination is more stable than the $(111)_A$ termination with no inversion; however, when inverted there is only a 0.01 Jm^{-2} difference in surface energy between the A and B terminations.

The stabilisation of inversion at the $ZnFe_2O_4$ surfaces illustrates how surface terminations, which imply a change in cation coordination, can alter the thermodynamic preferences observed in the bulk, which were driven by crystal-field effects. To investigate how deep this effect can propagate in the top layer, a second cation pair in the sub surface was inverted in the most stable surface termination, $(100)_A$. The relaxation of this surface can be seen in **Figure 4.15**.

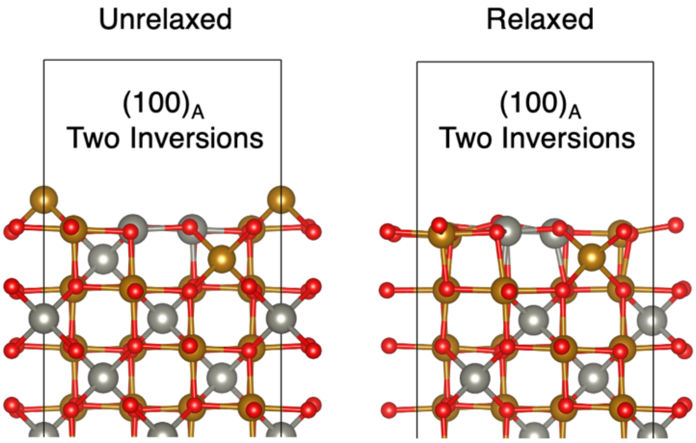

Figure 4.15. $ZnFe_2O_4$ $(100)_A$ surfaces with two cation pairs inverted before and after relaxation. Colour scheme: Zn = silver; Fe = gold; oxygen = red.

A similar shift and distortion in the surface and sub-surface layers is observed in both the $(100)_A$ surface with one and two inverted cation pairs. The calculated inversion energies (ΔE) of the normal and inverted $(100)_A$ surfaces are shown in **Table 4.5**. A negative inversion energy of -10.6 kJ mol^{-1} is observed when one inversion is created on the surface, therefore increasing the stability (as seen in the surface energies **Table 4.4**). When creating a second inversion in the sub-surface layer the inversion energy is even lower at -16.9 kJ mol^{-1}. This demonstrates that it is thermodynamically favourable for inversion to be propagated deeper into top layer of $ZnFe_2O_4$. In contrast, creating an inversion in the bulk is an unfavourable process, with a calculated inversion energy of 10.6 kJ mol^{-1}.

Table 4.5. Calculated inversion energies (ΔE) of the relaxed terminations of the $(100)_A$ $ZnFe_2O_4$ surfaces with 0, 1 and 2 inverted cation pairs.

Surface	Number of cation pair inversions on surface	ΔE / kJ mol^{-1}
$(100)_A$	0	0.0
	1	-10.6
	2	-16.9

Given the small size and high specific surface of the oxide nanoparticles, these surface effects can have a significant impact on the overall cation distributions in the nanoparticles. It is indeed reported that small nanoparticles of $ZnFe_2O_4$ tend to have higher degree of inversion compared to bulk material.[118, 273, 274] Due to the nature of the simulated surfaces, an extensive study of the surface effects, including reduction and oxygen vacancies, have not yet been investigated. However, given the important role of nanostructuring (and surfaces) in photocatalysis, these effects deserve further research attention.

4.4 Chapter Conclusions

Our comprehensive study on MFe_2O_4 (M = Co, Cu, Zn) spinel ferrites, using a combination of theoretical and experimental techniques, provides insights into their structure, electronic properties, and photocatalytic behaviours. The results from DFT simulations align well with experimental findings, revealing distinct inversion degrees and photocatalytic activities across the spinels. The DFT-predicted preference for inverse configurations in $CoFe_2O_4$ and $CuFe_2O_4$ and a normal configuration in $ZnFe_2O_4$ were confirmed by PXRD and AXRS measurements which showed inversion degrees of 0.81, 0.91, and 0.26, respectively.

Among the three spinel compositions, only $ZnFe_2O_4$ demonstrated photocatalytic activity for the OER, generating 65 μmol g^{-1} of oxygen over 5 hours under UV irradiation. This can be attributed to its favourable band alignment, as demonstrated through our electronic structure simulations. $CoFe_2O_4$ and $CuFe_2O_4$ do not exhibit OER activity, which could be explained by their band positions relative to the half-reaction potential.

Surface-sensitive measurements via XAS reveal significant variations in cation distribution at the surface compared to the bulk, particularly in $ZnFe_2O_4$ (52% of the near-surface Td sites occupied by Fe cations, compared to 26% in bulk). These findings highlight the influence of surface chemistry on the photocatalytic properties of these materials. Further, DFT simulations of surface terminations provided additional understanding of the stability and properties of the surfaces, showing that cation inversion is energetically favourable at the surfaces of $ZnFe_2O_4$, even if it is not in the bulk. Our calculations show that the effect of the surface termination in the energetics of cation inversion propagates beyond the top surface layer. The role of surface defects, such as oxygen vacancies in the stabilisation of cation inversion at the surface requires investigation in the future.

This study not only deepens the understanding of spinel ferrites and the effect of A cation substitution but also illustrates the critical role of both bulk and surface properties in determining the photocatalytic performance of these materials. Future work should continue to explore the intricate relationship between structural characteristics and catalytic activities, potentially leading to the development of more effective photocatalytic materials based on spinel ferrites.

5. Zinc depletion at the $ZnFe_2O_4$ (111) single-crystal surface: X-ray spectroscopy experiments and computer simulations

Chapter Overview

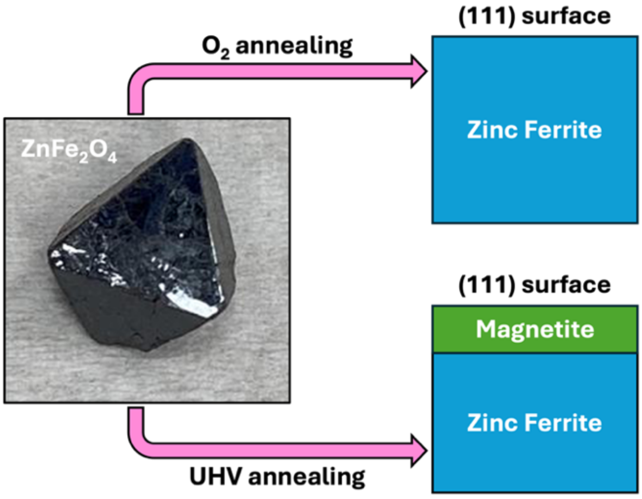

In this Chapter we use experimental and computational techniques to investigate the zinc ferrite ($ZnFe_2O_4$) (111) single-crystal surface under different preparation methods. Surface-sensitive XPS and NEXAFS measurements show that upon annealing in UHV, Zn depletion occurs, leading to the formation of an iron-rich (111) surface, whereas annealing in the presence of O_2 maintains a bulk-like $ZnFe_2O_4$ surface. After UHV annealing, a mixed Fe^{2+}/Fe^{3+} state and a cation distribution like that of magnetite (Fe_3O_4) is observed, whereas after annealing in oxygen only Fe^{3+}, mostly in octahedral coordination, is observed (as in bulk $ZnFe_2O_4$). Temperature-dependent XPS confirms significant Zn depletion in the near-surface region above 500 °C under UHV, with almost no Zn remaining at 600 °C; under O_2 atmosphere there is no zinc depletion up to 600 °C. A theoretical model illustrates how reduction from $ZnFe_2O_4$ to Fe_3O_4 with formation of O_2 and Zn gas is thermodynamically feasible under UHV, whereas the same reaction is not favourable at higher oxygen pressures. Our findings demonstrate the impact of UHV treatment on $ZnFe_2O_4$ surfaces, and cautions that UHV environments, routinely employed for surface analysis, can themselves induce substantial modifications to the surface, thereby complicating the interpretation of measurements in the context of catalytic conditions. The work presented in this Chapter was published in *Applied Surface Science*.

Statement of contributions

The work in this Chapter was a collaboration with Prof. Bo Brummerstedt Iversen (BBI), Dr Jonas Sandemann (JS) and Dr Roger A. Bennett (RAB). The single crystal was prepared by BBI and JS. The STM measurements and data processing were conducted by RAB.

5.1 Introduction

In this thesis so far, the advantages of zinc ferrite, $ZnFe_2O_4$, as a useful photocatalyst for the water splitting reaction have been highlighted. The research presented in Chapter 4 also demonstrated the significant difference between the bulk ($x = 0.26$) and surface ($x = 0.52$) cation distribution in $ZnFe_2O_4$ nanoparticles (22 nm). Also, at the near surface, ~30% of the iron cations were reduced to a 2+ oxidation state. Although the bulk generally determines the electronic properties of the material, a fundamental understanding of the surface behaviour is also crucial, given that heterogeneous catalysis is a surface process.

Single-crystal model catalysts are commonly prepared and studied under ultra-high vacuum (UHV) conditions; however, the preparation conditions of these surfaces can have a strong effect on their composition and structure, particularly in zinc-oxide materials. The known volatility of metallic Zn,[275-277] means that the structure and chemical composition of zinc-based materials can be significantly altered by the way they are treated. Controlling Zn volatility can have a variety of applications, including surface synthesis[275, 278] and metal recycling strageties.[279, 280] Previous studies on ZnO_x [278] and $ZnZrO_x$ [281] samples observed Zn evaporation above 550 °C under reductive conditions. Redekop *et al.*[281] conducted further studies of $ZnZrO_x$ and found that Zn did not evaporate from the surface at 550 °C under an oxygen environment, suggesting a reducing environment is crucial for zinc sublimation.

In this study we investigate the volatility of zinc from the $ZnFe_2O_4(111)$ surface under UHV and mild O_2 pressures. Experimental techniques include synchrotron-based X-ray photoelectron spectroscopy (XPS), near-edge X-ray absorption fine structure (NEXAFS) spectroscopy, low-energy electron diffraction (LEED) and scanning tunnelling microscopy (STM). We have used a benchmark zinc ferrite crystal grown following the procedure described by Sandemann *et al.*[12, 282] with a well-characterised defect-free, bulk structure. The experimental analysis in this study is complemented with density functional theory (DFT) simulations.

5.2 Methods

Growth of almost defect-free single-crystals of $ZnFe_2O_4$ was achieved using the flux method with PbO as flux material.[282] PbO was used in a 4:1 weight ratio to the spinel components. 50 g of PbO (99.99% metals basis, Alfa Aesar) was mixed with equimolar amounts of Fe_2O_3 (99.99% chemPUR) and ZnO (99.99% metal basis, Alfa Aesar) in a Pt crucible, which was covered with a lid and placed in Al_2O_3 sand inside an alumina crucible. The crucible was heated in a Nabertherm L5/14 muffle furnace to 1473 K at 600 K h^{-1}, then cooled to 1423 K at 10 K h^{-1} followed by cooling to 1173 K, where the temperature was held for 24 hours before the furnace was turned off to cool naturally to room temperature. Extensive single-crystal X-ray and neutron diffraction in combination with elemental analysis confirmed that the single crystals are almost defect free with ~1% cation inversion.[12] A picture of the single-crystal, highlighting one of the (111) planes can be seen in **Figure 5.1**.

Figure 5.1. Picture of the $ZnFe_2O_4$ single-crystal that is approximately 5 mm^3 in size with the (111) plane measured highlighted.

The sample surface was prepared by two different methods. The first step of both preparation methods was to argon-sputter the sample at an energy of 1 keV. For the first preparation method the sputtered surface was annealed in UHV (10^{-10} mbar) to 600 °C. For the second preparation method the sample was also annealed to 600 °C but in 10^{-5} mbar of oxygen pressure. For both methods the sample was annealed for 10 minutes before being cooled to room temperature (RT) slowly under the respective pressure conditions. Cycles of sputtering/annealing were carried out until contaminants were below the detection limit in the XPS survey spectra. The preparation methods were conducted in ES-1 preparation chamber on the B07-B beamline or in the separate UHV chamber linked with the B07-C beamline.

XPS and NEXAFS measurements were carried out on branch B of the B07 (VerSoX) beamline at Diamond Light Source.[25] The temperature-dependent XPS measurements were taken at 25 °C increments from 300 °C to 600 °C and at room temperature post cooling, this process was repeated for both annealing conditions.

The survey spectra were normalised to the O 1s peak to allow for relative comparison of the Fe 2p and Zn 2p peaks. A Shirley background removal was completed for the Fe 2p and Zn 2p peaks measured and the spectra were normalised with respect to their relative cross sections.[161, 163] The Zn $2p_{3/2}$ and $2p_{1/2}$ peaks were shifted to binding energies of 1021.8 eV and 1044.9 eV, respectively, based on the peak positions of Zn^{2+} reported in the literature.[283-286] The Fe 2p peaks measured were then shifted in binding energy by the same magnitude as the Zn 2p measured at the same photon energy. The valence-band measurements were normalised from 0 (pre-Fermi edge) to 1 (post Zn 3d peak). The binding energy was then shifted to align the Fermi edge to 0 eV.

NEXAFS spectra were measured under UHV in total electron yield (TEY) mode at 2 different incident angles, 10° and 90° (with respect to the surface plane), using horizontally-polarised X-rays.[143, 144].

The NEXAFS spectra were normalised to the beamline transmission by dividing by the I_0 (the photocurrent measured off the final refocussing mirror). Scaling to the calculated atomic photoabsorption cross-section was performed following the methodology described by Gota *et al.* [287] and Ruosi *et al.*[288]

LEED measurements were carried out in a separate UHV chamber on the B07 beamline. Surface images were taken with an Oxford Instruments variable-temperature STM,[289] equipped with Ar ion sputtering and a 3-grid LEED system from Vacuum Generators. The original STM control electronics have been replaced with a R9plus controller from RHK Technology Inc. The irregular shape of the crystal meant that a modified sample holder was employed, which led to the sample temperature thermocouple becoming inaccurate due to the changed position of the e-beam heating filament (a normal sample for this instrument is a 4.5mm square 1mm thick crystal, with filament mounted immediately behind). Imaging was performed at RT. The LEED was used to identify surface structures prior to STM experiments for comparison with the other techniques employed in this work.

The DFT calculations were performed using the VASP code.[290, 291] The generalised gradient approximation (GGA) with the Perdew-Burke-Ernzerhof (PBE) exchange-correlation functional was used to perform the geometry optimisations.[217] A Hubbard (GGA+U) correction was applied to the Fe 3d orbitals, with a U_{eff} value of 4.0 eV.[244] An energy cut-off of 520 eV, 30% above the recommended value for PAW potentials, was used to decrease Pulay errors. $ZnFe_2O_4$ was modelled as a normal spinel, *i.e.* with an inversion degree $x = 0$ (**Figure 4.1a**). The electronic structure calculation used to model the valence band of $ZnFe_2O_4$ was performed using the Heyd, Scuseria and Ernzerhof (HSE06) hybrid functional,[226] which included a 25% Hartree-Fock exchange and range-separated screening with a 0.2 $Å^{-1}$ attenuation parameter. The broadening of the calculated electronic density of states to model the valence band was undertaken using the GALORE code.[292]

5.3 Results

The XPS survey spectra of the $ZnFe_2O_4(111)$ single-crystal prepared by annealing under O_2 and UHV can be seen in **Figure 5.2a**. After preparing the surface in O_2, Fe 2p (~710 eV) and Zn 2p (~1020 eV) peaks and the corresponding LMM Auger signals are present in the spectrum, comparable to those observed for the sputtered surface before any thermal treatment (**Figure 5.2b**). In contrast, when annealed under UHV, the Zn 2p and Auger intensity is significantly decreased compared to the initial sputtered surface, while the Fe 2p and Auger signals maintain their intensity.

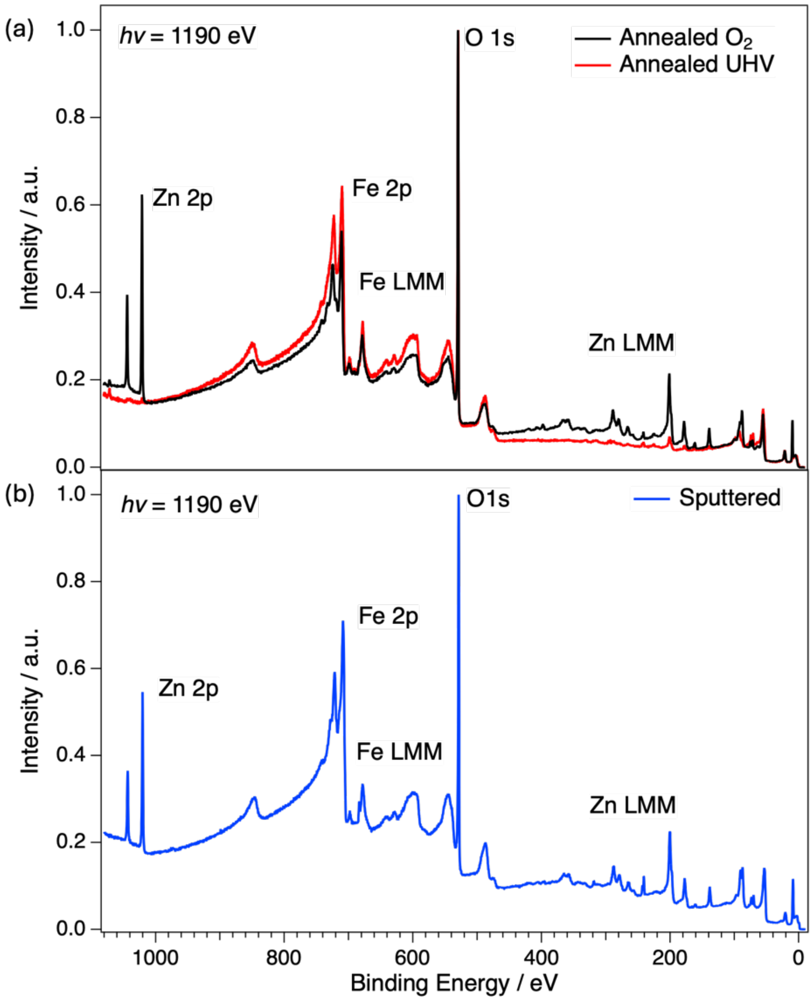

Figure 5.2. The XPS survey spectra of the $ZnFe_2O_4$ (111) (a) annealed under O_2 (black) and UHV (red), and (b) of the sputtered surface (blue) measured at a photon energy of 1190 eV.

The Fe 2p and Zn 2p spectra shown in **Figure 5.3** were recorded with photon energies of 840 eV and 1190 eV, respectively; *i.e.* the photoelectrons had a kinetic energy of ~140 eV probing the sample surface to an approximate depth of 1 nm (calculated as 3 times the inelastic mean free path).[165, 293] The presence of up to three different iron species combined with complex multiplet splitting makes the deconvolution of the Fe $2p_{3/2}$ and $2p_{1/2}$ peaks challenging.[152-154] It is also well established in the literature that Oh and Td Fe^{3+} cannot be distinguished by XPS.[294] However, the different iron oxidation states can be qualitatively distinguished by the binding energy of the Fe 2p satellite peaks.[294-299] The Fe 2p spectra are shown in **Figure 5.3a**. The initial sputtered $ZnFe_2O_4$(111) crystal surface has Fe 2p$_{3/2}$ and Fe 2p$_{3/2}$ satellite peaks at 715.5 eV and 728.6 eV, respectively, corresponding to the Fe^{2+} oxidation state (highlighted by dotted lines). The reduction of the iron species observed during the sputtering process is as expected.[300] When annealed in O_2 the satellite peaks shift to higher binding energies of 719.1 eV and 732.8 eV indicating the presence of Fe^{3+} (highlighted by dashed lines). In contrast, the Fe 2p$_{3/2}$ and Fe 2p$_{1/2}$ satellite features of the UHV annealed surface are indistinguishable, which occurs in samples containing both iron oxidation states, such as magnetite (Fe_3O_4).[295]

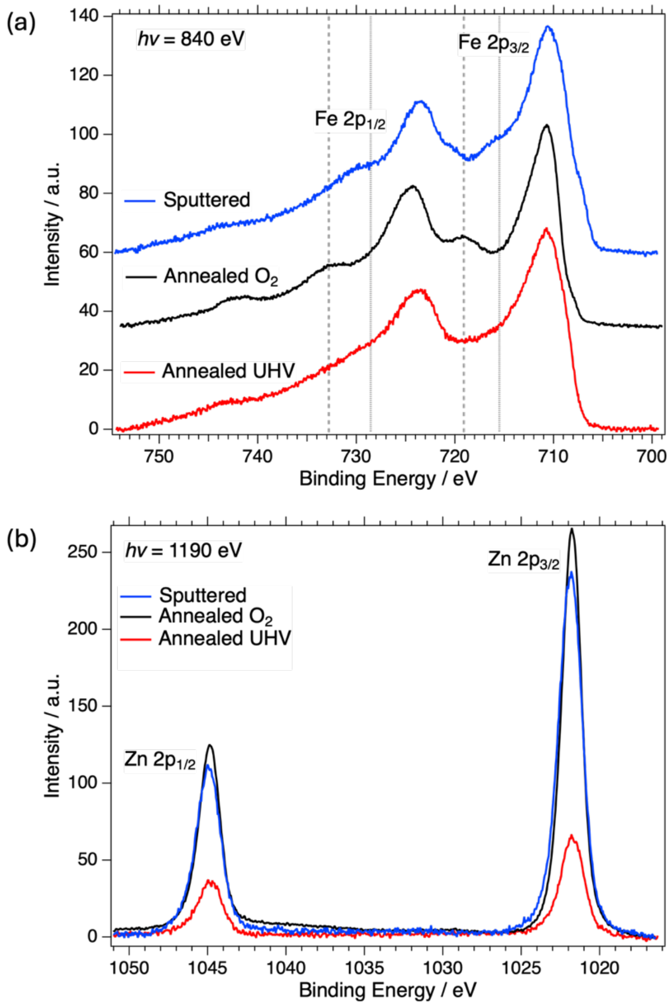

Figure 5.3. The (a) Fe 2p and (b) Zn 2p XPS of the $ZnFe_2O_4$ (111) surface after sputtering (blue), and after annealing in O_2 (black) and UHV (red). The Fe 2p and Zn 2p surveys are measured at photon energies of 840 and 1190 eV, respectively, corresponding to a kinetic energy of ~140 eV. The grey dotted and dashed lines correspond to the positions of the Fe^{2+} and Fe^{3+} satellite features, respectively. The Fe 2p spectra have been offset in the y-axis for clarity.

Similar to the XPS survey measurements, the Zn 2p peak intensity (**Figure 5.3b**), when the sample is annealed in UHV, is significantly lower compared to the intensity when annealed under O_2. The overall intensity is very similar to that seen in the initial sputtered surface. The presence of zinc and iron in the Fe^{3+} oxidation state observed at the surface after being prepared in oxygen is consistent with a zinc-ferrite composition and structure. However, the iron-rich surface with mixed iron vacancy formed under UHV suggests a magnetite-like structure being created on the surface after Zn is evaporated from the surface. The loss of Zn on the sample surface under UHV is similar to that observed in the treatment of other zinc-oxide materials under reducing conditions.[278, 281]

The LEED patterns in **Figure 5.4a,b** (75 eV) show that both preparation methods produce well-ordered crystalline surfaces with sharp integer order spots corresponding to the $ZnFe_2O_4$ (111) surface. In the O_2 annealed surface (**Figure 5.4a**) there is a halo of diffuse intensity surrounding the first-order reflections (see highlighted spot); after annealing in UHV (**Figure 5.4b**) the overall sharpness of the spots is increased, and the halo focusses into superstructure spots corresponding to a moiré lattice with a periodicity approximately 7 times the length of the $ZnFe_2O_4$(111) surface lattice vectors, i.e. around 42 Å. The LEED pattern is identical, both in shape and terms of lattice parameters, to the one observed by Berdunov *et al.*[301] for the oxygen-saturated Fe_3O_4(111) surface.

STM was collected on the UHV-annealed surface as displayed in **Figure 5.4c**. The surface is composed of flat terraces with widths ranging from 2-50 nm and rather randomly oriented, rounded single atomic steps (heights ~0.5 nm, as seen in the line profile in **Figure 5.4f**). Many regions of the crystal had very high step densities and narrow terraces and were unsuitable for high resolution imaging. The terraces and step edges are both decorated with bright round features with heights 0.3-0.6 nm. The terraces also display two different "textures" indicative of different surface terminations; these are depicted in the cartoon in **Figure 5.4d**. The smoother termination (blue region) show "flower-like" features (see enhanced-contrast image in **Figure 5.4e**), which are again very similar to the features observed by Berdunov *et al.* [301, 302] on the "oxygen terminated" Fe_3O_4(111). The features have a periodicity of around 42 Å, compatible with the periodicity observed in LEED. We therefore assign these regions to a pure Fe_3O_4(111) surface termination. The streakier, relatively disordered surface termination (highlighted red in **Figure 5.4d,** see also the section of the line profile in **Figure 5.4f** between 12 and 27 nm) do not seem to contribute to any superstructure. Given the significant enrichment of Fe and almost complete loss of Zn in the near-surface region of the UHV-annealed surface, we assign these regions to a FeOx termination, potentially similar to the "regular" termination of Fe_3O_4 reported in Ref.[301] after annealing. Overall, the two terminations occupy roughly equal areas of the surface of the crystal surface studied by STM.

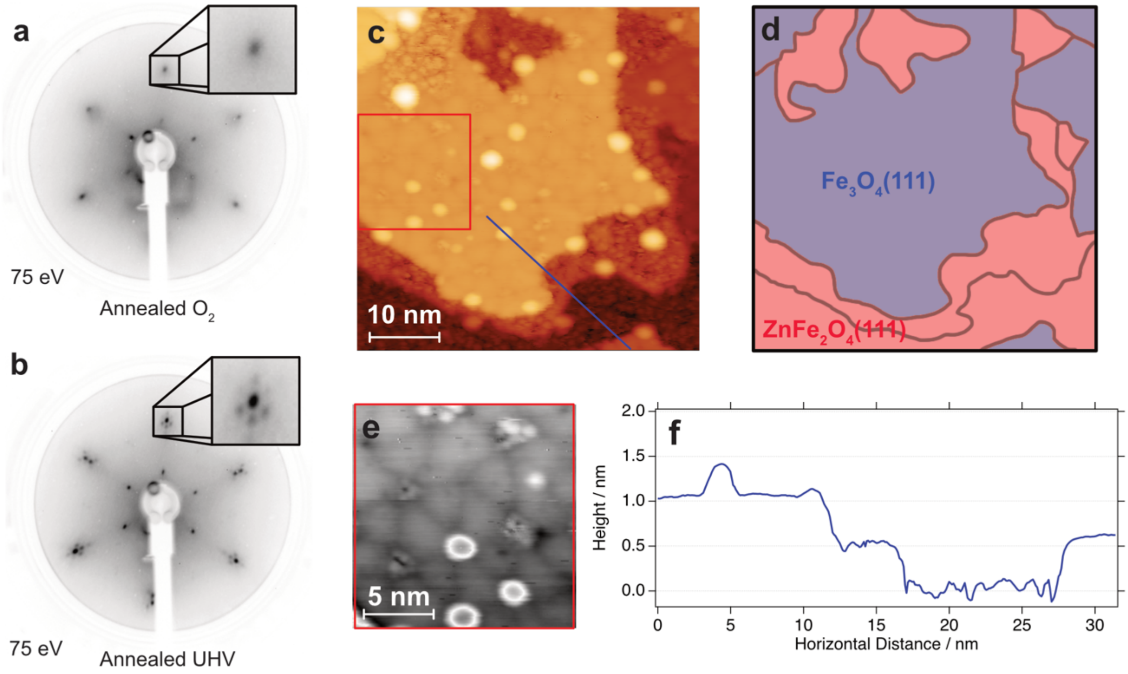

Figure 5.4. LEED (75 eV) of $ZnFe_2O_4$ (111) prepared under (a) oxygen and (b) UHV. (c) A STM topographic image (50 × 50 nm^2, $V_{sample} = 1.0$ V, $I_t = 100$ pA) of the single-crystal surface annealed in UHV. (d) A cartoon map of the surface terminations from the STM image in (c). (e) Inset (16 × 16 nm^2) of the STM image in C with increased contrast to highligh the "flower-like" reconstruction. (f) A line profile across the STM image in (c) indicated with a blue line.

The Fe $L_{2,3}$ NEXAFS measured in TEY mode of the $ZnFe_2O_4$ (111) surfaces prepared under UHV and O_2 are shown in **Figure 5.5**. The data have been scaled to the calculated atomic photoabsorption cross sections before and after the edge, allowing an estimate of the X-ray absorption length ($\lambda(L_3)$) at the Fe L_3 edge (709 eV) of 25 ± 10 nm. [288, 303, 304] Assuming an electron probe depth (*d*) of 4.5 nm, (measured for Fe_3O_4 by Gota *et al.*) [287] this leads to the ratio $\lambda(L_3)/d \approx 5.5$ for the normal incidence NEXAFS (dashed lines in **Figure 5.5**) versus $\lambda(L_3)/d \approx 0.9$ for the grazing incidence NEXAFS, (solid lines in **Figure 5.5**) demonstrating the higher surface sensitivity of the latter measurement geometry.

Measurements at different angles can also probe different orbitals on the sample surface; however, a study of an Fe_3O_4 (111) surface by Kaya *et al.* [305] showed no difference in the Fe L edge at varied angles. This suggests that differences observed in iron edges of the spinel ferrites are due to changes with depth, rather than orbital dependence. Work presented in Chapter 4 demonstrated that the shape and intensity of the spectral features of the Fe $L_{2,3}$ NEXAFS are dependent on the relative quantities of each iron species. The sputtered surface spectra (**Figure 5.6**) at both angles indicate a very reduced, Fe^{2+} rich surface, particularly at grazing incidence. When annealed in O_2, (**Figure 5.5**, black lines) the spectral shape indicates a high presence of Fe^{3+} in octahedral sites and is comparable to the Fe $L_{2,3}$ edge observed in $ZnFe_2O_4$ nanoparticles with a low inversion degree shown in Chapter 4 (**Figure 4.11a**).

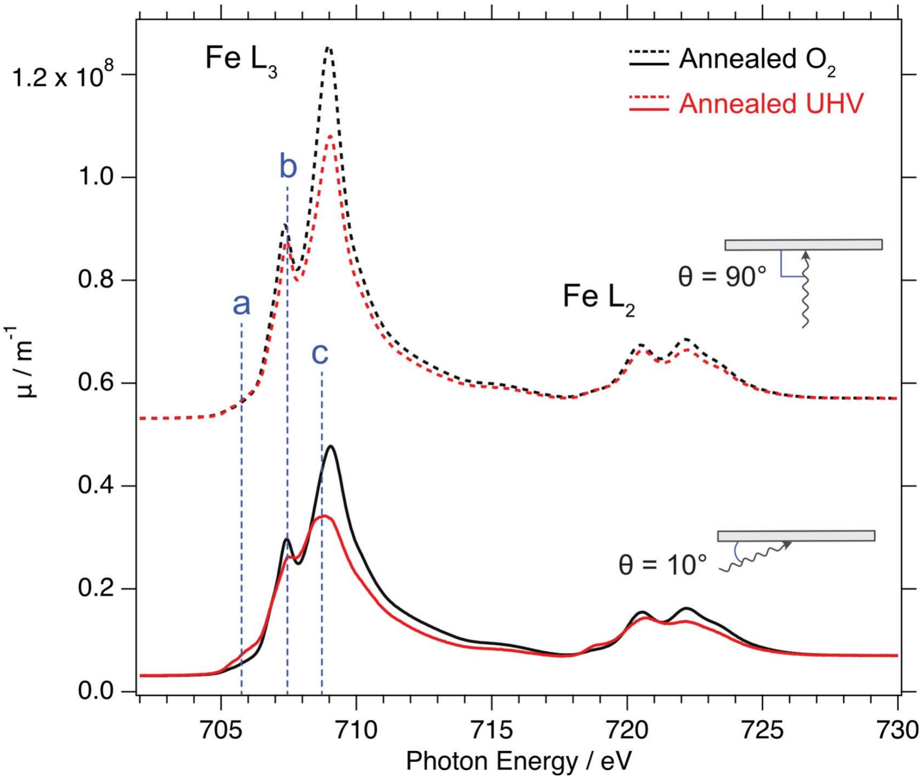

Figure 5.5. The Fe $L_{2,3}$ edge NEXAFS spectra of the $ZnFe_2O_4(111)$ surface annealed under O_2 (red lines) and UHV (black lines) in which the solid lines are measured at an angle of 10° and the dashed lines at an angle of 90°.

For the oxygen annealed surface there was also little difference between the spectra at the two angles, suggesting a similar Fe valency and distribution probing from more surface to more bulk. This supports the idea that when annealing in O_2 the sample surface maintains a more $ZnFe_2O_4$ bulk-like structure. In contrast, there are significant differences observed at different depths when the surface was annealed in UHV (**Figure 5.5**, red lines). The shape, when measured at normal incidence (**Figure 5.5**, dashed red line), is comparable to the O_2 annealed Fe $L_{2,3}$ edges (**Figure 5.5**, black lines). However, the difference in spectral features observed between 706 and 708 eV in the more surface-sensitive grazing incidence spectrum (**Figure 5.5**, solid red line) indicates the presence of more Fe^{2+}_{Oh} and Fe^{3+}_{Td}. This mixed Fe-oxide system is again as expected for a magnetite surface, consistent with the observations from XPS, LEED and STM imaging.

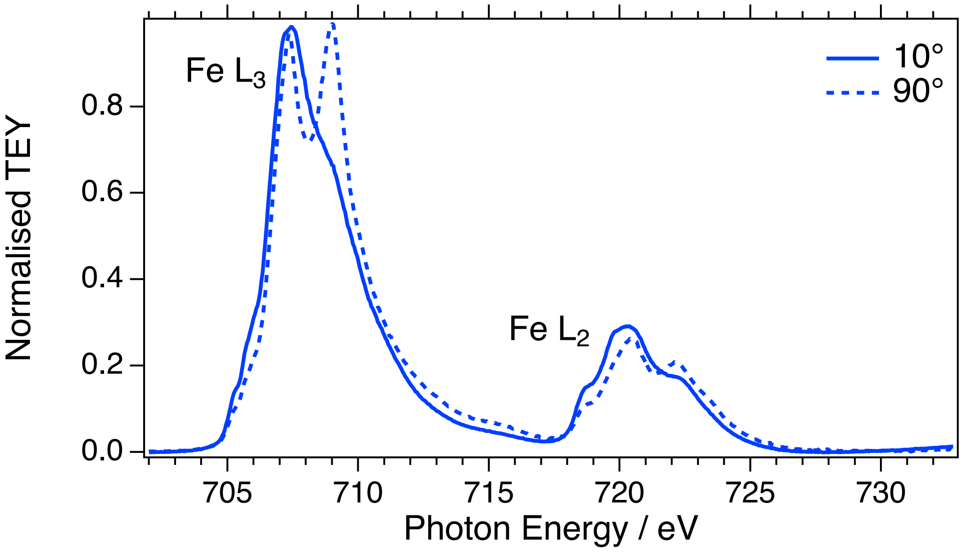

Figure 5.6. Fe L edge NEXAFS of sputtered $ZnFe_2O_4$ (111) surface at 10° (solid line) and 90° (dashed line).

The changes imposed by different annealing temperatures on the valence band and core level XPS spectra for both $ZnFe_2O_4$ (111) single-crystal surfaces were examined. **Figure 5.7a,b** shows the XPS valence bands measured at different temperatures with a surface-sensitive kinetic energy of 100 eV, probing ~1 nm depth, under UHV and O_2 pressure. The feature seen at ~10 eV is attributed mainly to the Zn 3d orbitals. The DFT-calculated valence band (**Figure 5.7c**) shows a similar spectral shape to the measured XPS valence bands, with Zn 3d orbitals being the main contribution to the high binding energy peak. The calculated peak position is ~4 eV lower than the experimental peak, due to the HSE06 hybrid functional's limitations for the calculation of Zn 3d orbital binding energies; studies on other zinc oxide materials have shown that using a higher level of theory, such as the GW approach, can improve the calculated energies.[306] For this study, the HSE level calculations were sufficient to identify the Zn 3d contribution as the feature seen experimentally at ~10 eV. When annealed in O_2 this feature remains present across the full temperature range from the sputtered surface to 600 °C. (**Figure 5.7a**) However, when annealed in UHV above 500 °C, the Zn 3d peak rapidly decreases and by 600 °C no peak is present (**Figure 5.7b**). These changes in the peaks of the Zn core levels from RT to 600 °C and then returning to RT are visualised in **Figure 5.7d**.

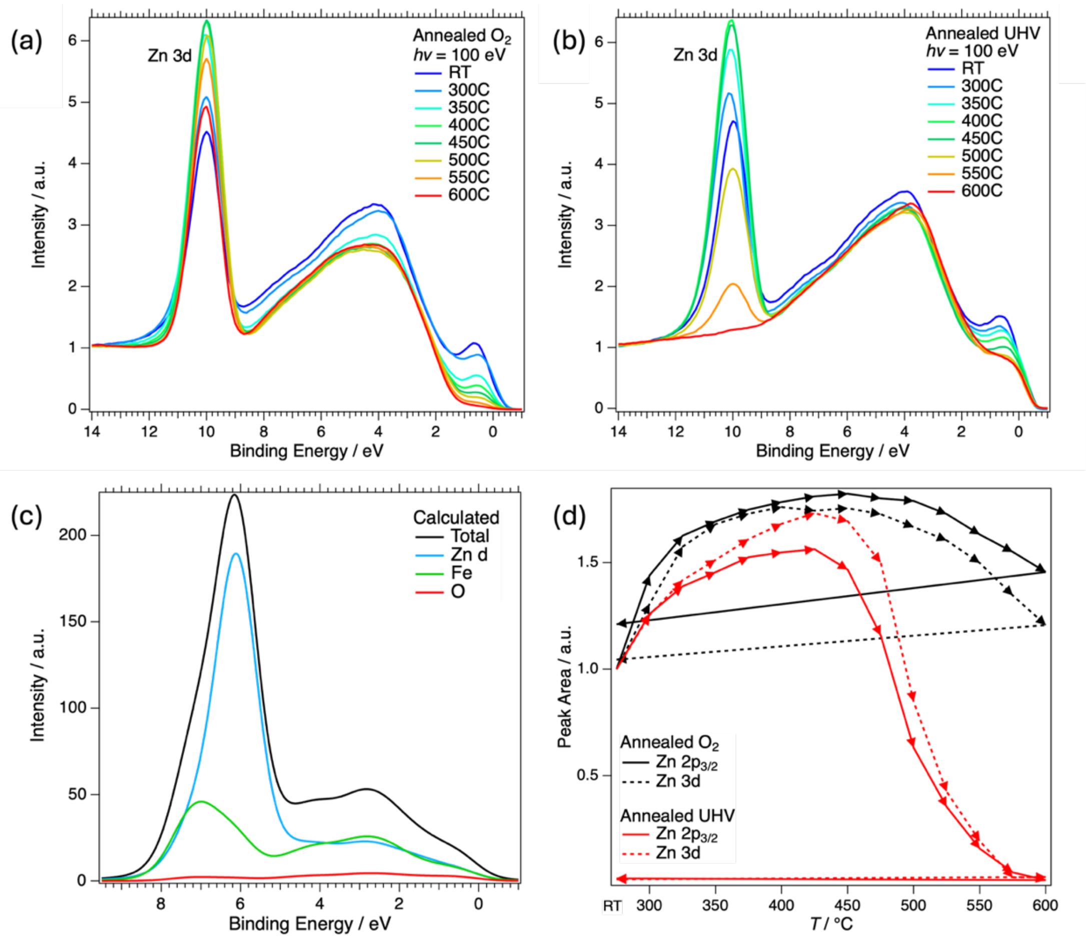

Figure 5.7. XPS valence bands of $ZnFe_2O_4$ (111) annealed under (a) O_2 and (b) UHV as a function of temperature at a photon energy of 100 eV. (c) DFT calculated valence band of bulk $ZnFe_2O_4$. (d) The peak area of the Zn core levels as a function of temperature in which $2p_{3/2}$ and 3d areas are represented by solid lines and dotted lines, respectively.

The valence band also provides information about the iron oxidation state. The presence of a peak near the Fermi edge (~ 0.5 eV) is attributed to reduced iron species of Fe^{2+} (refs. [298, 307]) or metallic iron.[308] The peak near the Fermi energy, at around 0.5 eV, observed in the spectra of the sputtered valence bands before thermal treatment (**Figure 5.7a,b**) is concordant with the presence of Fe^{2+} and metallic Fe. When annealed in O_2 the feature intensity significantly decreases, and at 600°C there are little traces of reduced iron species, with a spectral shape similar to that seen in other Fe^{3+} oxides.[307] The feature intensity decreases less when annealed under UHV compared to O_2, and the resulting spectrum is comparable to that observed in a magnetite surface, with both Fe^{3+} and Fe^{2+} present.[298]

The change in core level Fe 2p and Zn 2p spectra as a function of temperature is shown in **Figure 5.8**. Little changes are observed in the Fe $2p_{3/2}$ and Fe $2p_{1/2}$ intensities (**Figure 5.8a,c**) under both annealing conditions. However, as expected, the Zn 2p peak intensities (**Figure 5.8b,d**) follow the same trends as the Zn 3d peaks in the valence bands, as seen in **Figure 5.7d**.

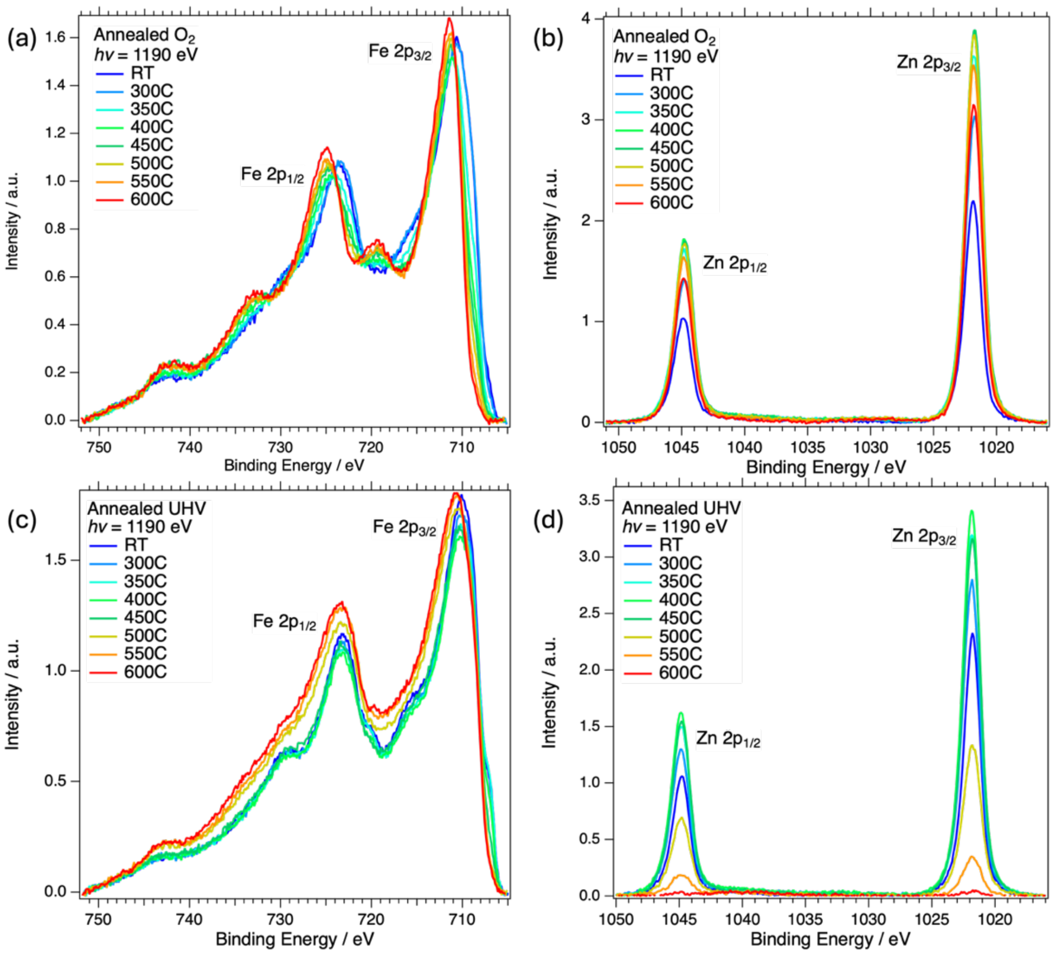

Figure 5.8. The Fe 2p and Zn 2p core level XPS of the $ZnFe_2O_4$ (111) surface annealed under (a-b) O_2 and (c-d) UHV as a function of temperature measured at a photon energy of 1190 eV.

Like the valence bands, changes in iron valency are demonstrated in the Fe 2p XPS across the temperature range for both preparation methods. The initial RT measurements of the sputtered surfaces have the Fe^{2+} satellite features, as seen in **Figure 5.3b**, demonstrating the reduced surface. When annealing in O_2 above 350 °C the Fe^{2+} features reduce, and Fe^{3+} satellite peaks become apparent, with a significant Fe^{3+} satellite peak present at 600 °C. The Fe 2p peak shift of ~ 0.6 eV is similar to the difference in peak positions between Fe^{2+} and Fe^{3+} iron oxides.[297, 299] When annealing under UHV a significant change in the Fe 2p satellite features occurs at 500 °C, where the Fe^{2+} satellite features becomes more like that of a mixed Fe^{2+}/Fe^{3+} oxidation state. A smaller shift in the Fe 2p peaks (~0.2 eV) is observed across the temperature range compared to the O_2 annealed shift.

To help rationalise the surface change from zinc ferrite to magnetite when annealed in UHV, we performed a DFT analysis of the thermodynamics of the reaction:

$$\mathrm{ZnFe_2O_4} \rightarrow \frac{2}{3}\mathrm{Fe_3O_4} + \mathrm{Zn_{(g)}} + \frac{2}{3}\mathrm{O_{2\,(g)}}. \tag{18}$$

The Gibbs free energy change (ΔG) of the reaction above can be estimated as:

$$\Delta G = \frac{2}{3}G_{\mathrm{Fe_3O_4}} + G_{\mathrm{Zn}} + \frac{2}{3}G_{\mathrm{O_2}} - G_{\mathrm{ZnFe_2O_4}} \tag{19}$$

where $G_{\mathrm{Fe_3O_4}}$, G_{Zn}, $G_{\mathrm{O_2}}$, and $G_{\mathrm{ZnFe_2O_4}}$are the Gibbs free energies of magnetite, molecular oxygen in gas phase, atomic zinc in gas phase, and zinc ferrite, respectively. The Gibbs free energy of the spinels (Fe_3O_4 and $ZnFe_2O_4$) are approximately equivalent to their respective calculated DFT energies. To estimate the Gibbs free energy of gas-phase oxygen molecules and zinc atoms, we need to consider their partial pressures. As typically done in *ab initio* thermodynamics,[309-311] the Gibbs free energy of molecular oxygen can be estimated, using a DFT reference level, as a function of oxygen partial pressure $p_{\mathrm{O_2}}$:

$$G_{\mathrm{O_2}} \approx E_{\mathrm{DFT\,O_2}} + \Delta G_{\mathrm{O_2}}(p_0, T) + k_{\mathrm{B}}T \ln\left(\frac{p_{\mathrm{O_2}}}{p_0}\right) + \mathrm{ZPE_{O_2}} \tag{20}$$

where $E_{\mathrm{DFT\,O_2}}$ is the DFT energy of an oxygen molecule, and $\mathrm{ZPE_{O_2}}$ is the zero-point energy of the oxygen molecule, 9.31 kJ mol^{-1}.[240] The change of Gibbs free energy per oxygen molecule, $\Delta G_{\mathrm{O_2}}(p_0, T)$, between 0 K and T, at constant pressure p_0, is related to the entropy (S) and enthalpy (H) of O_2 by the following equation:

$$\Delta G_{\mathrm{O_2}}(p_0, T) = H(T, p_0) - H(0\ \mathrm{K}, p_0) - TS(T, p_0), \tag{21}$$

where the values of H and S are extracted from thermochemical tables for a range of temperatures at $p_0 = 1$ bar.[312] The DFT energy of an oxygen molecule is not directly calculated due to the well-known O-O over binding in the GGA. Therefore $E_{\mathrm{DFT\,O_2}}$ is calculated as:

$$E_{\mathrm{DFT\,O_2}} = 2E_{\mathrm{DFT\,O}} + D_{\mathrm{exp\,O_2}} \tag{22}$$

where $E_{\mathrm{DFT\ O}}$ is the DFT energy of an oxygen atom in its magnetic groundstate, and $D_{\mathrm{exp\ O_2}}$ is the experimental dissociation energy of an oxygen molecule, 498 kJ mol^{-1}.[313, 314] Finally, the Gibbs free energy of a zinc atom is described by a similar equation to oxygen:

$$G_{\mathrm{Zn}} \approx E_{\mathrm{DFT\ Zn}} + \Delta G_{\mathrm{Zn}}(p_0, T) + k_{\mathrm{B}} T \ln\left(\frac{p_{\mathrm{Zn}}}{p_0}\right), \tag{23}$$

where the DFT energy of a zinc atom was calculated directly and the entropy and enthalpy values for Zn were taken from thermochemical tables.[312]

Figure 5.9 shows the calculated Gibbs free energy of the reaction under both UHV and with an O_2 pressure that mimic the experimental conditions. The reaction free energy depends on the partial pressures of both oxygen and zinc. However, to simplify the analysis, the total pressure, $p = p_{\mathrm{Zn}} + p_{\mathrm{O_2}}$, was fixed and a range of ratios of Zn and O_2 gas ($p_{\mathrm{Zn}}/p_{\mathrm{O_2}}$) was considered. The maximum partial pressure ratio considered is 1.5, corresponding to the relative Zn/Fe ratio in the reaction equation. The temperature at which ΔG becomes negative, and the reaction therefore becomes thermodynamically favourable, decreases slightly with decreasing $p_{\mathrm{Zn}}/p_{\mathrm{O_2}}$ ratio, but in general the results depend only very weakly on the pressure ratio used.

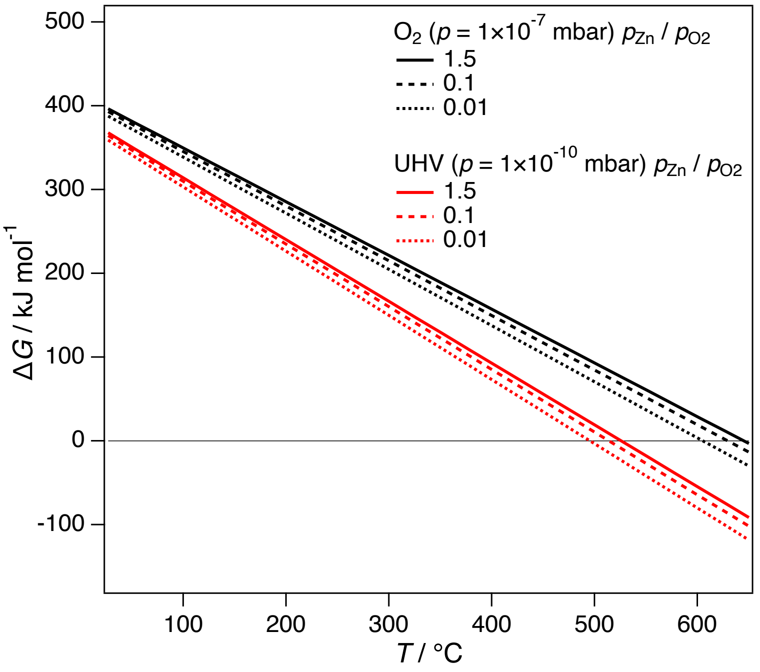

Figure 5.9. DFT calculated Gibbs free energy (Δ*G*) of the proposed reaction of forming magnetite from zinc ferrite as a function of temperature, *T*.

Under UHV conditions and $p_{\mathrm{Zn}}/p_{\mathrm{O_2}}$ = 1.5, ΔG becomes negative at ~520°C, a temperature close to that at which the Zn depletion starts to be observed experimentally (~500°C under UHV). In contrast, under an O_2 atmosphere the reaction does not become thermodynamically favourable until higher temperatures (> 600°C), above the experimental temperatures reached, even at a low partial pressure ratio of 0.01. Although the DFT model is very approximate (ignoring vibrational effects in the solid face, complex surface reconstructions, all kinetic effects, etc), it illustrates how it is thermodynamically favourable for magnetite to form under UHV conditions, whereas in an O_2 atmosphere the material maintains its $ZnFe_2O_4$ structure.

5.4 Chapter Conclusions

Our combination of experimental and theoretical techniques to study a $ZnFe_2O_4$(111) terminated single-crystal has provided insights into how the surface structure is dependent on its preparation method. The XPS analysis of the two preparation methods reveals a significant loss of Zn on the surface when annealed in UHV, creating an iron-rich surface, which does not happen when annealing in an O_2 atmosphere of 10^{-7} mbar. The Fe 2p satellite features of the O_2 annealed and the UHV annealed surfaces indicate the presence of Fe^{3+} and a Fe^{2+}/Fe^{3+} mixed valency, respectively. Surface-sensitive NEXAFS measurements show the same oxidation states as identified in the Fe 2p XPS spectra. The Fe $L_{2,3}$ edge measurements at different depths showed little difference in the Fe oxidation states and coordination when annealed in O_2 with both spectral shapes being comparable to a $ZnFe_2O_4$ sample with a low inversion degree. When annealing in UHV, the difference between the Fe $L_{2,3}$ edge shape at 10° and 90° incidence angles can be attributed to the presence of more Fe^{2+}_{Oh} and Fe^{3+}_{Td} at the surface, whereas the bulk, like the O_2 annealed surface, has more Fe^{3+}_{Oh}. LEED and STM investigations also indicate a magnetite-like reconstruction at the $ZnFe_2O_4$ surface when annealed in UHV conditions.

Temperature-dependent XPS revealed that Zn sublimation from the surface starts to occur at ~ 500 °C under UHV, and by 600 °C the Zn is almost completely removed, leaving a mixed Fe^{2+}/Fe^{3+} iron rich surface. Under O_2 the relative amounts of Zn/Fe remain unchanged at the surface pre- and post-annealing at high temperatures. Based on the analysis of the iron NEXAFS and XPS, the iron-rich surface created under UHV is likely to be a magnetite structure. The *ab initio* analysis of the reaction thermodynamics of $ZnFe_2O_4$ to Fe_3O_4 indeed suggests that this transformation is favourable at UHV conditions and temperatures above ~500 °C, while unfavourable under higher oxygen partial pressures.

This study has demonstrated the significant effect surface treatment can have on a $ZnFe_2O_4$ sample. The volatility of Zn needs to be considered when studying zinc ferrite samples, especially under high temperature conditions. Further work should continue to study the surface effects of $ZnFe_2O_4$ and how it could play a critical role in developing its catalytic abilities.

Chapter 6. B-site substitutions: understanding the structural, electronic, and photocatalytic properties of $ZnFeGaO_4$ and $ZnGa_2O_4$

Chapter Overview

In this work the structure and photocatalytic behaviour of $ZnFeGaO_4$ and $ZnGa_2O_4$ nanoparticles was studied with a combination of theoretical and experimental techniques. Photocatalytic testing showed that only $ZnFeGaO_4$ demonstrates activity for the oxygen evolution reaction. Powder X-ray diffraction and X-ray absorption spectroscopy measurements show that Fe^{3+} is in Oh coordination. However, the Zn L_3 edge indicated a small presence of $Zn^{2+}{}_{Oh}$, suggesting a low inversion degree caused by Ga^{3+} in Td sites. Limitations in the DFT modelling of transition metals need to be considered, therefore we designed a correction to the relative energies of tetrahedral vs octahedral site occupancy, to be applied to the spinel systems, by using calculated energies and experimental enthalpies of formation of metal-oxide standards. The corrected DFT thermodynamic studies showed that both $ZnFeGaO_4$ and $ZnGa_2O_4$ generally prefer a normal cation distribution ($x = 0$). However, at high temperatures (e.g. 900 K), low levels of inversion ($x = 0.11$) can occur in $ZnFeGaO_4$, with the Ga^{3+} preferentially moving to Td sites, over Fe^{3+}. Because the predicted inversion is small, and for the sake of simplicity, all the electronic structure calculations were conducted with $x = 0$ as a suitable assumption. The band alignments of both $ZnFeGaO_4$ and $ZnGa_2O_4$ demonstrate favourable band alignments for the OER. However, the band gap of $ZnGa_2O_4$ (4.10 eV) is larger than the $ZnFeGaO_4$ gap (3.35 eV), resulting in the lack of oxygen evolution. Our findings demonstrate the ability to influence the photocatalytic behaviour of spinels by doping the B site cations.

Statement of contributions

The work in this Chapter was a collaboration with Prof. Maria Retuerto (MR), Dr Ivan da Silva (IdS) and Dr Santosh Kumar (SK). Samples were synthesised by MR. The PXRD measurements, data processing and Rietveld refinements were conducted by IdS. The catalytic activity measurements were conducted by SK.

6.1 Introduction

In Chapter 4 we investigated the effect of A cation substitution in spinel ferrites and demonstrated the significantly higher catalytic activity of $ZnFe_2O_4$ for the oxygen evolution reaction (OER) compared to $CoFe_2O_4$ and $CuFe_2O_4$. This was attributed to its favourable band alignment (as calculated by DFT) with respect to the OER potential.

This Chapter focuses on the effect of B cation substitution in $ZnFe_2O_4$. As highlighted in Chapter 1, studies have demonstrated an improved photocatalytic ability of zinc ferrite with the introduction of Ga to the B sites.[110, 125, 129] Xu *et al.*[129] and Kalia *et al.*[125] independently report Ga-doped zinc ferrite as being active for the hydrogen evolution reaction (HER), however our studies found that $ZnFe_2O_4$ was only active for the OER.

In this study we investigate the oxygen evolution of $ZnFeGaO_4$ and $ZnGa_2O_4$ nanoparticle samples to compare with $ZnFe_2O_4$ using a combination of computational and experimental techniques. Simulations offer insights into electronic structure and photocatalytic properties, which help to rationalise their experimental activity for the water splitting process. We also use advanced computational methods, X-ray diffraction and X-ray absorption techniques to study the respective structures of $ZnFeGaO_4$ and $ZnGa_2O_4$.

6.2 Methods

6.2.1 Ab-initio simulations

The *ab-initio* calculations were completed using DFT within the VASP code.[290, 291] For the geometry optimisations the generalised gradient approximation (GGA) was used with the PBE exchange-correlation functional. For the $ZnFeGaO_4$ calculations, a Hubbard correction with a U_{eff} value of 4.0 eV was applied to the Fe 3d orbitals.[244] The projector augmented wave (PAW) method was used to describe the interaction between core and valence electrons.[228] In order to decrease Pulay errors, an energy cut-off of 520 eV, 30% above the recommended value for PAW potentials.

Primitive unit cells of $ZnFeGaO_4$ and $ZnGa_2O_4$, which contain two formula units were modelled. $ZnGa_2O_4$ was modelled with inversion degrees of $x = 0$, 0.5 and 1, of which there is only one symmetrically different configuration for each x in the primitive unit cell. The $ZnGa_2O_4$ models were similar to the $ZnFe_2O_4$ models seen in **Figure 4.1**. For $ZnFeGaO_4$, we considered the 6 symmetrically different possible configurations due to the possibility for either Fe or Ga to move to Td sites in the partially or fully inverse configurations. The 6 structures can be seen in **Figure 6.1**. From the relative corrected energies, we can calculate the inversion energy (ΔE_{conf}), accounting for the configurational contribution only.

For the most stable structure of each spinel, electronic structure calculations were conducted to determine their band gaps and alignments. For these calculations the hybrid functional by Heyd, Scuseria and Ernzerhof (HSE06)[226] was used. The previous studies of $ZnFe_2O_4$ presented in Chapter 4 found that the GGA+U approximation was acceptable for optimisation, resulting in very close cell parameters and band gaps (within 0.5%) compared to those calculated by HSE06.[135] Therefore, the HSE06 electronic structure calculations were completed using the structures optimised at the GGA+U level, *i.e.* the structures were not re-optimised at the HSE06 level.

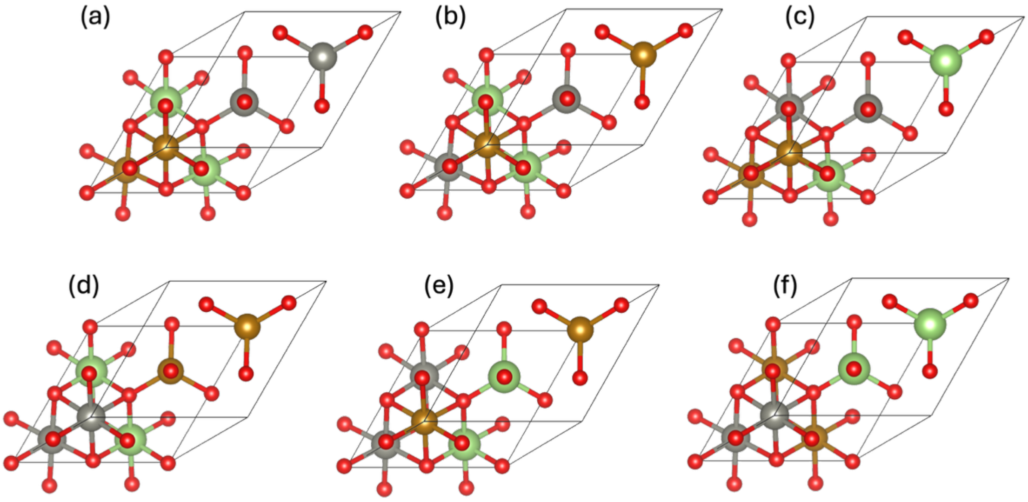

Figure 6.1. The models of the primitive unit cells of $ZnFeGaO_4$ with inversion degrees of (a) $x = 0$, (b-c) $x = 0.5$, and (d-f) $x = 1$ used for the DFT simulations. Colour scheme: Zn = silver; Fe = gold; Ga = green; oxygen = red.

In the calculations of $ZnFeGaO_4$, the magnetic moment for Fe^{3+} was initialised in a high-spin state.[9, 74, 250] Test calculations were run with different spin states and in all cases the high-spin configuration was most stable. All possible magnetic moment orientations were considered to initialise the magnetic ground state. In the normally distributed $ZnFeGaO_4$, the lowest energy was observed in an antiferromagnetic configuration of Fe^{3+} in Oh sites. When partially or fully inverse, the Fe^{3+} in Td and Oh sites had opposite magnetic moments.

To estimate the offset in the macroscopic electrostatic potential between the bulk and the vacuum level, periodic slab models of $ZnFeGaO_4$ and $ZnGa_2O_4$ with (100) terminated surfaces and a 10 Å vacuum gap were optimised using the same parameters outlined for the bulk GGA+U calculations. Due to spinels being Tasker type-III surfaces (in which there is a dipole moment perpendicular to the surface),[234] reconstruction was required to achieve a stoichiometric and non-polar surface model. The reconstructed slab surfaces can be seen in **Figure 6.2**.

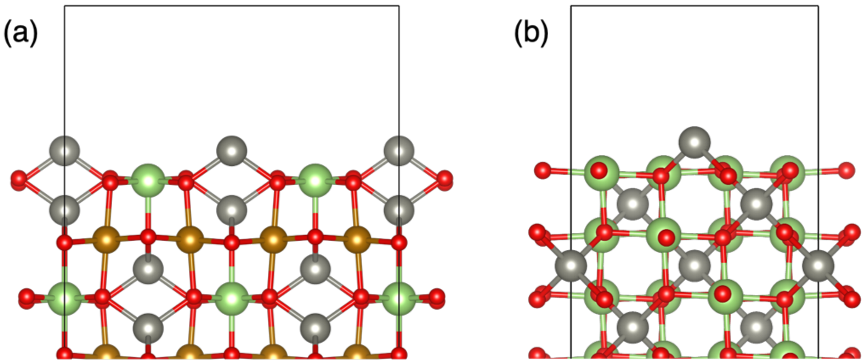

Figure 6.2. Surface structures of (a) $ZnFeGaO_4$ (100) and (b) $ZnGa_2O_4$ (100) surface reconstructions leading to stoichiometric and non-polar terminations. Only one side of the slab is shown but the other side of the slab is equivalent by symmetry. Colour scheme: Zn = silver; Fe = gold; Ga = green; oxygen = red.

6.2.2 Sample preparation

The $ZnFeGaO_4$ powder sample was prepared using equal molar ratios of the precursors ZnO, Ga_2O_3 and $Fe(NO_3)_3{\cdot}9H_2O$. The precursors were mixed and ground using an agate mortar before being heated to 450 °C for 12 hours, then to 900 °C for 12 hours in air (muffle oven) and then finally to 1200 °C for 12 hours in air (tube furnace). The samples were then cooled slowly to room temperature in air.

The same synthesis process was repeated for $ZnGa_2O_4$, with equal molar ratios of the precursors ZnO and Ga_2O_4.

6.2.3 Powder X-Ray diffraction

Powder X-ray diffraction (PXRD) patterns of $ZnFeGaO_4$ and $ZnGa_2O_4$ samples were collected on a Rigaku SmartLab diffractometer, using Cu $K\alpha_1$ radiation, in reflection mode and at room temperature, over a 2θ range of 10 – 110°. Topas Academic v6 software was used to implement the Rietveld method for fitting the PXRD patterns and crystal-structure refinements. A normal spinel structure was used as a structural starting point for the refinements.

To calculate the broadening effects, due to crystalline size, and perform particle size analysis, the instrument peak profile parameters were used. A silicon NIST-640C standard reference sample was measured at the same conditions as the two spinel samples to determine these parameters.

6.2.4 Catalytic testing

The catalytic testing was undertaken at the Catalysis Hub based at the Research Complex at Harwell. The photocatalytic oxygen evolution was measured in a gas-tight 50 mL quartz photoreactor at room temperature. An AM 1.5G mass filtered 300 W Xe source was used to produce a light intensity equivalent to 1 sun (100 mW cm^{-2}). For each measurement, 25 mg of the spinel samples $ZnFeGaO_4$ and $ZnGa_2O_4$ in a 0.5 M $AgNO_3$ medium (acting as the hole scavenger) was used. Before the measurements, the system was purged for 1 hour with 1.5 bar Ar gas. The oxygen evolution was measured over a period of 5 hours and the gas composition was monitored by gas chromatography with a barrier ionisation discharge (BID) detector (GC, Shimadzu GC-2010 Plus). To normalise the oxygen evolution data, reference measurements for each medium were taken; further details of the control measurements can be seen in **Figure 6.3**.

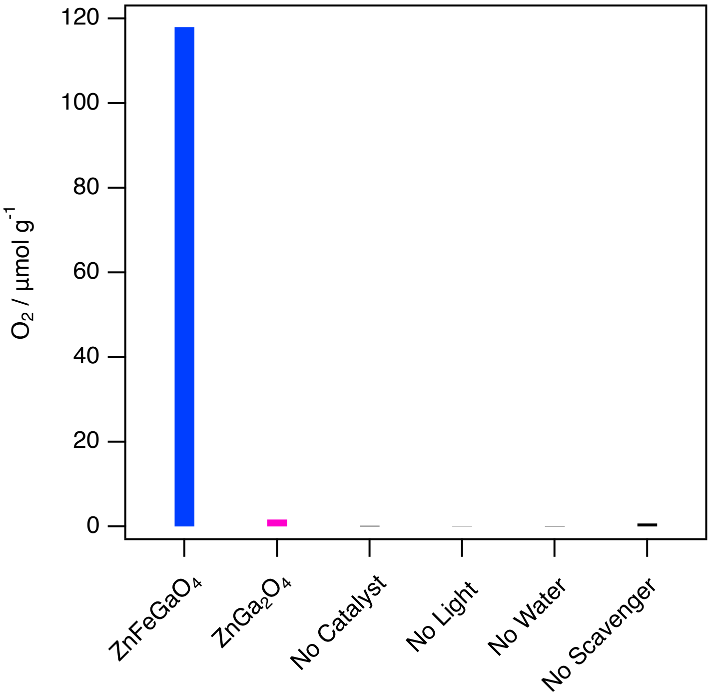

Figure 6.3. The amount of oxygen produced by the spinels $ZnFeGaO_4$ and $ZnGa_2O_4$ and the oxygen produced by the control measurements: with no catalyst, or with the $ZnFe_2O_4$ catalyst in conjunction with previous work but no UV light, no water or no $AgNO_3$ sacrificial agent (scavenger).

6.2.5 Near-edge X-Ray absorption fine structure

Near-edge X-ray absorption fine structure (NEXAFS) measurements were carried out at DLS on branch B of the B07 (VerSoX) beamline.[143, 144] The data were collected in total electron yield (TEY) mode under 1 mbar helium.

The NEXAFS spectra were all corrected for the beamline transmission by dividing through I_0, the photocurrent measured off the final refocussing mirror. The low-photon energy background was then subtracted and finally normalised with respect to the step height at the high photon energy side, outside the resonances. For the Fe $L_{2,3}$ edge the background and edge jumps were subtracted with a Fermi-Dirac step function. Two step functions with a width of 1 eV were used with a 2:1 jump ratio for the L_3 and L_2 edges, respectively. The edge jump position was shifted by 3 eV with respect to the peak maximum.[259] The Zn L_3 edge were normalised with respect to the peak maxima.

6.3 Results

Firstly, we discuss the suitability of the spinels as photocatalysts for the water splitting reaction. The activities of $ZnFeGaO_4$ and $ZnGa_2O_4$ with respect to the OER using an Ag^+ ion electron sacrificial agent under simulated solar light are shown in **Figure 6.4**. After 5 hours, $ZnFeGaO_4$ produced approximately 120 μmol g^{-1} of O_2, significantly more than the amount of O_2 produced by $ZnGa_2O_4$ (< 2 μmol g^{-1}). $ZnFeGaO_4$ also shows more efficiency as a photocatalyst for the OER compared with $ZnFe_2O_4$, which produced 65 μmol g^{-1} O_2 under the same experimental conditions.[135]

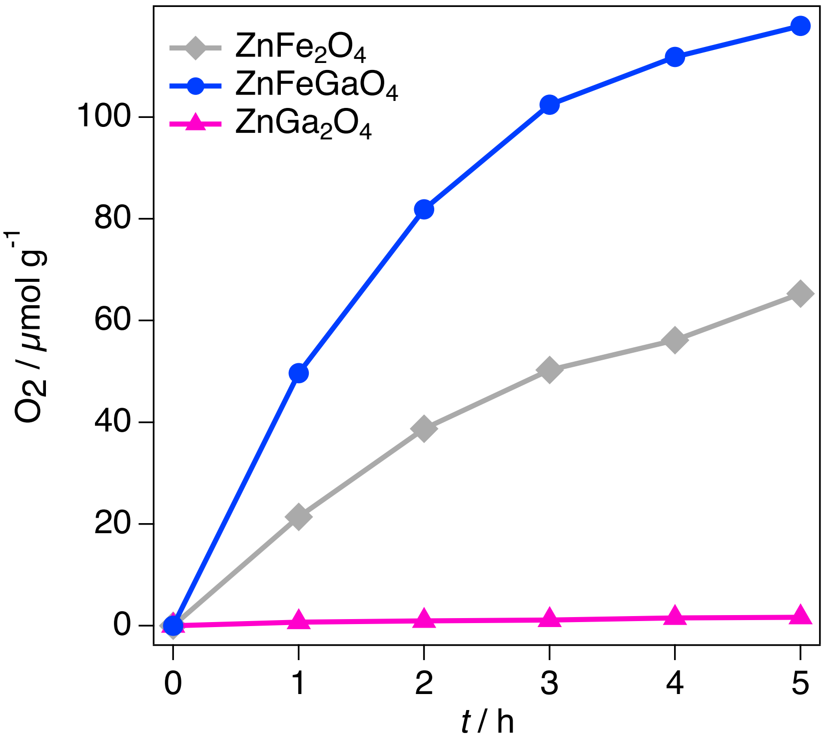

Figure 6.4. Photocatalytic oxygen evolution of $ZnFe_2O_4$, $ZnFeGaO_4$, and $ZnGa_2O_4$ over a time of 5 hours under simulated sun light using $AgNO_3$ as an electron sacrificial agent.

In order to rationalise the suitability of these spinels as photocatalysts, we need to understand their relative structures and configurations. Nanoparticle size, cell parameter (a) and oxygen coordinate parameter (u) as determined by PXRD with the Rietveld method analysis are shown in **Table 6.1** and the corresponding patterns can be seen in **Figure 6.5**.

Table 6.1. Summary of experimentally determined structural parameters: size, a (cell parameter), u, and R_{wp} (weighted profile R-factor). The u parameter determines the O atoms coordinates (u, u, u) in the standard setting of the *Fd-3m* space group.

	Experimental (nanoparticles at room temperature)				DFT (bulk at 0 K)		
Sample	Size / nm	a / Å	u	R_{wp} /%	x	a / Å	u
$ZnFeGaO_4$	130(3)	8.393(1)	0.23(2)	4.17	0	8.455	0.239
$ZnGa_2O_4$	120(1)	8.333(2)	0.23(1)	9.47	0	8.423	0.239

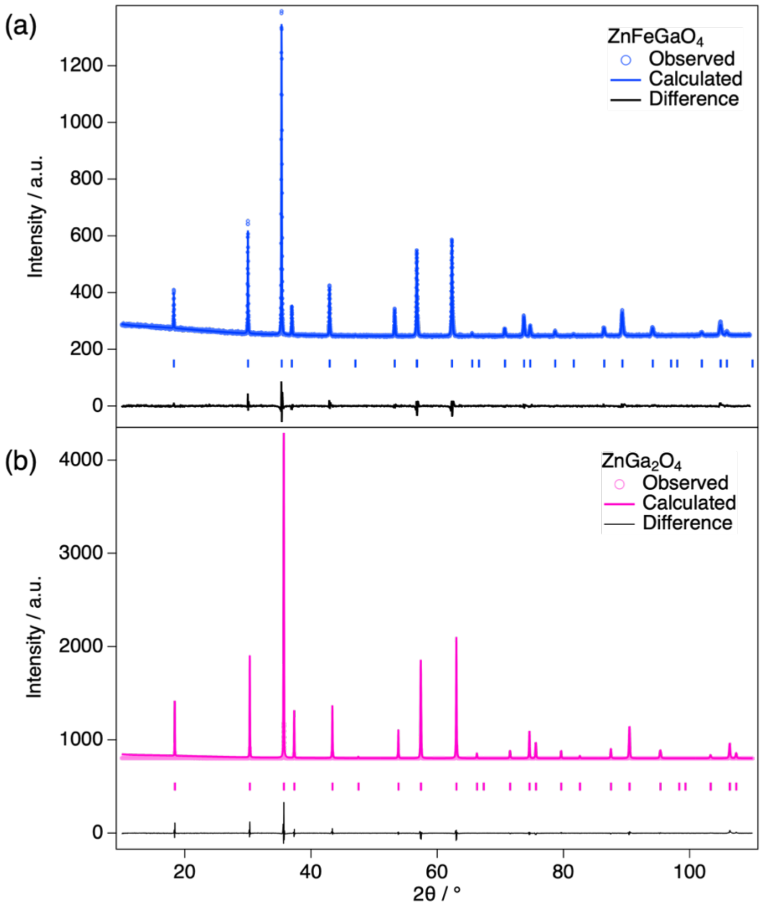

Figure 6.5. The PXRD patterns of (a) ZnFeGaO$_4$ and (b) ZnGa$_2$O$_4$.

The particle sizes of ZnGa$_2$O$_4$ and ZnFeGaO$_4$ are 120 and 130 nm, respectively. For both spinels, determining the cation distribution by PXRD is difficult due to their similar atomic numbers of Zn (30) and Ga (31), which makes them indistinguishable. However, in the ZnFeGaO$_4$ sample it is possible to distinguish the iron cations, and the PXRD data demonstrated that Fe occupies < 1% of the Td sites.

Although we are unable to determine the complete cation distribution by PXRD, spectroscopic techniques, such as X-ray absorption spectroscopy (XAS), can provide information about cation oxidation and distribution. **Figure 6.6** shows the Fe $L_{2,3}$ NEXAFS measured in TEY mode of the ZnFeGaO$_4$ sample. The spectral shape of the edge is dependent on the relative amounts of iron species (Fe^{2+}_{Oh}, Fe^{3+}_{Td}, and Fe^{3+}_{Oh}) present in the sample. The spectral shape of the ZnFeGaO$_4$ Fe $L_{2,3}$ edge is very similar to that of the Fe^{3+} in octahedral coordination as calculated using CTM4XAS[237, 239, 256, 257] (the full simulation parameters are outlined in Chapter 4). The calculated spectral shape of Fe^{3+}_{Td} and Fe^{2+}_{Oh}, which shows significant differences with respect to the $ZnFeGaO_4$ Fe $L_{2,3}$ edge. The lack of spectral evidence of tetrahedrally coordinated Fe in $ZnFeGaO_4$ agrees with the PXRD results.

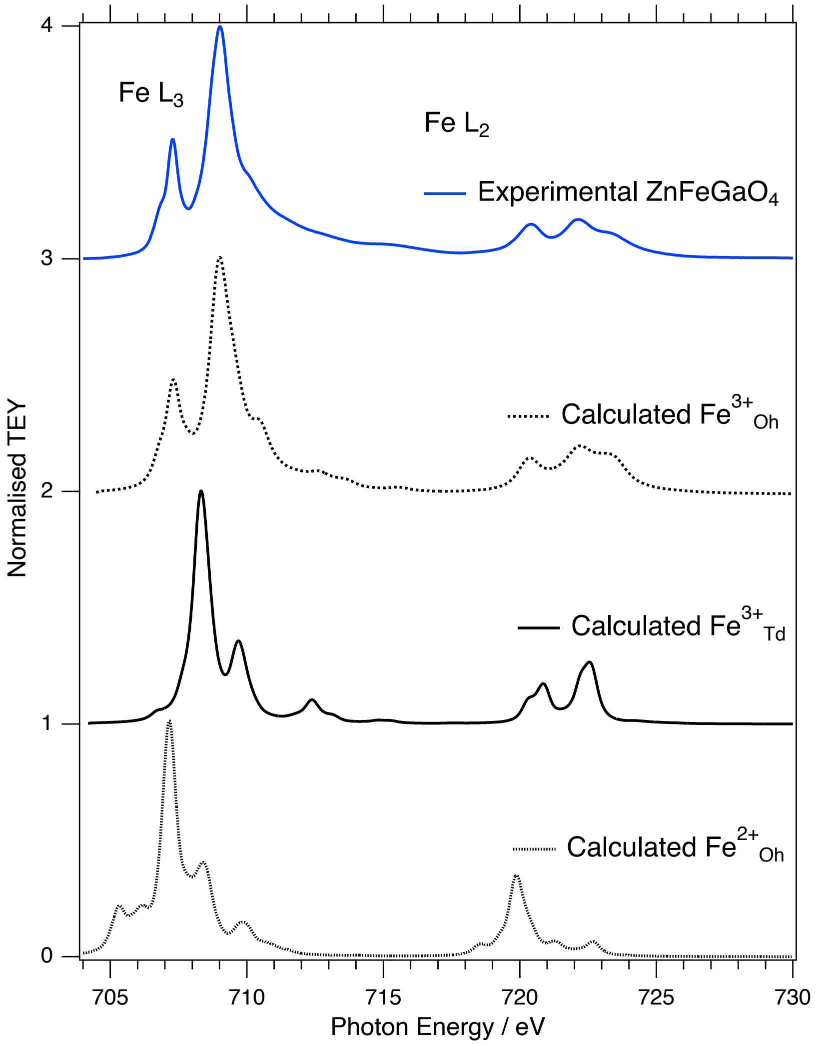

Figure 6.6. Fe $L_{2,3}$ edge NEXAFS spectra of $ZnFeGaO_4$ (blue) and the calculated spectral shape of Fe^{3+} (Oh), Fe^{3+} (Td), and Fe^{2+} (Oh). The calculated spectra have been normalised to the peak maximum and offset in the y-axis for clarity.

The Zn L_3 edges of both $ZnFeGaO_4$ and $ZnGa_2O_4$ measured in TEY mode can be seen in **Figure 6.7**. Similarly to the iron edge, their relative spectral shapes can provide insight into the Zn^{2+} coordination. Due to the closed shell nature of Zn^{2+} (d^{10}), the Oh and Td spectra cannot be calculated using the CTM4XAS software. The spectral features and shape of the $ZnGa_2O_4$ Zn L_3 edge are similar to those observed in ZnO ($Zn^{2+}{}_{Td}$),[315, 316] suggesting a near-normal inversion ($x \approx 0$) in this sample. In the Zn L_3 edge of $ZnFeGaO_4$ the pre-edge feature (**A**) and feature **B** are more prominent compared to $ZnGa_2O_4$, which is attributed to some presence of Zn^{2+}_{Oh}.[317] The relative intensities of **C** and **D** give a qualitative description of the Zn^{2+} coordination, a larger ratio of **C** to **D** indicates more Zn^{2+}_{Td}.[317, 318] The **C:D** ratio observed in $ZnFeGaO_4$ is greater than that of $ZnGa_2O_4$ therefore suggesting there is more Zn^{2+}_{Oh} present in $ZnFeGaO_4$.

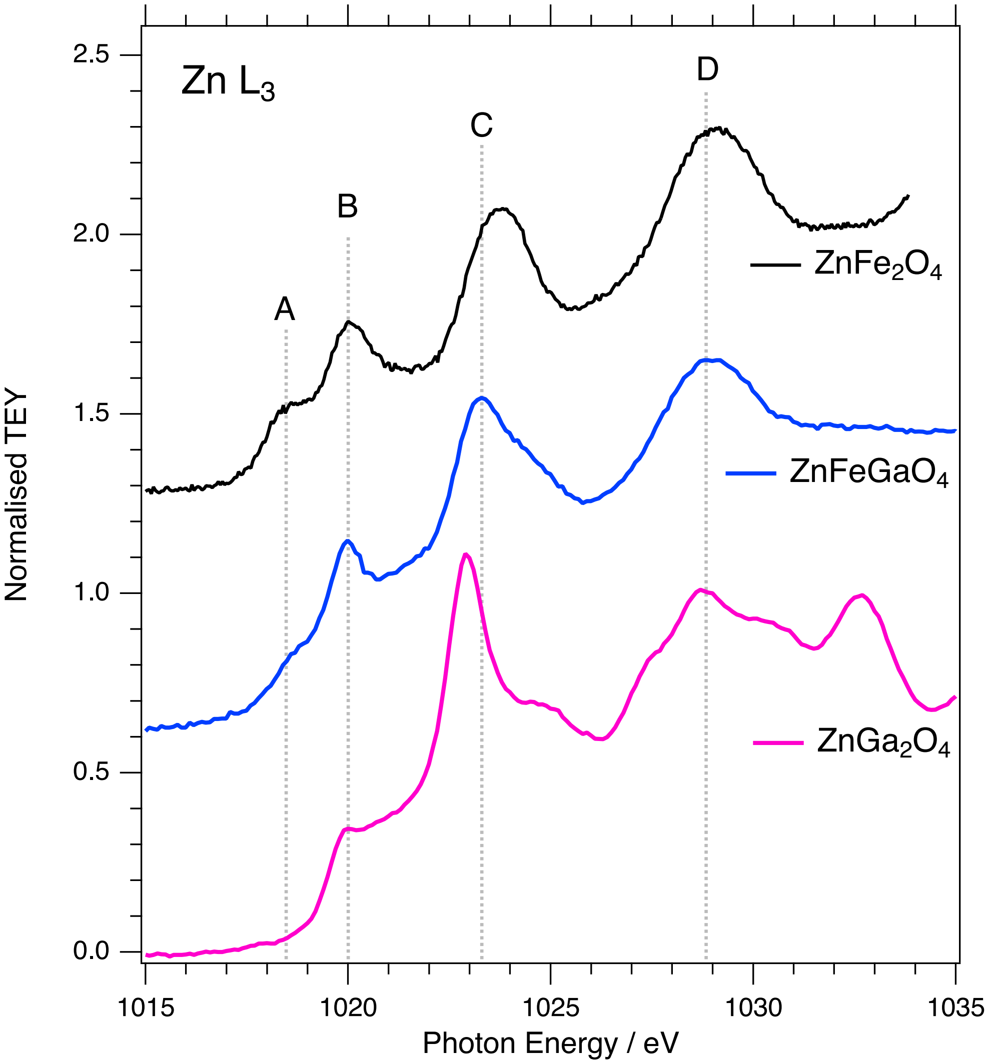

Figure 6.7. Zn L_3 edge NEXAFS spectra of $ZnFe_2O_4$ (black), $ZnFeGaO_4$ (blue), and $ZnGa_2O_4$ (pink).

The spectral features of $ZnFeGaO_4$ show there is some presence of Zn^{2+} in Oh sites. However these Oh features are not as strong as those observed in the Zn L_3 edge of $ZnFe_2O_4$, a nanoparticle sample with a known inversion degree of $x = 0.26$.[135] We can therefore suggest that low levels of cation inversion ($x < 0.26$) occur in $ZnFeGaO_4$. Combining this with evidence of Fe^{3+}_{Oh} found in the Fe $L_{2,3}$ edge (**Figure 6.6**) and the low traces of tetrahedrally coordinated iron determined by PXRD, suggests Ga^{3+} cations preferentially move to the Td sites above the Fe^{3+} cations.

Using DFT simulations we can study the thermodynamics of cation distribution in the spinel oxides. Following the approach of previous work,[260-262] we can calculate the configurational inversion energy for the ternary $ZnGa_2O_4$ system, using the same method as presented in Chapter 4:

$$\Delta E_{\text{conf}}(x) = E(x) - E(0). \tag{14}$$

Using the DFT models with the inversion degrees x = 0, 0.5 and 1, we interpolate the inversion energies using a quadratic dependence.[29] From the interpolated inversion energies (as shown in **Figure 6.8a)**, which are configurational only and independent of temperature, the configurational free energy of inversion (ΔF_{conf}) as a function of temperature (T) can be approximated as:

$$\Delta F_{\text{conf}} = \Delta E_{\text{conf}} - T\Delta S_{\text{conf}} \tag{16}$$

where ΔS_{conf} is the ideal configurational entropy of inversion as is described by the following equation:[29, 263]

$$\Delta S_{\text{conf}} = -R\left[x\ln(x) + (1-x)\ln(1-x) + x\ln\frac{x}{2} + (2-x)\ln\left(1-\frac{x}{2}\right)\right]. \tag{17}$$

Previous work showed that despite the possibility of other contributions to the inversion energy, *e.g.* vibrational contributions, these are relatively small and can be neglected in the first approximation.[261]

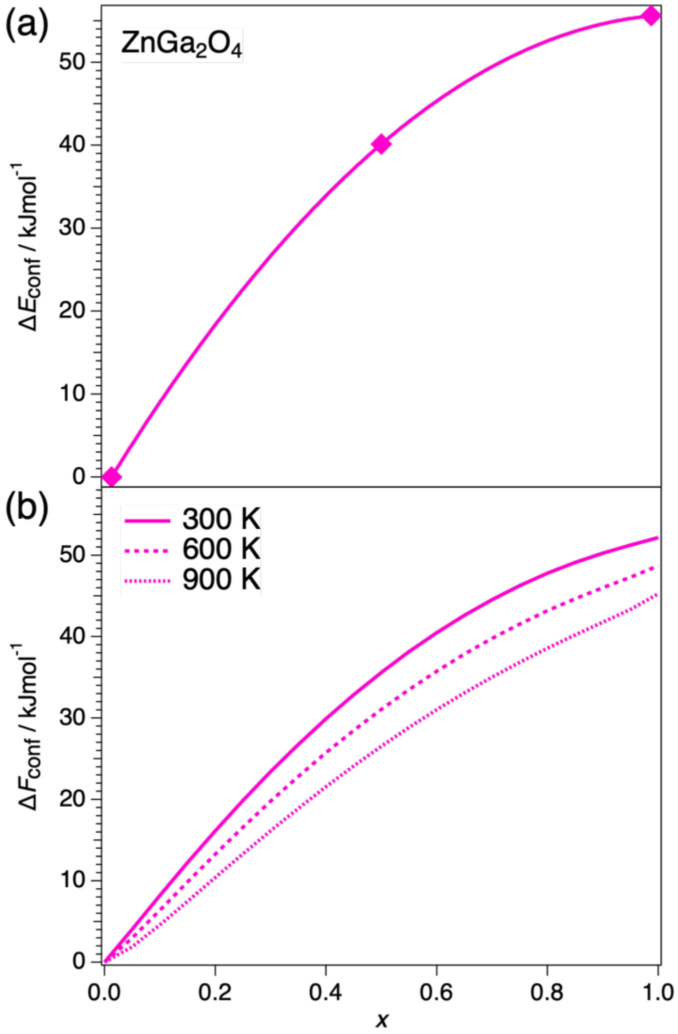

Figure 6.8. (a) inversion energy per formula unit (ΔE_{conf}, configurational contribution only) obtained by DFT, and (b) the configurational free energy (ΔF_{conf}) at 300, 600, and 900 K of $ZnGa_2O_4$.

The most stable configuration of $ZnGa_2O_4$ determined computationally is normal ($x = 0$), with positive inversion energies across the full inversion degree range in **Figure 6.8a**. In a spinel structure containing d^{10} cations, *i.e.* Zn^{2+} and Ga^{3+}, there is no crystal-field stabilisation energy (CFSE) effects, therefore a normal distribution of cations is preferred. By including configurational entropy effects, it allows for the consideration of finite temperatures within the relatively simple model (**Figure 6.8b**). Across a temperature range from 300 to 900 K an inversion degree of $x = 0$ is preferred, which is in good agreement with experimental reports the literature.[125, 129, 130]

In the thermodynamic analysis of $ZnFeGaO_4$, a spinel system with two different B cations (Fe^{3+} and Ga^{3+}), we need to two inversion degrees with respect to both Ga and Fe, which we define as x and y, respectively. The formula of $ZnFeGaO_4$ can be written as $(Zn_{1-x-y}Fe_yGa_x)[Zn_{(x+y)}Fe_{(1-y)}Ga_{(1-x)}]O_4$, in which () and [] represents the Td and Oh sites, respectively. In this case, we need to consider the configurational inversion energy as a function of x and y:

$$\Delta E_{\mathrm{conf}}(x, y) = E(x, y) - E(0) \tag{24}$$

and therefore, affecting how ΔS_{conf} is described:

$$\Delta S_{\mathrm{conf}} = -R \begin{bmatrix} (1 - x - y)\ln(1 - x - y) + x\ln(x) + y\ln(y) + \\ (x + y)\ln\left(\frac{x + y}{2}\right) + (1 - x)\ln\left(\frac{1 - x}{2}\right) + (1 - y)\ln\left(\frac{1 - y}{2}\right) \end{bmatrix}. \tag{25}$$

Figure 6.9 shows contour plots of the configurational free energy of $ZnFeGaO_4$ at 300 K, 600 K and 900 K. Similarly to $ZnGaO_4$, at 300 K a normal distribution of cations, $(Zn)[FeGa]O_4$, is strongly preferred, as Fe^{3+} also has no CFSE. At higher temperatures low levels of inversion become favourable, with the minimum ΔF_{conf} at 900 K corresponding to the configuration $(Zn_{0.93}Fe_{0.07})[Zn_{0.07}Fe_{0.93}Ga_1]O_4$. These calculations suggest that the Fe^{3+} cations will preferentially move to the Td sites, with the Ga^{3+} remaining Oh coordinated.

The DFT-based prediction that the Ga tends to "invert" more than Fe in the $ZnFeGaO_4$ spinel is problematic for several reasons. First, it is in conflict with the experimental spectroscopic results in our own work, shown in **Figure 6.6** and **Figure 6.7**, which suggested that the only iron species present in $ZnFeGaO_4$ is octahedral Fe^{3+}. Second, the consideration of cation sizes supports the preference for Ga^{3+} to move to Td sites over Fe^{3+}: the Td sites are smaller than the Oh sites, therefore the smaller Ga^{3+} cations (0.47 Å) should preferentially sit in the Td sites over the slightly larger Fe^{3+} cation (0.49 Å).[11, 319] Finally, the relative thermodynamic stabilities of the different phases of the pure metal oxides support the stronger preference for Fe in tetrahedral sites vs octahedral sites, in comparison with Ga: the most stable Fe^{3+} oxide polymorph is α-Fe_2O_3 (hematite), which only has octahedral Fe^{3+}, whereas γ-Fe_2O_3 (maghemite), with a mixture of octahedral and tetrahedral Fe^{3+}, has a formation enthalpy 18.1 kJ mol^{-1} higher than that of hematite.[320, 321] On the other side, the most stable gallium oxide polymorph is β-Ga_2O_3, which has a mixture of octahedral and tetrahedral Ga^{3+}, whereas α-Ga_2O_3, with only octahedrally-coordinated cations, has a formation enthalpy 28.9 kJ mol^{-1} higher than that of β-Ga_2O_3.[322] It is therefore sensible to suspect that DFT is getting this trend wrong, and that any cation inversion in the $ZnFeGaO_4$ is due to Ga (not Fe) in the tetrahedral sites.

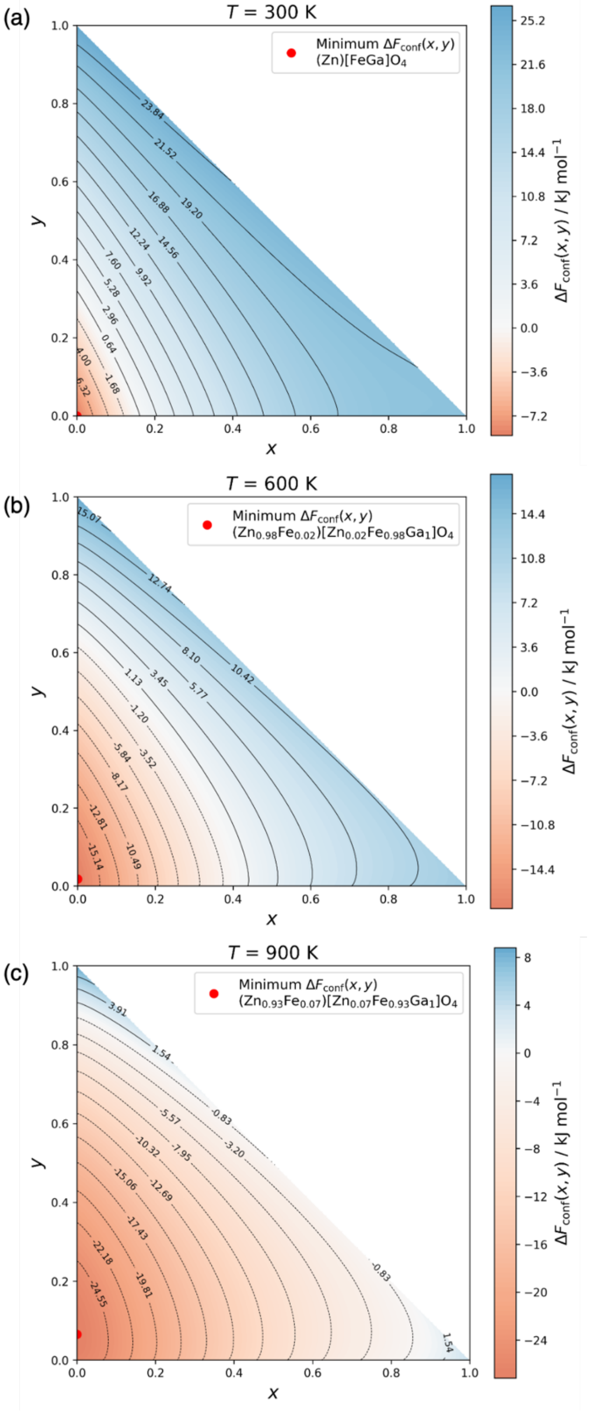

Figure 6.9 Contour plots of the configurational free energy (ΔF_{conf}) of $ZnFeGaO_4$ at (a) 300 K (b) 600 K, and (c) 900 K. The red dot indicates the minimum configuration with the lowest ΔF_{conf}.

The limitations of DFT functionals with respect to the description of transition metal compounds are well reported in the literature, and they often remain even after incorporating Hubbard-type (DFT+U) corrections.[323-325] To investigate these limitations, we calculated the relative energies of the oxides Fe_2O_3, Ga_2O_3, and ZnO in different phases. **Table 6.2** shows the DFT calculated energy of transformation from the Td/Oh phase to the Oh phase of the oxide standards. α-Ga_2O_3 is more stable compared to β-Ga_2O_3, a trend which agrees with experimentally observed enthalpies.[322] Similarly, tetrahedrally coordinated Zn^{2+} is energetically more favourable than octahedral Zn^{2+} in a ZnO structure, respectively. This aligns well with the experimental negative enthalpy of transformation (-23.9 kJ mol^{-1})[326, 327] from the rock salt (Zn^{2+}_{Oh}) to Wurtzite (Zn^{2+}_{Td}) phase of ZnO. The DFT energies predict that maghemite is a more stable configuration of Fe_2O_3 compared to hematite which is contradictory to the experimental observations.[320, 321]

Table 6.2. The experimental transformation enthalpy (ΔH_{expt}) and the DFT calculated energy of transformation per formula unit (ΔE_{DFT}) of the metal oxides Fe_2O_3, Ga_2O_3 and ZnO from the octahedral (Oh) to tetrahedral (Td) phases.

Oxide	Phase Transformation	ΔH_{expt} / kJ mol^{-1}	ΔE_{DFT} / kJ mol^{-1}
Fe_2O_3	Hematite (Oh) to Maghemite (Oh/Td)	18.1	-10.8
Ga_2O_3	α (Oh) to β (Oh/Td)	-28.9	-9.8
ZnO	Rock salt (Oh) to Wurtzite (Td)	-23.9	-24.9

In order to obtain a more accurate computational description of the cation distribution in the spinels we need to apply corrections with respect to the experimental enthalpies of the oxide standards. The method used is based on the following assumptions:

$$E[\text{Metal oxide}_{\text{Oh}}] = E_{\text{DFT}}[\text{Metal oxide}_{\text{Oh}}] \tag{26}$$

$$E\left[\text{Metal oxide}_{\text{Oh/Td}}\right] = E_{\text{DFT}}\left[\text{Metal oxide}_{\text{Oh/Td}}\right] + n_{Td}\Delta E_{\text{M}} \tag{27}$$

where n_{Td} is the number of Fe cations in Td coordination and ΔE_M is correction applied to the relative Td cations in the spinel structures. ΔE_M can then be calculated using the experimental enthalpies of transformation, ΔH, from the Oh to Oh/Td oxides:

$$\Delta E_{\mathrm{M}} = \frac{\Delta H + E_{\mathrm{DFT}}[\text{Metal oxide}_{\mathrm{Oh}}] - E_{\mathrm{DFT}}[\text{Metal oxide}_{\mathrm{Oh/Td}}]}{n_{\mathrm{Td}}}. \qquad (28)$$

The corrections calculated by this method for Fe, Ga and Zn can be seen in **Table 6.3**. For each structure a correction was added corresponding to the type and number of cations in the Td site. For example, for the primitive $ZnGaO_4$ spinel with an inversion degree of $x = 0$ ($2 \times Zn^{2+}{}_{Td}$), a correction of 2.0 kJ mol^{-1} was added.

Table 6.3. Tetrahedral energy corrections (ΔE_M, M = Zn, Fe, Ga) as determined by the DFT energies of metal oxide standards and experimental enthalpies of transformation.[320-322, 326, 327]

Cation M	ΔE_M / kJ mol^{-1}
Zn^{2+}	1.0
Fe^{3+}	38.5
Ga^{3+}	-19.1

The configurational inversion energies and free energies of $ZnGa_2O_4$ with the relative applied corrections can be seen in **Figure 6.10**. The results compared to the uncorrected data (**Figure 6.8**) remain relatively unchanged, with a normal cation distribution still being preferred up to a temperature of 900 K.

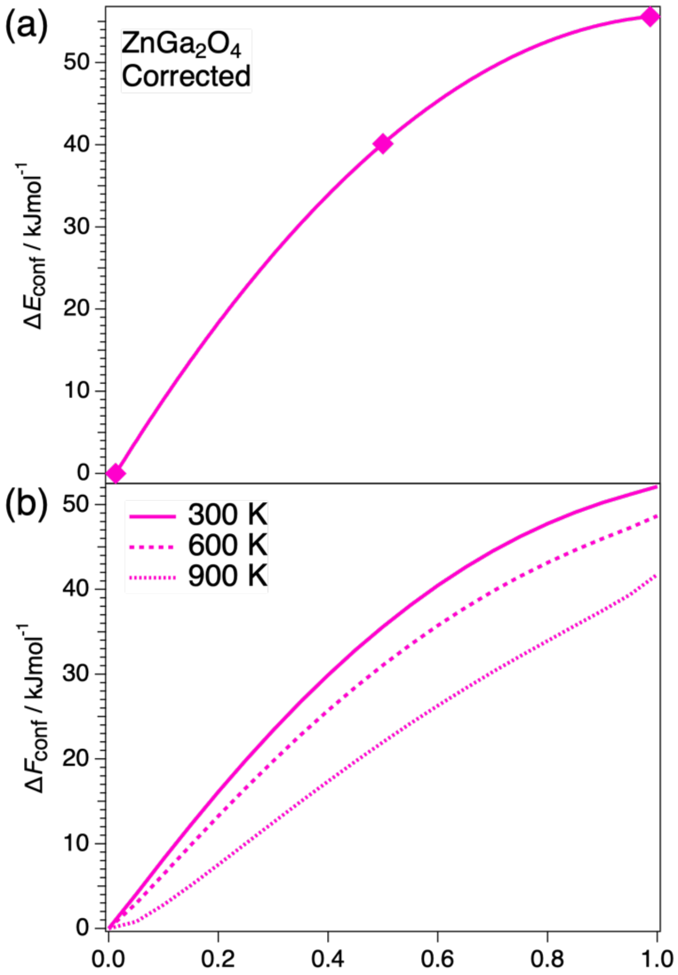

Figure 6.10. (a) inversion energy per formula unit (ΔE_{conf}, configurational contribution only) obtained by DFT with the calculated corrections applied, and (b) the configurational free energy (ΔF_{conf}) at 300, 600, and 900 K of $ZnGa_2O_4$.

The contour plots of the $ZnFeGaO_4$ configurational free energies with the calculated corrections applied are shown in **Figure 6.11**. At low temperatures (300 K), the inversion degree still shows a strong preference for a normal distribution. However, differences in the cation distributions at high temperatures are observed compared to those in **Figure 6.9**. Although the overall inversion degree is still relatively low at 900 K, $(Zn_{0.89}Ga_{0.11})[Zn_{0.11}Fe_1Ga_{0.89}]O_4$, with the corrections applied the Ga^{3+} cations preferentially move to the Td sites over the Fe^{3+} cations. This result aligns well with the NEXAFS and PXRD data of the $ZnFeGaO_4$ nanoparticles.

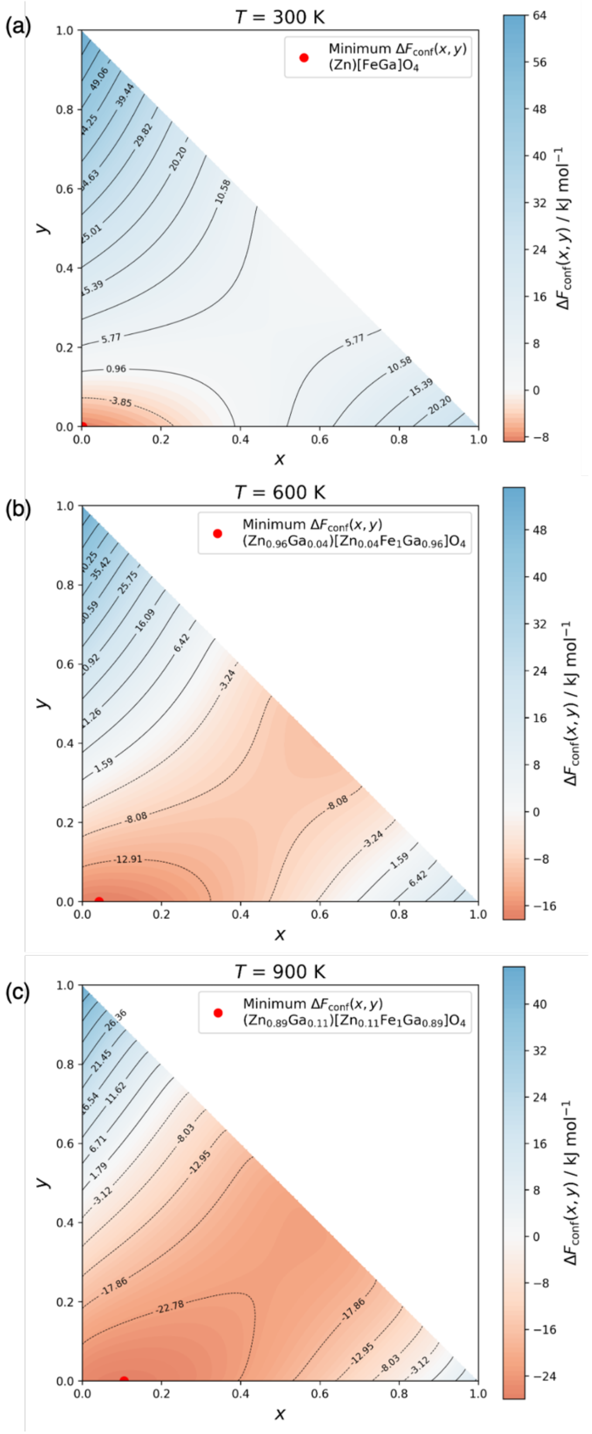

Figure 6.11. Contour plots of the configurational free energy (ΔF_{conf}) of ZnFeGaO$_4$ at (a) 300 K (b) 600 K, and (c) 900 K with the calculated corrections applied. The red dot indicates the minimum configuration with the lowest ΔF_{conf}.

Based on the calculated thermodynamics of cation distribution and the experimental results we can assume an inversion degree of $x = 0$ is suitable to conduct the following analysis. The absolute values of the structural parameters a and u of the nanoparticle samples and those calculated by DFT ($x = 0$) are relatively close, with percentage differences of ~ 1% (**Table 6.1**). The trend in cell parameters is the same in both the experimental and calculated data, *i.e.* $ZnFeGaO_4$ > $ZnGa_2O_4$. The deviation observed between the experimental and calculated structural parameters could be explained by several factors, such as the approximations made when using the GGA+U functional. We also need to consider the temperature difference (room temperature for experimental, 0 K in DFT) and the bulk nature of the DFT calculation, which neglect nanostructuring effects. From the experimental point of view, X-rays have low sensitivity to oxygen atoms; moreover, their scattering signal is masked by the surrounding heaver atoms making the refined u value less reliable.

The calculated electronic structures of the spinels with $x = 0$ can help to rationalise the photocatalytic activity observed in **Figure 6.2**. **Figure 6.12** displays the density of states (DOS) with the cations partial DOS contributions. The transition metal 3d levels provide little contribution to the valence band (VB) for both spinel samples, with O 2p orbitals contributing the most. For $ZnFeGaO_4$, the low-lying Fe 3d levels contribute to the conduction band (CB), resulting in a narrower band gap compared to $ZnGa_2O_4$. The minimum thermodynamic potential required for a photocatalyst for the water splitting process is 1.23 eV,[42, 43] however catalysts with band gap of 2 to 4 eV often demonstrate higher efficiency.[328] The DOS shows that $ZnFeGaO_4$ and $ZnGa_2O_4$ display wide band gaps of 3.35 eV and 4.10 eV, respectively. The trend observed in the band gap widths ($ZnFeGaO_4$ < $ZnGa_2O_4$) is reported in the literature,[110, 129] with $ZnGa_2O_4$ generally having a band gap > 4 eV.[133, 134] Wide band gap catalysts have the advantage of high photochemical stability (*i.e.* low charge carrier recombination rate), however are often limited with respect to their light absorption range.[329]

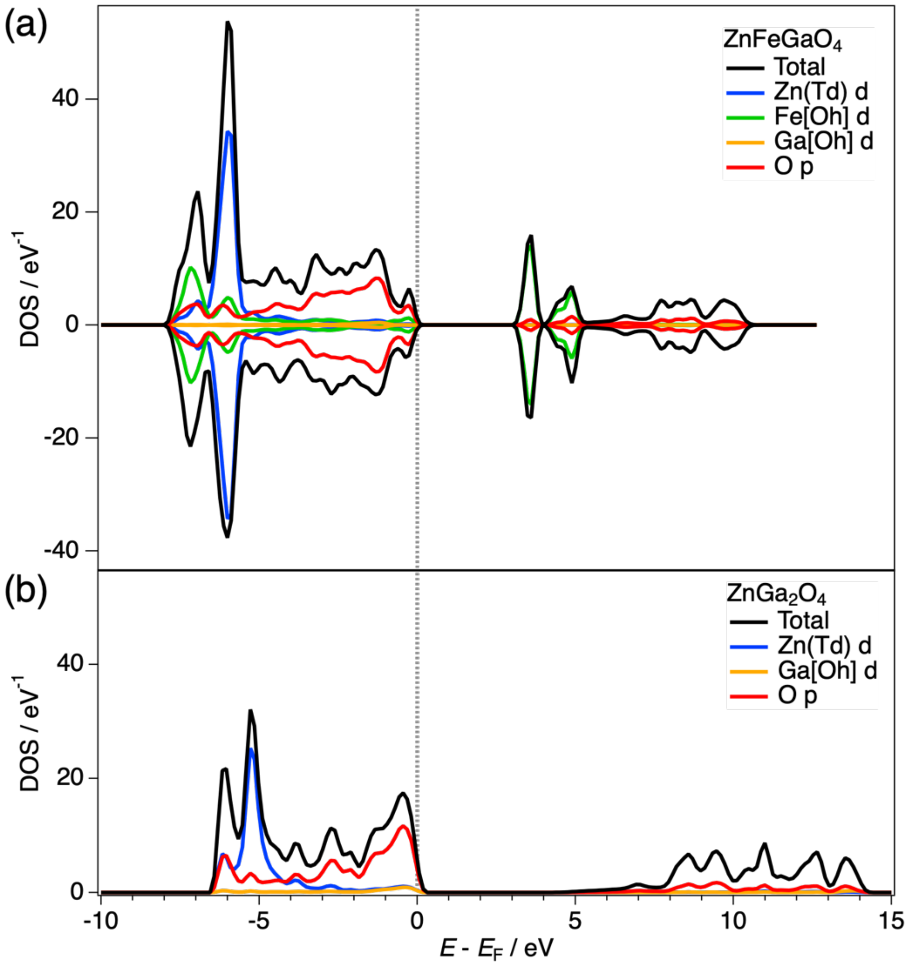

Figure 6.12. Density of states (DOS) at HSE06 level for (a) $ZnFeGaO_4$ and (b) $ZnGa_2O_4$ and partial DOS contributions from Zn, Fe and Ga d orbitals and O p orbitals.

In order for a single-semiconducting material to work as an efficient water splitting photocatalyst, its VB and CB positions must straddle the OER and HER positions as well as having a suitable band gap.[43] The CB minimum and VB maximum have been determined by the bulk DFT simulations, however these are calculated with respect to the average electron potential in the solid. The electronic structure needs to be aligned relative to the vacuum level to compare with the relative half reaction potentials. Slab calculations are used to determine the potential difference (ΔV) between the pseudo-bulk average and the vacuum potential. A stoichiometric slab of $ZnFeGaO_4$ with a symmetric (100) terminated surface and vacuum level can be seen in **Figure 6.13**. The same process was repeated for $ZnGa_2O_4$.

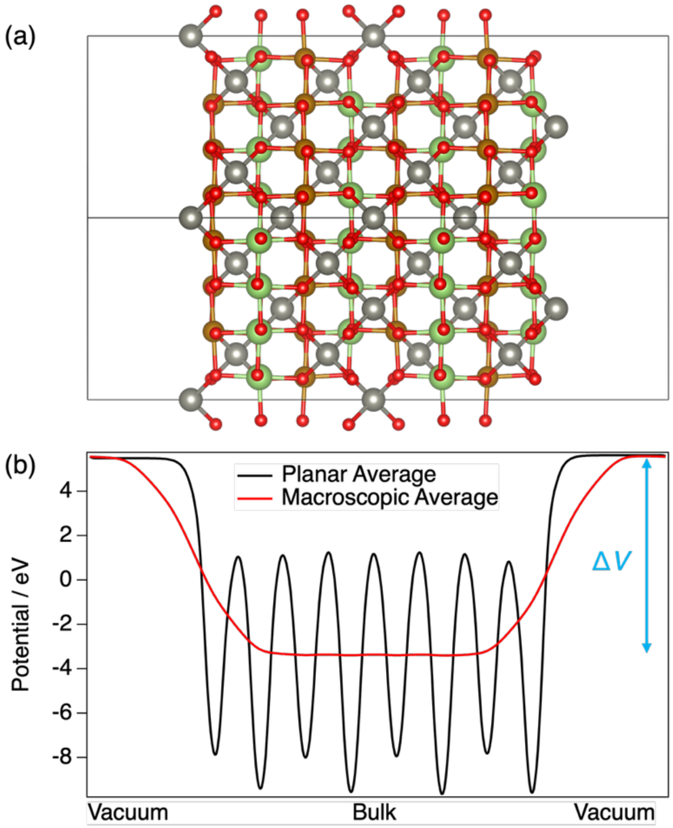

Figure 6.13. (a) $ZnFeGaO_4$ slab with a (100) termination (colour scheme: Zn = silver; Fe = gold; Ga = green; O = red) and (b) the planar averages of the electrostatic potential.

The presence of two B cations and their distribution in the $ZnFeGaO_4$ structure does create more complexity when building a symmetric slab. The two surfaces presented in the slab model in **Figure 6.12a** are not completely symmetrical, on one side there is a Fe^{3+} sub-surface layer and on the other side a Ga^{3+} sub-surface layer. However, as both Fe^{3+} and Ga^{3+} are trivalent cations the dipole moment created is negligible and can be easily corrected using dipole corrections implemented in the VASP code. The resulting potential in **Figure 6.12b** is not exactly symmetrical, however is suitable for defining the vacuum level. Even in complex systems with multiple A or B cations, the DFT calculations can provide a reliable band alignment.

Figure 6.13 shows the calculated band alignments of $ZnFeGaO_4$ and $ZnGa_2O_4$ relative to the vacuum scale compared with the water splitting half-reaction potentials. At pH = 7 and at room temperature the HER and OER potentials are -4.03 and -5.25 eV, respectively. Both $ZnFeGaO_4$ and $ZnGa_2O_4$ display a suitable band alignment with their VB maxima sitting below the OER potential with respect to the OER potential (-5.25 eV). The lack of oxygen evolution of $ZnGa_2O_4$ in **Figure 6.3** can be explained by its large band gap, reducing the number of photons absorbed.

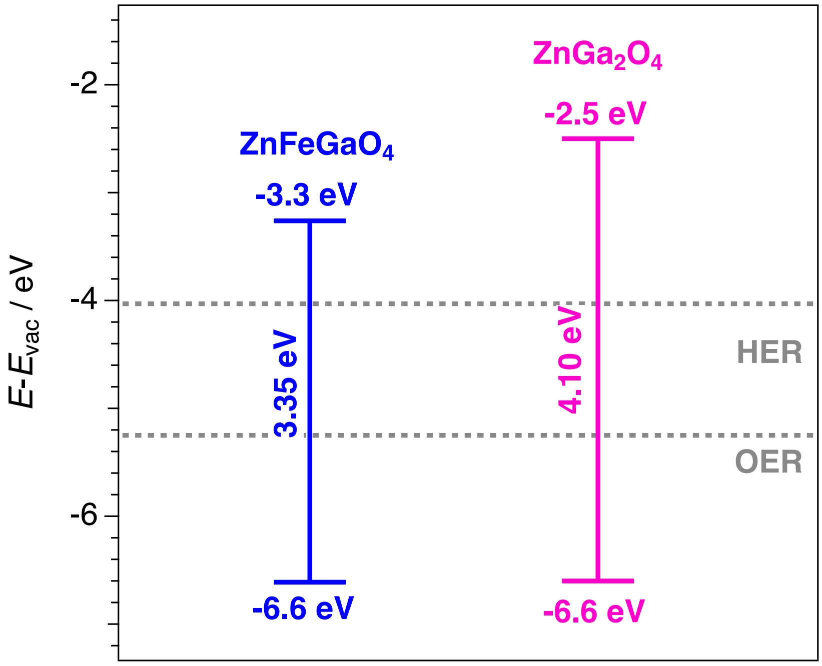

Figure 6.13. Calculated CB and VB positions and band gaps of $ZnFeGaO_4$ and $ZnGa_2O_4$. Half-reaction potentials for water splitting are represented by dotted lines.

The electronic structures and band alignments presented in this work are calculated from the spinels in a normal distribution and does not consider the partial inversion that may be present in the nanoparticle samples, particularly in $ZnFeGaO_4$. It is known that cation distribution can influence the electronic structure of spinels,[260, 261] therefore the effect of an inversion degree of $x < 0.5$ (an inversion level that thermodynamically could occur based on DFT predictions) on the electronic structure is an area that requires further attention.

6.4 Chapter Conclusions

Using a combination of theoretical and experimental techniques we have been able to study the structure, photocatalytic behaviour and electronic properties of $ZnFeGaO_4$ and $ZnGa_2O_4$ nanoparticle samples. $ZnFeGaO_4$ was the only sample that demonstrated photocatalytic activity for the OER, generating 120 μmol g^{-1} of oxygen under UV irradiation over a 5-hour period. This is an improvement on the oxygen evolution by $ZnFe_2O_4$ (65 120 μmol g^{-1}). To further understand the catalytic properties, we first investigated the spinels relative structures. PXRD showed that < 1% of the Td sites are occupied by Fe, however the technique is limited with respect to determining overall cation distribution. The NEXAFS spectra of $ZnFeGaO_4$ demonstrated low Zn^{2+} inversion and confirmed the presence of only Fe^{3+}_{Oh}, therefore some Ga^{3+} cations are in Td sites.

The DFT simulations predict a normal cation distribution of $ZnGa_2O_4$ at temperatures of up to 900 K. However, $ZnFeGaO_4$ showed inversion with a preference for Fe^{3+} to move to Td sites over Ga^{3+}, contradicting the experimental evidence. To overcome DFT's limitations in defining transition metals, a Td site correction was calculated using experimental enthalpies of formation and DFT energies of the Td/Oh phases of ZnO, Fe_2O_3 and Ga_2O_3. After applying the corrections, an $ZnFeGaO_4$ inversion degree of $x = 0.11$ with Ga^{3+} preferentially moving to the Td sites was established. This work has shown that corrections must be considered when computationally studying spinel systems.

Based on the thermodynamic simulations an inversion degree of $x = 0$ was assumed for the electronic structure calculations. Both spinels displayed a suitable band alignment for the OER, however $ZnGa_2O_4$ has a wide band gap of > 4 eV which could limit the photons absorbed, explaining the lack of O_2 produced. This work has demonstrated the potential influence of B cation substitution on spinels photocatalytic ability. Further work should continue to investigate how different ratios of Fe^{3+} and Ga^{3+} can influence the electronic structure and photocatalytic properties of the mixed B cation system.

7. Conclusions and Future Work

7.1 General Conclusions from the Thesis

This PhD project set out with the aim to characterise transition-metal spinel oxide structures and investigate their photocatalytic properties with respect to the water splitting process. As outlined in the thesis introduction, there are three key strategies to modify the electronic structure and photocatalytic properties of spinel ferrites: (i) A cation substitution, (ii) B cation substitution, and (iii) tuning the degree of inversion without changing composition. A comprehensive understanding of their structural and configurational properties is essential for determining the best method of enhancing their photocatalytic efficiency.

Chapters 4 and 6 focused on A and B cation substitution in spinel ferrites, respectively. Substituting Co, Cu, and Zn cations into the spinel AFe_2O_4 resulted in significant differences in cation distribution, electronic structure, and photocatalytic activity. Among the AFe_2O_4 ferrites, $ZnFe_2O_4$ exhibited significantly more activity for the oxygen evolution reaction (OER) compared to $CoFe_2O_4$ and $CuFe_2O_4$. Although all three spinels displayed suitable band gaps for the OER process, the enhanced activity of zinc ferrite is rationalised by its favourable band alignment as calculated by density functional theory (DFT). This demonstrated the importance of A cation selection when designing an efficient photocatalyst.

Our calculations also help rationalised the cation distributions in these spinels. Cobalt and copper ferrite exhibited high bulk inversion degrees of x = 0.81 and 0.91, respectively (as determined by X-ray diffraction techniques), whereas $ZnFe_2O_4$ displayed a lower inversion degree of x = 0.26. These trends align with both results reported in the literature [10, 12, 102, 125] and inversion preferences predicted by DFT, *i.e.* $CoFe_2O_4$ and $CuFe_2O_4$ are inverse structures, and $ZnFe_2O_4$ prefers a normal configuration. The primary influence on the high inversions of cobalt and copper ferrite is their crystal-field stabilisation energies (CFSE), whereas the low inversion displayed by $ZnFe_2O_4$ is driven by electrostatic stabilisation and the strong sp^3 hybridisation of Zn^{2+} in Td sites.

Despite the important roles of both the bulk and surface in photocatalytic materials, the study of the difference between the bulk and surface of spinels is relatively underdeveloped. Significant deviation in the cation inversions measured by bulk diffraction techniques and surface-sensitive X-ray absorption spectroscopy (XAS) were observed in the nanoparticles. The cation distribution of cobalt and copper ferrite demonstrated a high inversion degree in the bulk compared to the surface, where ~75% of the near-surface Td sites were occupied by Fe cations. In contrast, an increase from 26% of Fe in Td in the bulk to 52% at the surface was observed in $ZnFe_2O_4$. Evidence of Fe^{2+} Oh was also seen in the XAS spectra. To provide a deeper understanding of the surface influence we conducted DFT simulations on different terminations of zinc ferrite, the spinel ferrite that showed the greatest bulk/surface inversion difference (and also the most promise as a photocatalyst for the OER). These calculations proved that cation inversion at the surface of $ZnFe_2O_4$ is energetically favourable, with an increase stability as it propagates into the sub-surface layers. A more in-depth study of surface effects would need to consider surface defects, such oxygen vacancies. However, the simulations presented here establish a framework for future surface studies.

To further explore the surface effects of zinc ferrite, we conducted studies on a zinc ferrite single-crystal with a known pristine bulk structure (*i.e.* $x \approx 0$). Chapter 5 presents the influence of the preparation method on the surface structure of a (111) terminated $ZnFe_2O_4$ single-crystal. A combination of surface sensitive spectroscopy and imaging measurements revealed that annealing the sample under ultra-high vacuum (UHV) conditions removes Zn from the surface, leaving an iron-rich magnetite-like surface structure. However, annealing under O_2 preserved the stoichiometric zinc ferrite surface structure. The Fe $L_{2,3}$ edge of the $ZnFe_2O_4$ (111) O_2 annealed crystal are comparable to that of the nanoparticle sample measured in Chapter 4, suggesting similar surface structures. Temperature dependent X-ray photoelectron spectroscopy (XPS) measurements demonstrated a significant loss of Zn from the surface at temperatures ≥ 500 °C under UHV. However, at temperatures of up to 600 °C, there was no zinc sublimation seen when the sample was annealed under O_2. DFT simulations found that the transformation from zinc ferrite to magnetite is thermodynamically favourable under UHV at temperatures of ~ 500 °C. However, under an oxygen partial pressure comparable to the experimental conditions, the transformation is not favourable in the temperature range accessible by the experiment. Typically, the preparation and experimental analysis of single-crystal model catalysts are conducted under UHV, but this work highlights the dramatic effects that UHV treatment can have on the surface of these materials. In future work, this must be considered when studying photocatalytic activity as the surface plays a crucial role.

Having established zinc ferrite as an active photocatalyst for the OER, Chapter 6 investigated the effect of substituting the Fe^{3+} (B) cation with Ga^{3+}, a method of improving efficiency that had been reported in the literature.[125, 129] The structural properties and catalytic activity of $ZnFeGaO_4$ and $ZnGa_2O_4$ nanoparticle samples were investigated. Compared to $ZnFe_2O_4$, the mixed $ZnFeGaO_4$ spinel exhibited an improvement in the OER, producing almost double the amount of O_2. Despite both the Ga-based spinels having a favourable band alignment for the OER, $ZnGa_2O_4$ displayed no activity, which was attributed to its wide band gap (> 4 eV). A full comparison of the oxygen evolution of the spinel nanoparticles studied can be seen in **Table 7.1**.

Table 7.1. A summary of the photocatalytic oxygen evolution of the spinels studied over a time of 5 hours under simulated sun light using $AgNO_3$ as an electron sacrificial agent.

Catalyst	O_2 evolution over 5 hours / µmol g^{-1}
$CoFe_2O_4$	0.2
$CuFe_2O_4$	2.5
$ZnFe_2O_4$	65
$ZnFeGaO_4$	120
$ZnGa_2O_4$	1.7

Characterising the cation distribution in the quaternary spinel presented a more complex challenge compared to the ternary spinels, as the inversion with respect to two independent cations needs to be considered. The simulations also highlighted limitations in DFT when defining transition metals. By using a combination of experimental and DFT calculated energies of transformation of metal oxide standards, we were able to design a correction to the relative energies with respect to the Td/Oh site occupancy. The corrected DFT studies showed that in $ZnGa_2O_4$ and $ZnFeGaO_4$ a normal cation distribution ($x = 0$) is thermodynamically favourable. However, at high temperatures of 900 K, some low but finite levels of inversion become favourable, with Ga^{3+} preferentially moving to the Td sites. This aligns well with the experimental Fe $L_{2,3}$ and Zn L_3 near-edge X-ray absorption fine structure (NEXAFS) edges and powder X-ray diffraction (PXRD) data, which showed that there are low levels of Zn^{2+} in Oh sites with all the Fe^{3+} remaining in Oh sites, and that therefore some Ga^{3+} must be in Td sites. Like in zinc ferrite, in the absence of CFSE, the preference for a low inversion degree in $ZnFeGaO_4$ and $ZnGa_2O_4$ is driven by electrostatic stabilisation and Zn bonding. The preference for Ga^{3+} to move to Td sites over Fe^{3+} could be due to the size effects, with the ionic radii of Ga^{3+} (0.47 Å) in Td coordination being smaller than Fe^{3+} (0.49 Å).

Overall, the work conducted throughout this PhD has highlighted the profound influence of cation substitution on spinels electronic and catalytic properties, with $ZnFeGaO_4$ being the most efficient catalyst among those considered in this thesis. It also emphasises the importance of characterising not only the bulk but also surface structures of the spinels. These insights provide a strong foundation for the design of novel spinel-based photocatalysts for the water splitting reaction.

7.2 Future Work

The compositional diversity and tuneable cation distribution of spinels presents a wide range of research opportunities, with a only a few spinel structures and their potential applications presented across the thesis. In this section suggestions for future work and the potential expansion of the project will be discussed. Some preliminary results will be presented and how, given more time, they would be utilised and improved upon. Also, some of the (many!) challenges encountered during this project and how these could be overcome will be discussed.

A full understanding of the cation inversion is a fundamental part of the study of spinels which depending on the cations in the spinel structure can be challenging. In Chapter 4, the use of anomalous X-ray scattering (AXRS) is required to determine the inversion degree of $CoFe_2O_4$, due to the similar atomic numbers of the Co and Fe. In the cases of $ZnFeGaO_4$ and $ZnGa_2O_4$, AXRS is also required to determine full pictures of their cation distribution. However, due to limited access to beamlines that can conduct such experiments, we were unable to obtain this data; it would be useful to perform those experiments in the future.

In Chapters 4 and 5 the calculated electronic structures were conducted under the assumption the spinels are normal ($ZnFe_2O_4$, $ZnFeGaO_4$ and $ZnGa_2O_4$) or fully inverse ($CoFe_2O_4$ and $CuFe_2O_4$). In reality the nanoparticles display some deviation from the extreme inversions used in the calculations ($x = 0$ or 1). To improve on the accuracy of the band gaps and alignments with respect to the experimental samples the exact inversion degree needs to be modelled. To model specific a cation distribution requires the use of a larger cell, which not only increases computational cost but also the complexity of the models. In the conventional unit cell (**Figure 1.1a**) of a ternary spinel there are 4222 possible configurations, and this would significantly increase considering a quaternary spinel, such as $ZnFeGaO_4$. The importance of the cation configuration with respect to a specific x has been demonstrated by Hou *et al.*[9] who conducted a computational analysis of $CoFe_2O_4$. They found that the $Co^{2+}{}_{Oh}$ cations had a preference to be far away from other $Co^{2+}{}_{Oh}$ cations and $Co^{2+}{}_{Td}$.

In an attempt to study the configurations in the conventional unit cells of the spinel oxides, we conducted some cluster expansion simulations using the MedeA[330] UNCLE (UNiversal Cluster Expansion) software.[331, 332] **Figure 7.1a** shows the binary state diagram of the $ZnGa_2O_4$ spinel, where the ground state energy of 33 configurations with varying x was predicted using a DFT (VASP) training set.

From cluster expansion, we went on to complete a Monte Carlo simulation to predict how the inversion degree changes as a function of temperature. In theory, this method should provide a more accurate prediction compared to the three-point method presented in **Figure 4.4** and **Figure 6.9,** in Chapters 4 and 6, respectively. **Figure 7.1b** demonstrates that a normal configuration is favourable until temperatures of above 800 K are reached. However even at high temperatures up to 1500 K a very low inversion degree ($x = 0.12$) is predicted.

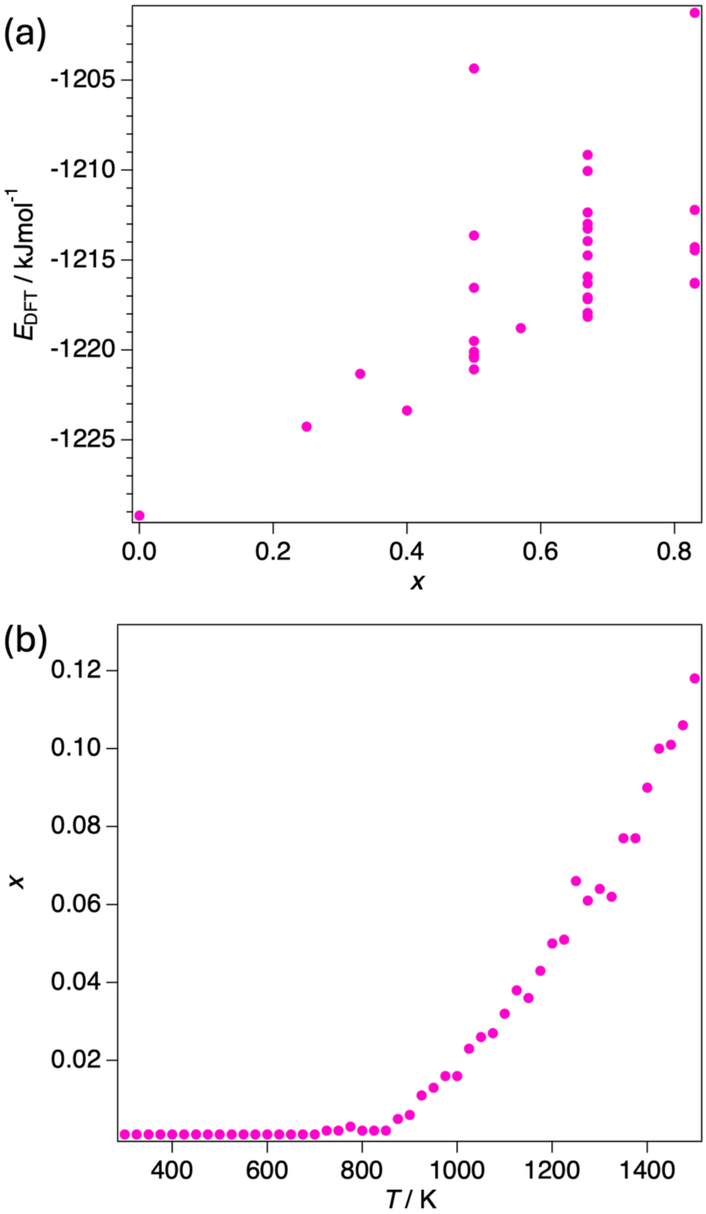

Figure 7.1. (a) The binary state diagram of the cluster expansion and (b) the inversion degree of $ZnGa_2O_4$ as a function of temperature by Monte Carlo simulations.

Despite good initial results for the $ZnGa_2O_4$ system, we encountered some issues in increasing dataset size and studying other spinels. Predicting only 33 structures came at a significant computational cost, therefore studying a larger data set would require greater computational power and time. The MedeA software was unable to include magnetism in the cluster expansion simulations, which resulted in poor representation of the modelled spinel ferrites. MedeA was also limited with respect to studying the spinel $ZnFeGaO_4$, which not only exhibits magnetism but also requires the consideration of two B cations. From these preliminary calculations we established a foundation for studying larger cells. To further the studies of the spinel inversion degrees we would either need to use more advanced cluster expansion software, or conduct a machine learning based approach, similar to that reported by Sánchez-Palencia *et al.*[333]

The third strategy of modifying the spinels properties, *i.e.* tuning the inversion degree, was briefly explored during the PhD project. Preliminary measurements investigated a series of $CoFe_2O_4$ nanoparticles prepared by the coprecipitation method in a range of temperatures (80, 450, 900 and 950 °C). The nanoparticle size and structural parameters of these samples as determined by AXRS are presented in **Table 7.2**.

Table 7.2. Summary of experimentally determined particle size and structural parameters *a* (cell parameters), *x* (inversion degree), and R_{wp} (weighted profile R-factor) of $CoFe_2O_4$ prepared at increasing temperature (*T*) by AXRS.

T / °C	Size / nm	a / Å	x	R_{wp} / %
80	16(1)	8.372(2)	0.87(1)	2.37
450	36(1)	8.399(2)	0.59(1)	1.90
900	83(1)	8.392(3)	0.77(1)	2.89
950	295(2)	8.341(5)	0.72(2)	4.90

With increasing preparation temperature, the particle size increased from 16 nm (80 °C) to 295 nm (950 °C). The trend of increasing particle size with increasing annealing temperature has been observed in the literature for cobalt ferrite nanoparticles.[334, 335] The temperature controlled growth of spinels nanoparticles can be attributed to either solid state diffusion or Ostwald Ripening.[336] An overall decrease in inversion degree was also observed with increasing temperature, with $x = 0.87$ at 80°C and $x = 0.72$ at 950 °C. However, at 450 °C a very low value of $x = 0.59$ is observed. To understand this anomalous result, we would need to conduct more sample characterisation, *e.g.* XAS. Initial neutron diffraction measurements conducted at the ISIS Neutron and Muon source showed the same trend of decreasing x and increasing particle size in $CoFe_2O_4$ nanoparticles with increasing temperature. Although both x and size are effected by temperature, Carta *et al.*[77] report that the inversion degree is not dependent on the particle size, suggesting x is mainly influenced by the thermodynamics of cation distribution.[26, 27] When discussing the photocatalytic activity of spinel samples both size and the cation distribution need to be considered. Firstly, smaller nanoparticles have a larger surface area to volume ratio, leading to more available active sites for the photocatalytic process.[240, 337, 338] Secondly, the particle size can influence the electronic properties of metal oxide materials,[339-341] for example Singh *et al.*[342] report an increase in the band gap of $ZnFe_2O_4$ with decreasing particle size from 60 – 10 nm. However, as demonstrated by some initial DFT calculations, the band gap is also influenced by changes in the bulk inversion degree (independent of size effects). **Table 7.3** shows the DFT calculated band gaps of $ZnFe_2O_4$ with inversion degrees of $x = 0$, 0.5 or 1.

Table 7.3. DFT calculated band gaps of $ZnFe_2O_4$ with a varied inversion degree.

x	Band Gap / eV
0	2.84
0.5	2.67
1	2.56

To continue this work we would aim to conduct similar studies of photocatalytic activity but with respect to a changing inversion degree. We would start with a sample, such as $ZnFe_2O_4$ or $ZnFeGaO_4$ which has already demonstrated activity and force changes in the inversion degree with thermal treatment.

Another area of research that we would like to develop on is the interaction of water with the spinel ferrite surfaces. On the B07-B and -C beamlines, we attempted to study how the distribution and oxidation states of the surface cation changes upon interaction with water and UV light. Initially we introduced a water pressure of a few mbar to the experimental chamber, but only gas phase water was observed, and no liquid layers condensed on the surface. We therefore attempted to cool the samples down to create a liquid water layer using a Peltier cooler. Although we were able to briefly obtain a liquid layer on the sample surface (similar to that shown in **Figure 7.2**), the instability of the cooling system either resulted in ice being formed or the evaporation of the water from the surface.

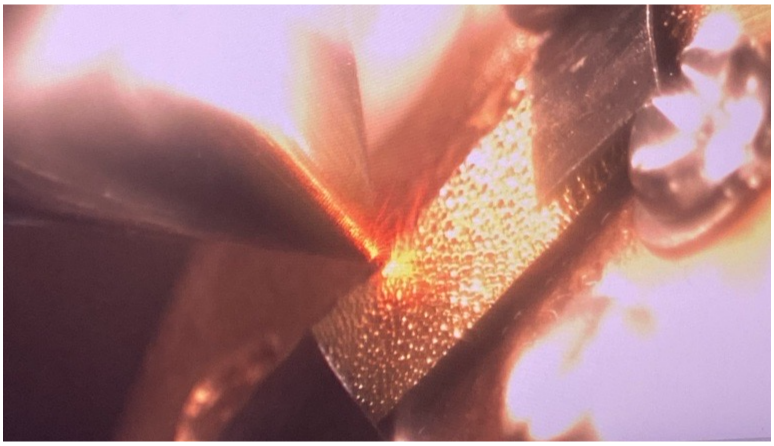

Figure 7.2. An example of a liquid water layer created on the surface of a gold coated silicon wafer.

To overcome this challenge, we would use the electrochemical cell on B07 to recreate the experimental conditions of the catalysis measurements (*i.e.* with sacrificial agents, water and UV light). We would therefore be able to study *in-situ* the effect of the catalysis process on the spinel samples by XPS and NEXAFS while monitoring the O_2 evolved. We would ideally parallel this experimental research with DFT simulations of the interaction of water with the spinel surfaces. As mentioned in Chapter 4, this would require more advanced surface modelling, taking into consideration surface defects.

As presented here, there are several immediate avenues for extending this research to further clarify the structural and photocatalytic behaviour of these spinels. Beyond the specific systems presented in this thesis, a broad range of spinel compositions, with many options for possible A and B cations, remain open for investigation. It is our hope that the collaborative experimental and theoretical approach developed throughout this project can help in future studies into the design and optimisation of spinel photocatalysts.

References

1. S. Nishikawa, *Ann. D. Phys.*, 1915, **8**, 199-209.

2. W. H. Bragg, *The London, Edinburgh, and Dublin Philosophical Magazine and Journal of Science*, 1915, **30**, 305-315.

3. V. Tsurkan, H.-A. Krug von Nidda, J. Deisenhofer, P. Lunkenheimer and A. Loidl, *Physics Reports*, 2021, **926**, 1-86.

4. K. E. Sickafus, J. M. Wills and N. W. Grimes, *J. Am. Ceram. Soc.*, 1999, **12**, 3279-3292.

5. K. Momma and F. Izumi, *Journal of Applied Crystallography*, 2011, **44**, 1272-1276.

6. T. Tatarchuk, B. Al-Najar, M. Bououdina and M. A. A. Ahmed, *Catalytic and Photocatalytic Properties of Oxide Spinels*, Springer, Cham, 2018.

7. K. Bouferrache, Z. Charifi, H. Baaziz, A. M. Alsaad and A. Telfah, *Semiconductor Science and Technology*, 2020, **35**, 095013.

8. H. Perron, T. Mellier, C. Domain, J. Roques, E. Simoni, R. Drot and H. Catalette, *Journal of Physics: Condensed Matter*, 2007, **19**, 346219.

9. Y. H. Hou, Y. J. Zhao, Z. W. Liu, H. Y. Yu, X. C. Zhong, W. Q. Qiu, D. C. Zeng and L. S. Wen, *Journal of Physics D: Applied Physics*, 2010, **43**, 445003.

10. J. Venturini, A. M. Tonelli, T. B. Wermuth, R. Y. S. Zampiva, S. Arcaro, A. Da Cas Viegas and C. P. Bergmann, *Journal of Magnetism and Magnetic Materials*, 2019, **482**, 1-8.

11. R. D. Shannon, *Acta Cryst.*, 1976, **32**, 751-767.

12. J. R. Sandemann, K. A. H. Stockler, X. Wang, B. C. Chakoumakos and B. B. Iversen, *J. Am. Chem. Soc.*, 2023, **145**, 21053-21065.

13. T. Dudev and C. Lim, *J. Am. Chem. Soc.*, 2000, **122**, 11146-11153.

14. K. A. M. Khalaf, *Solid State Communications*, 2021, **324**, 114134.

15. L. Rulíšek and J. Vondrášek, *Journal of Inorganic Biochemistry*, 1998, **71**, 115-127.

16. H. S. C. O'Neill and A. Navrotsky, *American Mineralogist*, 1983, **68**, 181-194.

17. E. J. W. Verwey and E. L. Heilmann, *The Journal of Chemical Physics*, 1947, **15**, 174-180.

18. J. D. Dunitz and L. E. Orgel, *Journal of Physics and Chemistry of Solids*, 1957, **3**, 318-323.

19. J. D. Dunitz and L. E. Orgel, *Journal of Physics and Chemistry of Solids*, 1957, **3**, 20-29.

20. D. S. McClure, *Journal of Physics and Chemistry of Solids*, 1957, **3**, 311-317.

21. K. R. Sanchez-Lievanos, J. L. Stair and K. E. Knowles, *Inorg. Chem.*, 2021, **60**, 4291-4305.

22. Q. Zhao, Z. Yan, C. Chen and J. Chen, *Chem. Rev.*, 2017, **117**, 10121-10211.

23. Z. Zi, Y. Sun, X. Zhu, Z. Yang, J. Dai and W. Song, *Journal of Magnetism and Magnetic Materials*, 2009, **321**, 1251-1255.

24. A. L. Tiano, G. C. Papaefthymiou, C. S. Lewis, J. Han, C. Zhang, Q. Li, C. Shi, A. M. M. Abeykoon, S. J. L. Billinge, E. Stach, J. Thomas, K. Guerrero, P. Munayco, J. Munayco, R. B. Scorzelli, P. Burnham, A. J. Viescas and S. S. Wong, *Chemistry of Materials*, 2015, **27**, 3572-3592.

25. K. Vamvakidis, M. Katsikini, D. Sakellari, E. C. Paloura, O. Kalogirou and C. Dendrinou-Samara, *Dalton Trans.*, 2014, **43**, 12754-12765.

26. L. Néel, *J. Phys. Radium*, 1950, **11**, 49-61.

27. J. S. Smart, *Physical Review*, 1954, **94**, 847-850.

28. H. B. Callen, S. E. Harrison and C. J. Kriessman, *Physical Review*, 1956, **103**, 851-856.

29. A. Navrotsky and O. J. Kleppa, *J. Inorg. Nucl. Chem.*, 1967, **29**, 2701-2714.

30. L. I. Granone, R. Dillert, P. Heitjans and D. W. Bahnemann, *Chemistry Select*, 2019, **4**, 1232-1239.

31. L. I. Granone, A. C. Ulpe, L. Robben, S. Klimke, M. Jahns, F. Renz, T. M. Gesing, T. Bredow, R. Dillert and D. W. Bahnemann, *Phys. Chem. Chem. Phys.*, 2018, **20**, 28267-28278.

32. F. Bræstrup, B. C. Hauback and K. K. Hansen, *Journal of Solid State Chemistry*, 2008, **181**, 2364-2369.

33. H. S. C. O'Neill and W. A. Dollase, *Phys. Chem. Minerals*, 1994, **20**, 541-555.

34. R. Zapukhlyak, M. Hodlevsky, V. Boychuk, J. Mazurenko, V. Kotsyubynsky, L. Turovska, B. Rachiy and S. Fedorchenko, *Journal of Magnetism and Magnetic Materials*, 2023, **587**, 171208.

35. M. R. De Guire, R. C. O'Handley and G. Kalonji, *Journal of Applied Physics*, 1989, **65**, 3167-3172.

36. G. A. Sawatzky, F. Van Der Woude and A. H. Morrish, *Journal of Applied Physics*, 1968, **39**, 1204-1205.

37. U. N. E. Programme, *Emission Gap Report 2024: No more hot air … please! With a massive gap between rhetoric and reality, countries draft new climate commitments*, 2024.

38. H. Council, *Hydrogen for Net-Zero: A critical cost-competitive energy vector*, 2021.

39. Y. Zhu, Q. Lin, Y. Zhong, H. A. Tahini, Z. Shao and H. Wang, *Energy & Environmental Science*, 2020, **13**, 3361-3392.

40. M. J. Molaei, *Fuel*, 2024, **365**, 131159.

41. A. Fujishima and K. Honda, *Nature*, 1972, **238**, 37-38.

42. L. Yuan, C. Han, M.-Q. Yang and Y.-J. Xu, *International Reviews in Physical Chemistry*, 2016, **35**, 1-36.

43. S. A. Razek, M. R. Popeil, L. Wangoh, J. Rana, N. Suwandaratne, J. L. Andrews, D. F. Watson, S. Banerjee and L. F. J. Piper, *Electronic Structure*, 2020, **2**, 023001.

44. K. Maeda, *Journal of Photochemistry and Photobiology C: Photochemistry Reviews*, 2011, **12**, 237-268.

45. H. Eidsvåg, S. Bentouba, P. Vajeeston, S. Yohi and D. Velauthapillai, *Molecules*, 2021, **26**, 1687.

46. T. Jafari, E. Moharreri, A. S. Amin, R. Miao, W. Song and S. L. Suib, *Molecules*, 2016, **21**, 900.

47. M. G. Walter, E. L. Warren, J. R. McKone, W. Boettcher, Q. Mi, E. A. Santori and N. S. Lewis, *Chem. Rev.*, 2010, **110**, 6446-6473.

48. R. Asahi, T. Morikawa, H. Irie and T. Ohwaki, *Chem. Rev.*, 2014, **114**, 9824-9852.

49. C. Wang, H. Qiu, T. Inoue and Q. Yao, *International Journal of Hydrogen Energy*, 2014, **39**, 12507-12514.

50. Q. Q. Ye, M. Li, X. B. Shi, M. P. Zhuo, K. L. Wang, F. Igbari, Z. K. Wang and L. S. Liao, *ACS Appl. Mater. Interfaces*, 2020, **12**, 21772-21778.

51. W. Maziarz, A. Kusior and A. Trenczek-Zajac, *Beilstein J. Nanotechnol.*, 2016, **7**, 1718-1726.

52. D. E. Scaife, *Solar Energy*, 1980, **25**, 41-54.

53. W. Erbs, J. Desilvestro, E. Borgarello and M. Grätzel, *J. Phys. Chem.*, 1984, **88**, 4001-4006.

54. K. Maeda and K. Domen, *J. Phys. Chem. C.*, 2007, **111**, 7851-7861.

55. A. B. Ellis, S. W. Kaiser, J. M. Bolts and M. S. Wrighton, *J. Am. Chem. Soc.*, 1977, **99**, 2839-2848.

56. R. Williams, *J. Chem. Phys.*, 1960, **32**, 1505-1514.

57. N. M. Gupta, *Renewable and Sustainable Energy Reviews*, 2017, **71**, 585-601.

58. N. N. Rosman, R. M. Yunus, N. R. A. M. Shah, R. M. Shah, K. Arifin, L. J. Minggu and N. A. Ludin, *International Journal of Energy Research*, 2022, **46**, 11596-11619.

59. S. Chandrasekaran, C. Bowen, P. Zhang, Z. Li, Q. Yuan, X. Ren and L. Deng, *Journal of Materials Chemistry A*, 2018, **6**, 11078-11104.

60. M. Feng, A. Yang, X. Zuo, C. Vittoria and V. G. Harris, *Journal of Applied Physics*, 2010, **107**.

61. G. Liu, J. Wang, X. Sheng, X. Xue and Y. Wang, *Ceramics International*, 2023, **49**, 29747-29754.

62. Z. Szotek, W. M. Temmerman, D. Ködderitzsch, A. Svane, L. Petit and H. Winter, *Physical Review B*, 2006, **74**, 174431.

63. S. J. Salih and W. M. Mahmood, *Heliyon*, 2023, **9**, e16601.

64. M. G. Idris, H. Y. Hafeez, J. Mohammed, A. B. Suleiman and C. E. Ndikilar, *Applied Surface Science Advances*, 2023, **18**, 100468.

65. K. Malaie, Z. Heydari and M. R. Ganjali, *International Journal of Hydrogen Energy*, 2021, **46**, 3510-3529.

66. R. Dillert, D. H. Taffa, M. Wark, T. Bredow and D. W. Bahnemann, *APL Materials*, 2015, **3**, 104001.

67. H. Ma and C. Liu, *Frontiers in Energy*, 2021, **15**, 621-630.

68. Y. Mohammed, H. Y. Hafeez, J. Mohammed, A. B. Suleiman, C. E. Ndikilar and M. G. Idris, *Next Energy*, 2024, **4**, 100145.

69. T. Helmenstine, Periodic Table with 118 Elements - Black and White, (accessed 15/07/2025, 2025).

70. S. Farzaneh, S. Hosseinzadeh, R. Samanipour, S. Hatamie, J. Ranjbari and A. Khojasteh, *Journal of Drug Delivery Science and Technology*, 2021, **64**, 102525.

71. A. S. Garanina, A. A. Nikitin, T. O. Abakumova, A. S. Semkina, A. O. Prelovskaya, V. A. Naumenko, A. S. Erofeev, P. V. Gorelkin, A. G. Majouga, M. A. Abakumov and U. Wiedwald, *Nanomaterials (Basel)*, 2021, **12**, 38.

72. R. Jasrotia, J. Prakash, Y. B. Saddeek, A. H. Alluhayb, A. M. Younis, N. Lakshmaiya, C. Prakash, K. A. Aly, M. Sillanpää, Y. A. M. Ismail, A. Kandwal and P. Sharma, *Coordination Chemistry Reviews*, 2025, **522**, 216198.

73. W. H. Wang and X. Ren, *Journal of Crystal Growth*, 2006, **289**, 605-608.

74. D. Fritsch and C. Ederer, *Physical Review B*, 2010, **82**, 104117.

75. J. D. Dunitz and L. E. Orgel, *Advances in Inorganic Chemistry and Radiochemistry*, 1960, **2**, 1-60.

76. H. L. Andersen, M. Saura-Muzquiz, C. Granados-Miralles, E. Canevet, N. Lock and M. Christensen, *Nanoscale*, 2018, **10**, 14902-14914.

77. D. Carta, M. F. Casula, A. Falqui, D. Loche, G. Mountjoy, C. Sangregorio and A. Corrias, *J. Phys. Chem. C*, 2009, **113**, 8606-8615.

78. H. Wang, P. Bencok, P. Steadman, E. Longhi, J. Zhu and Z. Wang, *J. Synchrotron Rad.*, 2012, **19**, 944-948.

79. W. L. Roth, *Journal of Physics and Chemistry of Solids*, 1964, **25**, 1-10.

80. M. E. Fleet, *Acta Cryst.*, 1981, **37**, 917-920.

81. Y. K. Wakabayashi, Y. Nonaka, Y. Takeda, S. Sakamoto, K. Ikeda, Z. Chi, G. Shibata, A. Tanaka, Y. Saitoh, H. Yamagami, M. Tanaka, A. Fujimori and R. Nakane, *Physical Review B*, 2017, **96**, 104410.

82. A. Subedi, D. Yang, Y. Yun, X. Xu and P. A. Dowben, *Journal of Vacuum Science & Technology A*, 2022, **40**, 023201.

83. N. Kita, N. Shibuichi and S. Sasaki, *J. Synchrotron Rad.*, 2001, **8**, 446-448.

84. H. Wang, Q. Hu, J. Qiu, R. Guo and X. Liu, *Catalysis Science & Technology*, 2023, **13**, 6102-6125.

85. M. Benlembarek, N. Salhi, R. Benrabaa, A. M. Djaballah, A. Boulahouache and M. Trari, *International Journal of Hydrogen Energy*, 2022, **47**, 9239-9247.

86. G. He, Y. Wen, C. Ma, X. Li, L. Gao and Z. Sun, *International Journal of Hydrogen Energy*, 2021, **46**, 5369-5377.

87. A. Farooq, S. Khalil, B. Basha, A. Habib, M. S. Al-Buriahi, M. F. Warsi, S. Yousaf and M. Shahid, *International Journal of Hydrogen Energy*, 2024, **51**, 1318-1332.

88. S. Bellamkonda, C. Chakma, S. Guru, B. Neppolian and G. R. Rao, *International Journal of Hydrogen Energy*, 2022, **47**, 18708-18724.

89. X. Jiang, D. Fan, X. Yao, Z. Dong, X. Li, S. Ma, J. Liu, D. Zhang, H. Li, X. Pu and P. Cai, *J. Colloid Interface Sci.*, 2023, **641**, 26-35.

90. W. Ge, J. Song, S. Deng, K. Liu and P. Yang, *Separation and Purification Technology*, 2024, **328**, 125059.

91. A. El Arrassi, Z. Liu, M. V. Evers, N. Blanc, G. Bendt, S. Saddeler, D. Tetzlaff, D. Pohl, C. Damm, S. Schulz and K. Tschulik, *J. Am. Chem. Soc.*, 2019, **141**, 9197-9201.

92. C. Mahala, M. D. Sharma and M. Basu, *Electrochimica Acta*, 2018, **273**, 462-473.

93. Y. Ji, J. Wu, H. Wen, S. Wang and L. Feng, *Chemical Engineering Journal*, 2024, **496**, 154211.

94. L. Royer, J. Guehl, M. Zilbermann, T. Dintzer, C. Leuvrey, B. P. Pichon, E. Savinova and A. Bonnefont, *Electrochimica Acta*, 2023, **446**, 141981.

95. Q. Yameen, M. Ikram, S. Moeen, M. Imran, A. Ul-Hamid, G. Ali, S. Goumri-Said and M. B. Kanoun, *Chemosphere*, 2025, **382**, 144490.

96. S. M. Fotukian, A. Barati, M. Soleymani and A. M. Alizadeh, *Journal of Alloys and Compounds*, 2020, **816**, 152548.

97. S. Özçelik, *BioNanoSci.*, 2023, **13**, 958-972.

98. N. Hamdan, M. A. Haija, F. Banat and A. Eskhan, *Desalination and Water Treatment*, 2017, **69**, 268-283.

99. T. P. Oliveira, S. F. Rodrigues, G. N. Marques, R. C. Viana Costa, C. G. Garçone Lopes, C. Aranas, A. Rojas, J. H. Gomes Rangel and M. M. Oliveira, *Catalysts*, 2022, **12**, 623.

100. S. Sharma, P. Jakhar and H. Sharma, *Journal of the Chinese Chemical Society*, 2023, **70**, 107-127.

101. B. Ren, Y. Huang, C. Han, M. N. Nadagouda and D. D. Dionysiou, *Ferrites as Photocatalysts for Water Splitting and Degradation of Contaminants*, American Chemical Society, Washington, 2016.

102. S. Anandan, T. Selvamani, G. G. Prasad, A. M. Asiri and J. J. Wu, *Journal of Magnetism and Magnetic Materials*, 2017, **432**, 437-443.

103. J. Z. Jiang, G. F. Goya and H. R. Rechenberg, *J. Phys. Condens. Matter*, 1999, **11**, 4063.

104. Z. Jiang, W. Zhang, W. Shangguan, X. Wu and Y. Teraoka, *The Journal of Physical Chemistry C*, 2011, **115**, 13035-13040.

105. D. Odkhuu, T. Tsevelmaa, D. Sangaa, N. Tsogbadrakh, S. H. Rhim and S. C. Hong, *Physical Review B*, 2018, **98**, 094408.

106. M. Siddique and N. M. Butt, *Physica B: Condensed Matter*, 2010, **405**, 4211-4215.

107. D. Pajić, K. Zadro, R. E. Vanderberghe and I. Nedkov, *Journal of Magnetism and Magnetic Materials*, 2004, **281**, 353-363.

108. K. Baruah, A. Kant, P. Gaijon, S. Ghosh and M. R. Singh, *Applied Surface Science Advances*, 2021, **6**, 100130.

109. N. Kareem, I. Karim, S. A. Alsalhi, J. Makasana, M. M. Rekha, G. S. Kumar, M. A. Al-Anber, S. N. Das, R. R. Chaudhary, A. Kumar and A. D. Oza, *Journal of the Indian Chemical Society*, 2025, **102**, 101759.

110. Q. Li, L. Zhang, C. Tang and J. Yin, *European Journal of Inorganic Chemistry*, 2019, **2019**, 3476-3480.

111. A. Soto-Arreola, A. M. Huerta-Flores, J. M. Mora-Hernández and L. M. Torres-Martínez, *Journal of Photochemistry and Photobiology A: Chemistry*, 2018, **357**, 20-29.

112. S. Bera, S. Ghosh, T. Maiyalagan and R. N. Basu, *ACS Applied Energy Materials*, 2022, **5**, 3821-3833.

113. H. Yang, J. Yan, Z. Lu, X. Cheng and Y. Tang, *Journal of Alloys and Compounds*, 2009, **476**, 715-719.

114. R. Cheng, X. Fan, M. Wang, M. Li, J. Tian and L. Zhang, *RSC Advances*, 2016, **6**, 18990-18995.

115. S. Hussain, S. Hussain, A. Waleed, M. M. Tavakoli, Z. Wang, S. Yang, Z. Fan and M. A. Nadeem, *ACS Appl. Mater. Interfaces*, 2016, **8**, 35315-35322.

116. S. M. Hoque, M. S. Hossain, S. Choudhury, S. Akhter and F. Hyder, *Mater. Lett.*, 2016, **162**, 60-63.

117. N. T. T. Nguyen, T. T. T. Nguyen, D. T. C. Nguyen and T. V. Tran, *Sci. Total Environ.*, 2023, **872**, 162212.

118. F. S. Li, L. Wang, J. B. Wang, Q. G. Zhou, X. Z. Zhou, H. P. Kunkel and G. Williams, *Journal of Magnetism and Magnetic Materials*, 2004, **268**, 332-339.

119. J. Philip, G. Gnanaprakash, G. Panneerselvam, M. Antony, T. Jayakumar and B. Raj, *Journal of Applied Physics*, 2007, **102**, 054305.

120. A. A. Rodríguez-Rodríguez, M. B. Moreno-Trejo, M. J. Meléndez-Zaragoza, V. Collins-Martínez, A. López-Ortís, E. Martínez-Guerra and M. Sánchez-Domínguez, *Int. J. Hydrogen Energy*, 2019, **44**, 12421-12429.

121. H. Lv, L. Ma, P. Zeng, D. Ke and T. Peng, *Journal of Materials Chemistry*, 2010, **20**, 3665.

122. R. Dom, R. Subasri, N. Y. Hebalkar, A. S. Chary and P. H. Borse, *RSC Advances*, 2012, **2**, 12782.

123. S. Boumaza, A. Boudjemaa, A. Bouguelia, R. Bouarab and M. Trari, *Applied Energy*, 2010, **87**, 2230-2236.

124. S. Das, S. Paramanik, R. G. Nair and A. Chowdhury, *Chemistry*, 2024, **30**, e202402512.

125. R. Kalia, Pushpendra, R. K. Kunchala, S. N. Achary and B. S. Naidu, *Journal of Alloys and Compounds*, 2021, **875**, 159905.

126. S. D. Jituri, R. P. NIkam, V. J. Mane, C. D. Lokhande and S. H. Mujawar, *J. Mater. Sci: Mater. Electron*, 2023, **34**, 1842.

127. Y. Lim, S. Y. Lee, D. Kim, M.-K. Han, H. S. Han, S. H. Kang, J. K. Kim, U. Sim and Y. I. Park, *Chemical Engineering Journal*, 2022, **438**, 135503.

128. A. K. Singh, S. Kumar, B. S. Yadav, A. K. Vishwakarma and N. Kumar, *Appl. Phys. Lett.*, 2023, **123**, 033902.

129. X. Xu, A. K. Azad and J. T. S. Irvine, *Catalysis Today*, 2013, **199**, 22-26.

130. L. Zou, X. Xiang, M. Wei, F. Li and D. G. Evans, *Inorg. Chem.*, 2008, **47**, 1361-1369.

131. N. Li, X. Duan, F. Yu and H. Jiang, *Vacuum*, 2017, **142**, 1-4.

132. M. Baojun, L. Keying, S. Weiguang and L. Wanyi, *Applied Surface Science*, 2014, **317**, 682-687.

133. M. Zhong, Y. Li, I. Yamada and J. J. Delaunay, *Nanoscale*, 2012, **4**, 1509-1514.

134. X. Yang, J. Ma, R. Guo, X. Fan, P. Xue, X. Wang, H. Sun, Q. Yang and X. Lai, *Materials Chemistry Frontiers*, 2021, **5**, 5790-5797.

135. C. A. Hall, P. Ferrer, D. C. Grinter, S. Kumar, I. da Silva, J. Rubio-Zuazo, P. Bencok, F. de Groot, G. Held and R. Grau-Crespo, *Journal of Materials Chemistry A*, 2024, **12**, 29645-29656.

136. F. R. Elder, A. M. Gurewitsch, R. V. Langmuir and H. C. Pollock, *Physical Review*, 1947, **71**, 829-830.

137. J. C. Maxwell, *Phil. Trans. R. Soc. Lond.*, 1865, **155**, 459-512.

138. J. Schwinger, *Physical Review*, 1949, **75**, 1912-1925.

139. H. Saisho and Y. Goshshi, *Applications of Synchrotron Radiation to Materials Analysis*, Elsevier, The Netherlands, 1996.

140. T. Sham, *Chemical Applications of Synchrotron Radiation*, World Scientific, Singapore, 2002.

141. P. Suortti and W. Thomlinson, *Phys. Med. Biol.*, 2003, **48**, 1-35.

142. S. Dubsky, *Chapter 20 - Synchrotron-Based Dynamic Lung Imaging*, Academic Press, 2021.

143. D. C. Grinter, P. Ferrer, F. Venturini, M. A. van Spronsen, A. I. Large, S. Kumar, M. Jaugstetter, A. Iordachescu, A. Watts, S. L. M. Schroeder, A. Kroner, F. Grillo, S. M. Francis, P. B. Webb, M. Hand, A. Walters, M. Hillman and G. Held, *J. Synchrotron Rad.*, 2024, **31**, 578-589.

144. G. Held, F. Venturini, D. C. Grinter, P. Ferrer, R. Arrigo, L. Deacon, W. Quevedo Garzon, K. Roy, A. Large, C. Stephens, A. Watts, P. Larkin, M. Hand, H. Wang, L. Pratt, J. J. Mudd, T. Richardson, S. Patel, M. Hillman and S. Scott, *J. Synchrotron Rad.*, 2020, **27**, 1153-1166.

145. D. C. Grinter, F. Venturini, P. Ferrer, M. A. van Spronsen, R. Arrigo, W. Quevedo Garzon, K. Roy, A. I. Large, S. Kumar and G. Held, *Synchrotron Radiation News*, 2022, **35**, 39-47.

146. H. Hertz, *Annalen der Physik*, 1887, **267**, 421-448.

147. A. Einstein, *Annalen der Physik*, 1905, **17**, 132-147.

148. A. Fahlman, C. Nordling and K. Siegbahn, *ESCA: atomic, molecular and solid state structure studied by means of electron spectroscopy*, Almqvist and Wiksell, Uppsala, 1967.

149. T. Koopman, *Physica*, 1934, **1**, 104-113.

150. S. Hüfner, *Photoelectron Spectroscopy: Prinicíples and Applications*, Springer New York 2003.

151. C. Nicolas and C. Miron, *Journal of Electron Spectroscopy and Related Phenomena*, 2012, **185**, 267-272.

152. M. C. Biesinger, B. P. Payne, A. P. Grosvenor, L. W. M. Lau, A. R. Gerson and R. S. C. Smart, *Applied Surface Science*, 2011, **257**, 2717-2730.

153. A. P. Grosvenor, B. A. Kobe, M. C. Biesinger and N. S. McIntyre, *Surface and Interface Analysis*, 2004, **36**, 1564-1574.

154. F. M. de Groot, *Coordination Chemistry Reviews*, 2005, **249**, 31-63.

155. D. R. Baer, K. Artyushkova, C. R. Brundle, J. E. Castle, M. H. Engelhard, K. J. Gaskell, J. T. Grant, R. T. Haasch, M. R. Linford, C. J. Powell, A. G. Shard, P. M. A. Sherwood and V. S. Smentkowski, *J. Vac. Sci. Technol. A*, 2019, **37**, 063203.

156. A. Proctor and P. M. A. Sherwood, *Anal. Chem.*, 1982, **54**, 13-19.

157. D. A. Shirley, *Physical Review B*, 1972, **5**, 4709-4714.

158. S. Tougaard and P. Sigmund, *Physical Review B*, 1982, **25**, 4452-4466.

159. J. E. Castle and A. M. Salvi, *Journal of Vacuum Science & Technology A: Vacuum, Surfaces, and Films*, 2001, **19**, 1170-1175.

160. J. Végh, *Journal of Electron Spectroscopy and Related Phenomena*, 1988, **46**, 411-417.

161. J. J. Yeh and I. Lindau, *Atomic Data and Nuclear Data Tables*, 1985, **32**, 1-155.

162. J. H. Scofield, *Technical Report UCRL-51326*, 1973, DOI: https://doi.org/10.2172/4545040.

163. C. Kalha, N. K. Fernando, C. V. Hernandez, E. E. Kurtulus, J. Li, Y. Zhoi and A. Regoutz, *Journal*, 2021, DOI: https://doi.org/10.6084/m9.figshare.12389750.v2.

164. C. Kalha, N. K. Fernando and A. Regoutz, *Journal*, 2020, DOI: https://doi.org/10.6084/m9.figshare.12967079.v1.

165. J. C. Vickerman and I. S. Gilmore, *Surface Analysis: The Principal Techniques*, John Wiley & Sons, Chichester, 2009.

166. A. Patton Weber, Doctor of Philosophy, University of Missouri-Kansas City, 2015.

167. M. P. Seah and W. A. Dench, *Surface and Interface Analysis*, 1979, **1**, 1-11.

168. H. Siegbahn and K. Siegbahn, *Journal of Electron Spectroscopy and Related Phenomena*, 1973, **2**, 319-325.

169. C. Arble, M. Jia and J. T. Newberg, *Surface Science Reports*, 2018, **73**, 37-57.

170. C. Schlueter, A. Gloskovskii, K. Ederer, I. Schostak, S. Piec, I. Sarkar, Y. Matveyev, P. Lömker, M. Sing, R. Claessen, C. Wiemann, C. M. Schneider, K. Medjanik, G. Schönhense, P. Amann, A. Nilsson and W. Drube, *AIP Conf. Proc.*, 2019, **2054**, 040010.

171. Y. W. Choi, H. Mistry and B. Roldan Cuenya, *Current Opinion in Electrochemistry*, 2017, **1**, 95-103.

172. E. J. Crumlin, H. Bluhm and Z. Liu, *Journal of Electron Spectroscopy and Related Phenomena*, 2013, **190**, 84-92.

173. K. A. Stoerzinger, W. T. Hong, E. J. Crumlin, H. Bluhm and Y. Shao-Horn, *Acc. Chem. Res.*, 2015, **48**, 2976-2983.

174. S. Alayoglu and G. A. Somorjai, *Topics in Catalysis*, 2015, **59**, 420-438.

175. J. Dou, Z. Sun, A. A. Opalade, N. Wang, W. Fu and F. F. Tao, *Chem. Soc. Rev.*, 2017, **46**, 2001-2027.

176. D. E. Starr, H. Bluhm, Z. Liu, A. Knop-Gericke and M. Hävecker, *Application of Ambient-Pressure X-ray Photoelectron Spectroscopy for the In-situ Investigation of Heterogeneous Catalytic Reactions*, Wiley, New York, 2013.

177. J. F. Watts and J. E. Castle, *Surface and Interface Analysis*, 2024, **56**, 408-424.

178. L. Weinhardt, R. Steininger, D. Kreikemeyer-Lorenzo, S. Mangold, D. Hauschild, D. Batchelor, T. Spangenberg and C. Heske, *J. Synchrotron Rad.*, 2021, **28**, 609-617.

179. M. Pijolat and G. Hollinger, *Surface Science*, 1981, **105**, 114-128.

180. B. J. Tyler, D. G. Castner and B. D. Ratner, *Surface and Interface Analysis*, 1989, **14**, 443-450.

181. D. E. Sayers, E. A. Stern and F. W. Lytle, *Physical Review Letters*, 1971, **27**, 1204-1207.

182. P. Eisenberger and B. M. Kincaid, *Science*, 1978, **200**, 1441-1447.

183. C. Lamberti and J. A. van Bokhoven, *X-Ray Absorption and X-Ray Emission Spectroscopy: Theory and Applications*, John Wiley & Sons, Ltd, Chichester, United Kingdom, 2016.

184. F. M. de Groot and A. Kotani, *Core Level Spectroscopy of Solids*, CRC Press, Boca Raton, Florida, 2008.

185. S. Krishnan, M. Y. Paik, C. K. Ober, E. Martinelli, G. Galli, K. E. Sohn, E. J. Kramer and D. A. Fischer, *Macromolecules*, 2010, **43**, 4733-4743.

186. B. Pollakowski, P. Hoffmann, M. Kosinova, O. Baake, V. Trunova, R. Unterumsberger, W. Ensinger and B. Beckhoff, *Anal. Chem.*, 2013, **85**, 193-200.

187. K. E. Sohn, M. D. Dimitriou, J. Genzer, D. A. Fischer, C. J. Hawker and E. J. Kramer, *Langmuir*, 2009, **25**, 6341-6348.

188. D. Asakura, E. Hosono, Y. Nanba, H. Zhou, J. Okabayashi, C. Ban, P.-A. Glans, J. Guo, T. Mizokawa, G. Chen, A. J. Achkar, D. G. Hawthron, T. Z. Regier and H. Wadati, *AIP Advances*, 2016, **6**, 035105.

189. C. C. Chiu, Y. W. Chang, Y. C. Shao, Y. C. Liu, J. M. Lee, S. W. Huang, W. Yang, J. Guo, F. M. F. de Groot, J. C. Yang and Y. D. Chuang, *Sci. Rep.*, 2021, **11**, 5250.

190. M. O. Krause, *Journal of Physical and Chemical Reference Data*, 1979, **8**, 307-327.

191. A. J. Achkar, T. Z. Regier, H. Wadati, Y. J. Kim, H. Zhang and D. G. Hawthorn, *Physical Review B*, 2011, **83**, 081106(R).

192. M. Terauchi, Y. K. Sato, T. D. Yokoyama and T. Murano, *Microscopy*, 2024, **73**, 451-455.

193. Y. Waseda, E. Matsubara and K. Shinoda, *X-Ray Diffraction Crystallography: Introduction, Examples and Solved Problems*, Springer, Berlin, 2011.

194. L. Alexander, H. P. Klug and E. Kummer, *J. Appl. Phys.*, 1948, **19**, 742-753.

195. B. Hehlen and R. Vacher, in *Atomic Structure of Glasses Investigated by Diffraction and Scattering of Radiations*, eds. K. Annapurna and A. R. Molla, Springer, Singapore, 2022, vol. 178.

196. C. T. P. Metzger, Julius-Maximilians-Universität Würzburg, 2020.

197. L. E. C. van de Leemput and H. van Kempen, *Rep. Prog. Phys.*, 1992, **55**, 1165.

198. N. Maturi, Doctor of Philosophy, Université de Franche-Comté, 2013.

199. T. Giovannini, S. Gomez and C. Cappelli, *J. Phys. Chem. Lett.*, 2025, **16**, 3106-3121.

200. J. Grunenberg, *Computational Spectroscopy: Methods, Experiments and Applications*, Wiley, Germany, 2011.

201. T. L. C. Jansen, *J. Chem. Phys.*, 2021, **155**, 170901.

202. C. R. A. Catlow, *Computer Modelling in Inorganic Crystallography*, Academic Press, London, 1997.

203. A. Srivastava, T. Nagai, A. Srivastava, O. Miyashita and F. Tama, *Int J Mol Sci*, 2018, **19**.

204. R. O. Dror, R. M. Dirks, J. P. Grossman, H. Xu and D. E. Shaw, *Annu Rev Biophys*, 2012, **41**, 429-452.

205. E. H. Lee, J. Hsin, M. Sotomayor, G. Comellas and K. Schulten, *Structure*, 2009, **17**, 1295-1306.

206. E. McLeod and A. Ozcan, *Rep Prog Phys*, 2016, **79**, 076001.

207. J. Dalton, *A new system of chemical philosophy, v. 1; pt. 1*, S. Russell for R. Bickerstaff, London, 1808.

208. M. S. Newman, *Journal of Chemical Education*, 1955, **32**, 344.

209. S. Lemonick, *C&EN Global Enterprise*, 2021, **99**, 13-15.

210. E. N. Muratov, R. Amaro, C. H. Andrade, N. Brown, S. Ekins, D. Fourches, O. Isayev, D. Kozakov, J. L. Medina-Franco, K. M. Merz, T. I. Oprea, V. Poroikov, G. Schneider, M. H. Todd, A. Varnek, D. A. Winkler, A. V. Zakharov, A. Cherkasov and A. Tropsha, *Chem. Soc. Rev.*, 2021, **50**, 9121-9151.

211. M. Born and R. Oppenheimer, *Annalen der Physik*, 1927, **389**, 457-484.

212. P. Hohenberg and W. Kohn, *Physical Review*, 1964, **136**, B864-B871.

213. W. Kohn and L. J. Sham, *Physical Review*, 1965, **140**, A1133-A1138.

214. E. G. Lewars, *Computational Chemistry: Introduction to the Theory and Applications of Molecular and Quantum Mechanics Third Edition*, Springer, Switzerland, 2016.

215. F. Jensen, *Introduction to Computational Chemistry*, John Wiley & Sons, Chichester, 2017.

216. K. Burke, J. P. Perdew and Y. Wang, in *Electronic Density Functional Theory*, eds. J. F. Dobson, G. Vignale and M. P. Das, Springer, Boston, 1998.

217. J. P. Perdew, K. Burke and M. Ernzerhof, *Phys. Rev. Lett.*, 1996, **77**, 3865.

218. Y. Zhang and W. Yang, *Phys. Rev. Lett.*, 1998, **80**, 890.

219. J. P. Perdew, A. Ruzsinszky, G. I. Csonka, O. A. Vydrov, G. E. Scuseria, L. A. Constantin, X. Zhou and K. Burke, *Phys Rev Lett*, 2008, **100**, 136406.

220. J. L. Bao, L. Gagliardi and D. G. Truhlar, *J Phys Chem Lett*, 2018, **9**, 2353-2358.

221. V. I. Anisimov, F. Aryasetiawan and A. I. Lichtenstein, *J. Phys.: Condens. Matter*, 1997, **9**, 767.

222. V. V. Anisimov, J. Zaanen and O. K. Andersen, *Phys Rev B Condens Matter*, 1991, **44**, 943-954.

223. A. D. Becke, *The Journal of Chemical Physics*, 1993, **98**, 1372-1377.

224. P. J. Stephens, F. J. Devlin, C. F. Chabalowski and M. J. Frisch, *J. Phys. Chem.*, 1994, **98**, 11623-11627.

225. C. Adamo and V. Barone, *The Journal of Chemical Physics*, 1999, **110**, 6158-6170.

226. J. Heyd, G. E. Scuseria and M. Ernzerhof, *J. Chem. Phys.*, 2003, **118**, 8207-8215.

227. D. S. Sholl and J. A. Steckel, *Density Functional Theory: A Practical Introduction*, John Wiley & Sons, New Jersey, 2009.

228. P. E. Blöchl, *Phys. Rev. B Condens. Matter.*, 1994, **50**, 17953-17979.

229. G. Kresse and D. Joubert, *Phys. Rev. B*, 1999, **59**, 1758-1755.

230. M. Gajdoš, K. Hummer, G. Kresse, J. Furthmüller and F. Bechstedt, *Physical Review B*, 2006, **73**.

231. S. Grimme, J. Antony, S. Ehrlich and H. Krieg, *J. Chem. Phys.*, 2010, **132**, 154104.

232. H. J. Monkhorst and J. D. Pack, *Physical Review B*, 1976, **13**, 5188-5192.

233. A. Maniopoulou, E. R. M. Davidson, R. Grau-Crespo, A. Walsh, I. J. Bush, C. R. A. Catlow and S. M. Woodley, *Computer Physics Communications*, 2012, **183**, 1696-1701.

234. P. W. Tasker, *J. Phys. Chem. C: Solid State Phys*, 1979, **12**, 4977.

235. V. Consonni and A. M. Lord, *Nano Energy*, 2021, **83**.

236. H. Ikeno, F. M. de Groot, E. Stavitski and I. Tanaka, *J. Phys. Condens. Matter.*, 2009, **21**, 104208.

237. E. Stavitski and F. M. F. de Groot, *Micron*, 2010, **41**, 687-694.

238. M. Retegan, 2019.

239. M. W. Haverkort, M. Zwierzycki and O. K. Andersen, *Physical Review B*, 2012, **85**, 165113.

240. *NIST Computational Chemistry Comparison and Benchmark Database, NIST Standard Reference Database*, 2022, **101**.

241. G. Kresse and J. Furthmüller, *Physical Review B*, 1996, **54**, 11169.

242. G. Kresse and J. Furthmüller, *Computational Materials Science* 1996, **6**, 15-50.

243. J. P. B. Perdew, Kieron; Ernzerhof, Matthias, *Physical Review Letters*, 1996, **77**.

244. L. Wang, T. Maxisch and G. Ceder, *Physical Review B*, 2006, **73**, 195107.

245. R. Grau-Crespo, F. Corà, A. A. Sokol, N. H. de Leeuw and C. R. A. Catlow, *Physical Review B*, 2006, **73**, 035116.

246. Y.-L. Lee, M. J. Gadre, Y. Shao-Horn and D. Morgan, *Physical Chemistry Chemical Physics*, 2015, **17**, 21643-21663.

247. C. Collins, M. S. Dyer, A. Demont, P. A. Chater, M. F. Thomas, G. R. Darling, J. B. Claridge and M. J. Rosseinsky, *Chemical Science*, 2014, **5**, 1493-1505.

248. S. Grover, K. T. Butler, U. V. Waghmare and R. Grau-Crespo, *Advanced Theory and Simulations*, 2023, **6**, 2200673.

249. P. E. Blöchl, *Physical Review B*, 1994, **50**, 17953-17979.

250. A. Hossain, M. S. I. Sarker, M. K. R. Khan and M. M. Rahman, *Materials Science and Engineering: B*, 2020, **253**, 114496.

251. Q. Cai, J.-g. Wang, Y. Wang and D. Mei, *The Journal of Physical Chemistry C*, 2016, **120**, 19087-19096.

252. D. Santos-Carballal, A. Roldan, R. Grau-Crespo and N. H. de Leeuw, *Phys. Chem. Chem. Phys.*, 2014, **16**, 21082-21097.

253. H. Guo, A. C. Marschilok, K. J. Takeuchi, E. S. Takeuchi and P. Liu, *ACS Appl. Mater. Interfaces*, 2018, **10**, 35623-35630.

254. K. L. S. Rodríguez, J. J. M. Quintero, H. H. Medina Chanduví, A. V. G. Rebaza, R. Faccio, W. A. Adeagbo, W. Hergert, C. E. R. Torres and L. A. Errico, *Applied Surface Science*, 2020, **499**, 143859.

255. R. E. Warburton, H. Iddir, L. A. Curtiss and J. Greeley, *ACS applied materials & interfaces*, 2016, **8**, 11108-11121.

256. M. W. Haverkort, G. Sangiovanni, P. Hansmann, A. Toschi, Y. Lu and S. Macke, *EPL (Europhysics Letters)*, 2014, **108**, 57004.

257. Y. Lu, M. Höppner, O. Gunnarsson and M. W. Haverkort, *Physical Review B*, 2014, **90**, 085102.

258. A. A. Coelho, *Journal of Applied Crystallography*, 2018, **51**, 210-218.

259. G. Van Der Laan, J. Zaanem and G. A. Sawatzky, *Physical Review B*, 1986, **33**, 4253-4263.

260. D. Santos-Carballal, A. Roldan, R. Grau-Crespo and N. H. de Leeuw, *Physical Review B*, 2015, **91**, 195106.

261. Y. Seminovski, P. Palacios, P. Wahnón and R. Grau-Crespo, *Applied Physics Letters*, 2012, **100**, 102112.

262. S.-H. Wei and S. Zhang, *Physical Review B*, 2001, **63**, 045112.

263. F. Tielens, M. Calatayud, R. Franco, J. M. Recio, Pérez-Ramírez. and C. Minot, *J. Phys. Chem. B*, 2006, **110**, 988-995.

264. J. Lin, J. Wu, E. Fan, X. Zhang, R. Chen, F. Wu and L. Li, *International Journal of Minerals, Metallurgy and Materials*, 2022, **29**, 942-952.

265. S. Sukmara, A. Manaf and W. Adib, *Journal of Physics: Conference Series*, 2021, **1715**, 012065.

266. V. Uvarov, *Journal of Applied Crystallography*, 2019, **52**, 252-261.

267. N. Guijarro, P. Bornoz, M. Prévot, X. Yu, X. Zhu, M. Johnson, X. Jeanbourquin, F. Le Formal and K. Sivula, *Sustainable Energy & Fuels*, 2018, **2**, 103-117.

268. M. Sundararajan, L. John Kennedy, P. Nithya, J. Judith Vijaya and M. Bououdina, *Journal of Physics and Chemistry of Solids*, 2017, **108**, 61-75.

269. Q. Liang, G. Brocks and A. Bieberle-Hütter, *Journal of Physics: Energy*, 2021, **3**, 026001.

270. H. Elnaggar, R. Wang, M. Ghiasi, M. Yañez, M. U. Delgado-Jaime, M. H. Hamed, A. Juhin, S. S. Dhesi and F. M. F. de Groot, *Physical Review Materials*, 2020, **4**, 024415.

271. B. Liu, C. Piamonteze, M. U. Delgado-Jaime, R.-P. Wang, J. Heidler, J. Dreiser, R. Chopdekar, F. Nolting and F. M. F. de Groot, *Physical Review B*, 2017, **96**, 054446.

272. R. A. D. Pattrick, G. Van Der Laan, C. M. B. Henderson, P. Kuiper, E. Dudzik and D. J. Vaughan, *European Journal of Mineralogy*, 2002, **14**, 1095-1102.

273. V. Blanco-Gutierrez, E. Climent-Pascual, M. J. Torralvo-Fernandez, R. Saez-Puche and M. T. Fernandez-Diaz, *Journal of Solid State Chemistry*, 2011, **184**, 1608-1613.

274. M. Á. Cobos, P. de la Presa, I. Puente-Orench, I. Llorente, I. Morales, A. García-Escorial, A. Hernando and J. A. Jiménez, *Ceramics International*, 2022, **48**, 12048-12055.

275. D. F. Anthrop and A. W. Searcy, *The Journal of Physical Chemistry*, 1964, **66**, 2335-2342.

276. G. W. C. Kaye and D. Ewen, *Proc. R. Soc. Lond. A*, 1913, **89**, 58-67.

277. W. Zhang, Y. Tian, D.-C. Liu, F. Wang, B. Yang and B.-Q. Xu, *Journal of Materials Research and Technology*, 2020, **9**, 3590-3597.

278. D. Zhao, X. Tian, D. E. Doronkin, S. Han, V. A. Kondratenko, J. D. Grunwaldt, A. Perechodjuk, T. H. Vuong, J. Rabeah, R. Eckelt, U. Rodemerck, D. Linke, G. Jiang, H. Jiao and E. V. Kondratenko, *Nature*, 2021, **599**, 234-238.

279. L. Zhan, Z. Qiu and Z. Xu, *Separation and Purification Technology*, 2009, **68**, 397-402.

280. L. Zhan and Z. Xu, *Environ. Sci. Technol.*, 2008, **42**, 7676-7681.

281. E. A. Redekop, T. Cordero-Lanzac, D. Salusso, A. Pokle, S. Oien-Odegaard, M. F. Sunding, S. Diplas, C. Negri, E. Borfecchia, S. Bordiga and U. Olsbye, *Chem. Mater.*, 2023, **35**, 10434-10445.

282. J. R. Sandemann, T. B. E. Gronbech, K. A. H. Stockler, F. Ye, B. C. Chakoumakos and B. B. Iversen, *Adv. Mater.*, 2023, **35**, e2207152.

283. M. A. Bhide, C. J. Carmalt and C. E. Knapp, *Journal of Materials Chemistry C*, 2020, **8**, 5501-5508.

284. A. V. Naumkin, A. Kraut-Vass, W. Gaarenstroom and C. J. Powell, *NIST X-ray Photoelectron Spectroscopy Database*, 2023, **5.0**.

285. T. Wang, B. Jin, Z. Jiao, G. Lu, J. Ye and Y. Bi, *J. Mater. Chem. A*, 2014, **2**, 15553-15559.

286. D. Xu, D. Fan and W. Shen, *Nanoscale Red. Lett.*, 2013, **8**, 46.

287. S. Gota, M. Gautier-Soyer and M. Sacchi, *Phys. Rev. B*, 2000, **62**, 4187.

288. A. Ruosi, C. Raisch, A. Verna, R. Werner, B. A. Davidson, J. Fujii, R. Kleiner and D. Koelle, *Physical Review B*, 2014, **90**.

289. M. Bowker, S. Poulston, R. A. Bennett, P. Stone, A. H. Jones, S. Haq and P. Hollins, *Journal of Molecular Catalysis A: Chemical*, 1998, **131**, 185-197.

290. G. F. Kresse, J. , *Physical Review B*, 1996, **54**, 11169.

291. G. F. Kresse, J., *Comupational Materials Science 6*, 1996, 15-50.

292. A. J. Jackson, A. M Ganose, A. Regoutz, R. G. Egdell and D. O Scanlon, *Journal of Open Source Software*, 2018, **3**.

293. C. J. Powell and A. Jablonski, *NIST Electron Inelastic-Mean-Free-Path Database. Version 1.2. SRD 71*, Nationl Institute of Standards and Technology, Gaithersburg, MD 2010.

294. C. S. Kuivila, J. B. Butt and P. C. Stair, *Applied Surface Science*, 1988, **32**, 99-121.

295. S. Alraddadi, *Applied Physics A*, 2021, **127**.

296. T. Fujii, F. M. de Groot and G. A. Sawatzky, *Phys. Rev. B* 1999, **59**, 3195.

297. J. Rubio-Zuazo, A. Chainani, M. Taguchi, D. Malterre, A. Serrano and G. R. Castro, *Physical Review B*, 2018, **97**.

298. T. Schedel-Niedrig, W. Weiss and R. Schlogl, *Phys. Rev. B Condens. Matter.*, 1995, **52**, 17449-17460.

299. T. Yamashita and P. Hayes, *Applied Surface Science*, 2008, **254**, 2441-2449.

300. S. Hoffman, *Practical Surface Analysis*, Wiley, Chichester, 1990.

301. N. Berdunov, S. Murphy, G. Mariotto and I. V. Shvets, *Physical Review B*, 2004, **70**.

302. N. Berdunov, G. Mariotto, S. Murphy, K. Balakrishnan and I. V. Shvets, *Physical Review B*, 2005, **71**.

303. B. L. Henke, E. M. Gullikson and J. C. Davis, *Atomic Data and Nuclear Data Tables*, 1993, **54**, 181-342.

304. R. Nakajima, J. Stöhr and Y. U. Idzerda, *Phys. Rev. B*, 1999, **59**, 6421.

305. S. Kaya, H. Ogasawara and A. Nilsson, *Catalysis Today*, 2015, **240**, 184-189.

306. I. A. Sarsari, C. D. Pemmaraju, H. Salamati and S. Sanvito, *Physical Review B*, 2013, **87**.

307. T. Radu, C. Iacovita, D. Benea and R. Turcu, *Applied Surface Science*, 2017, **405**, 337-343.

308. C. R. Brundle, T. J. Chuang and K. Wandelt, *Surface Science*, 1977, **68**, 459-468.

309. K. Reuter and M. Scheffler, *Physical Review B*, 2001, **65**, 035406.

310. R. Grau-Crespo, C. R. A. Catlow and N. H. de Leeuw, *Journal of Catalysis*, 2007, **248**, 77-88.

311. T. A. Mellan and R. Grau-Crespo, *The Journal of chemical physics*, 2012, **137**.

312. *NIST-JANAF Thermochemical Tables, NIST Standard Reference Database*, 1998, **13**.

313. S. W. Benson, *J. Chem. Educ.*, 1965, **42**, 502.

314. J. A. Kerr, *Chem. Rev.*, 1966, **66**, 465.

315. D.-Y. Cho, J. H. Kim, K. D. Na, J. Song, C. S. Hwang, B.-G. Park, J.-Y. Kim, C.-H. Min and S.-J. Oh, *Applied Physics Letters*, 2009, **95**.

316. M. Kazemian, F. Rossi, A. Casaroli, T. Caielli, B. Kaulich, M. Kiskinova, I. Sgura and B. Bozzini, *Journal of Power Sources*, 2022, **524**.

317. T. Mizoguchi, M. Yoshiya, J. Li, F. Oba, I. Tanaka and H. Adachi, *Ultramicroscopy*, 2001, **86**, 363-370.

318. I. Caretti, M. Yuste, R. Torres, O. Sánchez, I. Jiménez and R. Escobar Galindo, *RSC Advances*, 2012, **2**.

319. L. H. Ahrens, *Geochimica et Cosmochimica Acta*, 1952, **2**, 155-169.

320. J. Majzlan, K. Grevel and A. Navrotsky, *American Mineralogist*, 2003, **88**, 855-859.

321. R. A. Robie and B. S. Hemingway, *Thermodynamic properties of minerals and related substances at 298.15 K and 1 bar (10^5 pascals) pressure and at higher temperatures*, U.S. Geologival Survey, 1995.

322. H. Y. Kang, H. Kang, E. Lee, G. R. Lee and R. B. K. Chung, *ACS Omega*, 2021, **6**, 31292-31298.

323. M. Capdevila-Cortada, Z. Łodziana and N. López, *ACS Catalysis*, 2016, **6**, 8370-8379.

324. J. N. Harvey, *Annual Reports Section "C" (Physical Chemistry)*, 2006, **102**.

325. A. Römer, L. Hasecke, P. Blöchl and R. A. Mata, *Molecules*, 2020, **25**.

326. O. Knacke, O. Kubaschewski and K. Hesselmann, *Thermochemical Properties of Inorganic Substances, 2nd ed.*, Springer, Berlin, 1991.

327. J. Leitner, M. Kamrádek and D. Sedmidubský, *Thermochimica Acta*, 2013, **572**, 1-5.

328. A. Krishnan, K. Archana, A. S. Arsha, A. Viswam and M. S. Meera, *Chinese Journal of Catalysis*, 2025, **68**, 103-154.

329. K. Villa, J. R. Galán-Mascarós, N. López and E. Palomares, *Sustainable Energy & Fuels*, 2021, **5**, 4560-4569.

330. *MedeA and Materials Design are registered trademarks of Materials Design, Inc.*

331. D. Lerch, O. Weickhorst, G. L. W. Hart, R. W. Forcade and S. Müller, *Modeling and Simulation in Materials Science and Engineering*, 2009, **17**, 055003.

332. S. Müller, *J. Phys. Condens. Matter*, 2003, **15**, R1429-R1500.

333. P. Sánchez-Palencia, S. Hamad, P. Palacios, R. Grau-Crespo and K. T. Butler, *Digital Discovery*, 2022, **1**, 665-678.

334. T. Prabhakaran, R. V. Mangalaraja, J. C. Denardin and J. A. Jiménez, *Journal of Alloys and Compounds*, 2017, **716**, 171-183.

335. J. P. Singh, J. Y. Park, V. Singh, S. H. Kim, W. C. Lim, H. Kumar, Y. H. Kim, S. Lee and K. H. Chae, *RSC Adv.*, 2020, **10**, 21259-21269.

336. H. L. Andersen, C. Granados-Miralles, K. M. O. Jensen, M. Saura-Muzquiz and M. Christensen, *ACS Nano*, 2024, **18**, 9852-9870.

337. A. C. Dodd, A. J. McKinley, M. Saunders and T. Tsuzuki, *Journal of Nanoparticle Research*, 2006, **8**, 43-51.

338. Z. Zhang, C. Wang, R. Zakaria and J. Y. Ying, *J. Phys. Chem. B*, 1998, **102**, 10871-10878.

339. A. J. Deotale and R. V. Nandedkar, *Materials Today: Proceedings*, 2016, **3**, 2069-2076.

340. A. M. Smith and S. Nie, *Accounts of Chemical Research*, 2009, **43**, 190-200.

341. R. Viswanatha, S. Sapra, B. Satpati, P. V. Satyam, B. N. Dev and D. D. Sarma, *Journal of Materials Chemistry*, 2004, **14**, 661-668.

342. J. P. Singh, R. C. Srivastava, H. M. Agrawal, P. K. Giri, D. K. Goswami, A. Perumal and A. Chattopadhyay, *AIP Conf. Proc.*, 2010, **1276**, 137-143.